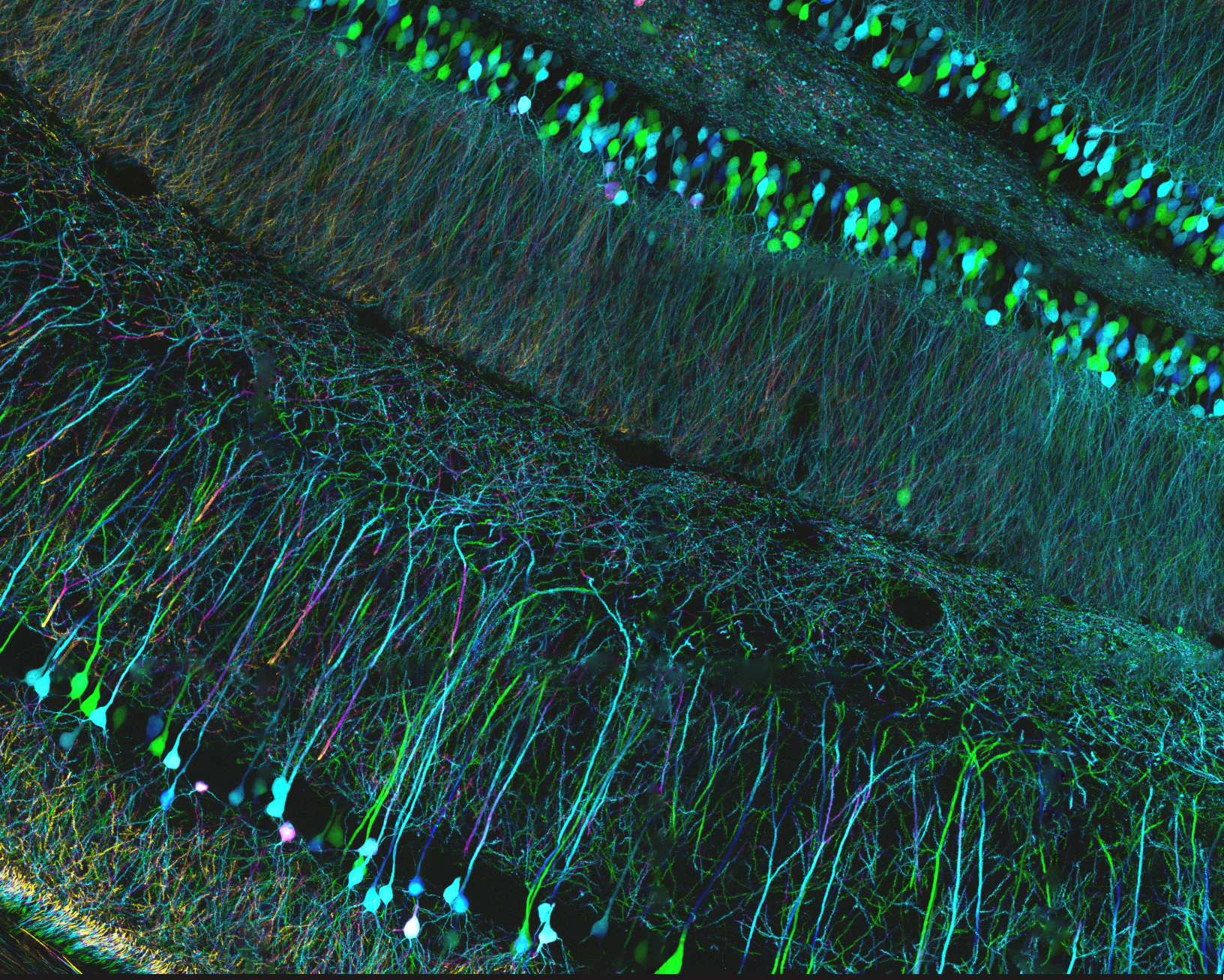

Visualizing the Dynamics of Cancer Cells: The Power of Translational Imaging

ARTICLE COLLECTION

WILEY Analytical Science

Sponsored by:

ZEISS

Seeing beyond

End-to-End Workflow Solutions to Automate Research from Image to Results

ZEISS Microscopy is here to help enable discovery and accelerate your research via the interconnected ZEISS Digital Ecosystem by making it easier to extract meaningful data in an automated, scalable fashion. Get reliable, reproduceable results via custom automated workflows that can be run continuously without user input – let the technology work for you and your lab.

Discover how we automate your entire workflow from image to results so you can focus on what's most important: the science and what the data is telling you to make informed decisions on the direction of your research.

Don't just decrease time to image…
Decrease your time to decision.

Get better data, faster.

Scan the QR code to learn more.

ZEISS

Seeing beyond

Contents

Introduction

Translational imaging is a powerful tool used in cancer research to study the dynamics of cancer cells and the changes they undergo over time. It utilizes advanced imaging techniques, such as confocal microscopy, laser scanning microscopy, and fluorescence microscopy, to visualize the cellular and molecular processes involved in cancer progression. These imaging techniques provide researchers with detailed information about the structure and function of cancer cells, as well as their interactions with the surrounding environment.

The ability to monitor and study cancer cell behavior in real-time has revolutionized cancer research. Using imaging microscopy, researchers can observe the physical changes in cancer cells, including their size, shape, and intracellular organization. In addition, imaging microscopy can be used to detect molecular changes, such as gene expression and protein expression. This allows researchers to gain a better understanding of the molecular mechanisms that drive cancer progression and metastasis.

ZEISS has an entire product portfolio to meet the needs of even the most demanding microscopy workflows used in translational cancer science, regardless of the stage of research or required throughput. From widefield and live-cell to confocal and super-resolution, the power of ZEISS' industry-leading optics provides the most detailed imaging on all sample types, ranging from large tissue sections and organoids, all the way down to sub-cellular and single-molecule resolution. ZEISS provides flexible imaging solutions to nearly any research discipline and is the reason why ZEISS is used by so many scientists in cutting-edge medical research breakthroughs.

In this article collection, we present examples of multiple ZEISS microscopes and imaging systems being applied to translational biology and cancer research to help uncover disease MOA, identify unique protein targets, and develop novel therapies. In each article, ZEISS imaging played an important role in the scientific insights gained.

This article collection begins with a study by Taffoni et al. (2022) that shows that the DNA-PK DNA repair complex can drive cGAS-independent inflammatory responses, and its catalytic activity is necessary for cGAS-dependent cGAMP production and optimal downstream signaling. It also suggests that the cooperation between DNA-PK and cGAS can promote macrophage recruitment in the tumor microenvironment, which can impair early tumorigenesis but lead to poor outcomes in glioblastoma patients.

Kim et al. (2023) report research about Plakophilin 1 (PKP1), a member of the arm-repeat family of catenins that helps stabilize cell-cell adhesion as a structural component of desmosomes. It has also been found to be involved in the post-transcriptional regulation of gene expression. PKP1 is normally expressed in the prostate epithelium but is often downregulated in more aggressive prostate cancers. When PKP1 is absent, the occurrence of T-cells, B-cells, macrophages, and neutrophils is significantly increased.

Next, Taubenschmid-Stowers et al. (2023) discuss Artemisinin, a natural compound used as an antimalarial drug and for anticancer therapy. Using yeast and stem cell screening, researchers have discovered that the cytotoxicity of Artemisinins is related to the cellular pathway of porphyrin (heme) biosynthesis. Modulating this pathway can increase the cytotoxicity of Artemisinins. Additionally, a combination of Artemisinins and 5-ALA is effective in killing brain tumor cells in multiple model systems and in vivo. This research has uncovered a critical molecular pathway for Artemisinin cytotoxicity and a sensitization strategy to treat different brain tumors.

Finally, Choi. et al. (2023) discuss ovarian cancer, which has a high degree of genetic heterogeneity, making it difficult to treat with existing therapies. This study found that endonuclease G, which is overexpressed in ovarian cancer, does not cause cell death, but instead plays a role in cell proliferation. This suggests that targeting endonuclease G may have the potential to become a treatment for ovarian cancer.

Overall, translational imaging microscopy has been instrumental in all of these studies, for advancing our understanding of cancer biology and improving our ability to diagnose and treat cancer. Through the methods and applications presented in this article collection, we hope to educate researchers on new technologies and techniques for translational imaging. For more information, we encourage you to visit ZEISS to learn more and explore options to enhance your research.

Róisín Murtagh
Editor at Wiley Analytical Science

References

Taffoni, C., Marines, J., Chamma, H., Guha, S., Saccas, M., Bouzid, A., Valadao, A.L.C., Maghe, C., Jardine, J., Park, M.K. and Polak, K., 2022. DNA damage repair kinase DNA- PK and cGAS synergize to induce cancer-related inflammation in glioblastoma. *The EMBO Journal*, p.e111961. https://www.embopress.org/doi/full/10.15252/embj.2022111961

Kim, M., Reidenbach, S., Schlechter, T., Rothmann, A.C., Will, R. and Hofmann, I. (2023), Plakophilin 1 deficiency in prostatic tumours is correlated with immune cell recruitment and controls the up-regulation of cytokine expression post-transcriptionally. *FEBS J*. https://doi.org/10.1111/febs.16680

Taubenschmid- Stowers, J., Orthofer, M., Laemmerer, A., Krauditsch, C., Rózsová, M., Studer, C., Lötsch, D., Gojo, J., Gabler, L., Dyczynski, M. and Efferth, T., 2023. A whole- genome scan for Artemisinin cytotoxicity reveals a novel therapy for human brain tumors. *EMBO molecular medicine*, 15(3), p.e16959. https://www.embopress.org/doi/full/10.15252/emmm.202216959

Choi, Y.N., Seo, T.W., Lee, Y.T., Jeong, D.H. and Yoo, S.J. (2023), Nuclear endonuclease G controls cell proliferation in ovarian cancer. *FEBS Open Bio*. https://doi.org/10.1002/2211-5463.13572

Article

SOURCE DATA | TRANSPARENT PROCESS | OPEN ACCESS

THE EMBO JOURNAL

DNA damage repair kinase DNA-PK and cGAS synergize to induce cancer-related inflammation in glioblastoma

Clara Taffoni[1,†], Johanna Marines[1,2,†], Hanane Chamma[1], Soumyabrata Guha[1], Mathilde Saccas[1], Amel Bouzid[1], Ana-Luiza Chaves Valadao[1], Clément Maghe[3,4], Jane Jardine[3,4], Mi Kyung Park[5], Katarzyna Polak[1], Mara De Martino[6], Claire Vanpouille-Box[6], Maguy Del Rio[7], Celine Gongora[7], Julie Gavard[3,4,8], Nicolas Bidère[3,4], Min Sup Song[5], Donovan Pineau[9], Jean-Philippe Hugnot[9], Karima Kissa[10], Laura Fontenille[2], Fabien P Blanchet[11], Isabelle K Vila[1] & Nadine Laguette[1,*]

Abstract

Cytosolic DNA promotes inflammatory responses upon detection by the cyclic GMP-AMP (cGAMP) synthase (cGAS). It has been suggested that cGAS downregulation is an immune escape strategy harnessed by tumor cells. Here, we used glioblastoma cells that show undetectable cGAS levels to address if alternative DNA detection pathways can promote pro-inflammatory signaling. We show that the DNA-PK DNA repair complex (i) drives cGAS-independent IRF3-mediated type I Interferon responses and (ii) that its catalytic activity is required for cGAS-dependent cGAMP production and optimal downstream signaling. We further show that the cooperation between DNA-PK and cGAS favors the expression of chemokines that promote macrophage recruitment in the tumor microenvironment in a glioblastoma model, a process that impairs early tumorigenesis but correlates with poor outcome in glioblastoma patients. Thus, our study supports that cGAS-dependent signaling is acquired during tumorigenesis and that cGAS and DNA-PK activities should be analyzed concertedly to predict the impact of strategies aiming to boost tumor immunogenicity.

Keywords cGAS; DNA-PK; inflammation; tumor immunogenicity
Subject Categories Cancer; Immunology; Signal Transduction
DOI 10.15252/embj.2022111961 | Received 23 June 2022 | Revised 30 November 2022 | Accepted 2 December 2022 | Published online 27 December 2022
The EMBO Journal (2023) 42: e111961

Introduction

Most cells mount type I Interferon (IFN) responses in the presence of cytosolic DNA (Hartmann, 2017). One of the key pathways involved in the detection of immune-stimulatory DNA relies on the cyclic GMP-AMP synthase (cGAS). Upon detection of dsDNA, ssDNA, or RNA:DNA hybrids (Guerra *et al*, 2020, Sun *et al*, 2013), cGAS produces the cyclic GMP-AMP (cGAMP) second messenger. Interaction of cGAMP with the Stimulator of Interferon Genes (STING) promotes the assembly of a signalosome comprised of the Tank Binding Kinase 1 (TBK1) and transcription factors such as Interferon Regulatory Factor 3 (IRF3) (Tanaka & Chen, 2012). TBK1-dependent phosphorylation of IRF3 leads to its nuclear translocation and subsequent activation of transcriptional programs that ultimately lead to the production of inflammatory cytokines, chemokines, and type I IFNs (Ishikawa *et al*, 2009).

The cGAS-STING signaling cascade has been shown to be essential to the orchestration of antitumor responses (Corrales *et al*, 2016, Zhu *et al*, 2019). Indeed, activating the cGAS-STING axis can promote tumor rejection through increasing tumor immunogenicity and priming T cell responses (Sen *et al*, 2019, Sivick *et al*, 2018). However, STING activation can also foster metastatic dissemination (Chen *et al*, 2016) and impair the establishment of durable immunity (Larkin *et al*, 2017). In addition, the cGAS-STING axis has been shown to support the survival of chromosomally unstable cancers (Hong *et al*, 2022), providing an explanation for cGAS-STING

1 IGH, Université de Montpellier, CNRS, Montpellier, France
2 Azelead©, Montpellier, France
3 Team SOAP, CRCI2NA, Nantes Université, Inserm, CNRS, Université d'Angers, Nantes, France
4 Equipe Labellisée Ligue Contre le Cancer, Paris, France
5 Department of Molecular and Cellular Oncology, The University of Texas MD Anderson Cancer Center, Houston, TX, USA
6 Department of Radiation Oncology, Weill Cornell Medicine, New York, NY, USA
7 Institut de Recherche en Cancérologie de Montpellier (IRCM), INSERM, Université de Montpellier, ICM, Montpellier, France
8 Institut de Cancérologie de l'Ouest (ICO), Saint-Herblain, France
9 Institut de Génomique Fonctionnelle (IGF), Université de Montpellier, CNRS, INSERM, Montpellier, France
10 Université de Montpellier, CNRS UMR 5235, Montpellier, France
11 Institut de Recherche en Infectiologie de Montpellier, Université de Montpellier, CNRS, Montpellier, France
*Corresponding author. Tel: +33 434359811; E-mail: nadine.laguette@igh.cnrs.fr
†These authors contributed equally to this work

inactivation in primary tumors (Bakhoum & Cantley, 2018, Bakhoum *et al*, 2018) and activation in late tumorigenesis (Mayca Pozo *et al*, 2021). In addition to these tumor-intrinsic parameters, the diversity of cells composing the tumor microenvironment and their differential expression of cGAS and/or STING are also determinant for tumor fate (Chamma *et al*, 2022a). Prior studies have suggested that downregulation of the cGAS-STING axis is an immune escape strategy exploited by tumor cells (Song *et al*, 2017, Xia *et al*, 2016), despite evidence that high expression of cGAS and/or STING predicts poor outcome for cancer patients (An *et al*, 2019). Reconciling both views likely requires the integration of both tumor-intrinsic and -extrinsic immunogenicity drivers.

Recently, the DNA-dependent protein kinase (DNA-PK) complex, involved in the repair of double-strand DNA lesions by non-homologous end-joining (NHEJ) (Yue *et al*, 2020), has been involved in the detection of DNA virus-derived cytosolic dsDNA, eliciting type I or III IFN responses (Burleigh *et al*, 2020, Ferguson *et al*, 2012, Morchikh *et al*, 2017, Sui *et al*, 2017, Zhang *et al*, 2011). The DNA-PK core complex is a holoenzyme composed of the KU70^{XRCC6} and KU80^{XRCC5} subunits that ensure the recruitment of the DNA-dependent protein kinase catalytic subunit (DNA-PKcs^{PRKDC}) to double-strand breaks (Hammel *et al*, 2010). How cGAS- and DNA-PK-mediated detection of dsDNA are coordinated remains the subject of controversies. Indeed, there are reports indicating that DNA-PKcs inhibits cGAS (Sun *et al*, 2020, Wang *et al*, 2022), while others suggest that DNA-PK may be required for cGAS-STING-dependent inflammatory responses to viral DNA (Morchikh *et al*, 2017, Tao *et al*, 2022). Intriguingly, despite the crucial role of DNA-PK in NHEJ, and the tight link between DNA repair machineries and nucleic acid sensing (Taffoni *et al*, 2021), there is no evidence for a role of DNA-PK in eliciting inflammatory responses following genotoxic stress (Burleigh *et al*, 2020).

Here, we used glioblastoma cells to interrogate how type I IFN responses are initiated in the absence of detectable cGAS. We found that DNA-PK can promote nucleic acid- and chemotherapy-associated inflammatory responses independently of cGAS. Further, we uncover that cGAS and DNA-PK cooperate for optimal STING-dependent signaling, thereby defining tumor immunogenicity. Our work thus suggests that cGAS-dependent signaling is acquired during tumorigenesis.

Results

DNA-PK catalytic activity promotes cytosolic dsDNA-dependent type I Interferon responses in cGAS-deficient cells

Assessment of dsDNA-induced type I IFN responses in the T98G glioblastoma cell line, which does not express detectable cGAS levels (Figs 1A and EV1A), showed increased Interferon β (*IFNB*) and C-X-C motif chemokine ligand 10 (*CXCL10*) Interferon-stimulated gene (ISG) mRNA levels (Fig 1B), attesting to the activation of type I IFN responses. Western blot (WB) analysis further showed that dsDNA stimulation of T98G led to phosphorylation of IRF3 (pIRF3) (Fig 1A). Similar analysis, conducted on CD133^{+} glioblastoma stem cells (namely, Gli4 and Gli7) (Guichet *et al*, 2013) and patient-derived glioblastoma stem-like cells (GSC4, 6, 9, 13, 15) (Harford-Wright *et al*, 2017), confirmed the absence of cGAS (Figs 1C and EV1B–D) and showed that upon challenge with dsDNA these cells present increased pIRF3 (Figs 1C and EV1B and D), *IFNB* and *CXCL10* (Figs 1D and EV1E and F). In addition, conditioned media from T98G cells treated with dsDNA were sufficient to induce the expression of the Interferon-induced protein with tetratricopeptide repeats (*IFIT*) *1*, *IFIT2*, myxovirus resistance protein 1 (*MXA*) and 2′-5′-Oligoadenylate Synthetase 1 (*OAS1*) ISGs in the THP-1 myeloid cell line (Fig 1E). This attests to the production of bioactive type I IFNs from glioblastoma cells, where cGAS is not detectable, further indicating that glioblastoma cells possess cGAS-independent cytosolic dsDNA detection mechanisms.

Because the DNA-PK complex was previously reported as an alternative cytosolic dsDNA sensor, we interrogated whether DNA-PK could be responsible for the type I IFN response elicited by dsDNA in absence of cGAS. To this aim, we first performed WB analysis using an antibody specific for the auto-phosphorylation of DNA-PKcs on Serine 2056 (pDNA-PKcs), which reflects its activation (Chen *et al*, 2005). Stimulation of T98G, Gli4, Gli7, and GSC9

Figure 1. DNA-PK catalytic activity promotes nucleic acid-dependent type I IFN responses in cGAS-deficient cells.

A T98G cells were challenged or not with dsDNA or with 2′3′cGAMP for 6 h prior to whole cell extraction and Western Blot (WB) analysis using indicated antibodies.
B *IFNB* and *CXCL10* mRNA levels were analyzed by RT–qPCR in samples treated as in A ($n = 3$ independent experiments).
C Gli4 cells were treated as in A prior to WB analysis using indicated antibodies.
D *IFNB* and *CXCL10* mRNA levels were analyzed by RT–qPCR in samples treated as in C ($n = 3$ independent experiments).
E Phorbol 12-myristate 13-acetate (PMA)-treated THP1 cells were incubated for 24 h with conditioned media derived from T98G cells treated or not with dsDNA. *IFIT1*, *IFIT2*, *MXA*, *OAS1* mRNA levels were analyzed by RT–qPCR. Graphs present a representative biological triplicate ($n = 3$ independent experiments).
F T98G cells were challenged or not with dsDNA for 6 h, in the presence or not of the NU7441 DNA-PKcs inhibitor, prior WB analysis using indicated antibodies.
G *IFNB* and *CXCL10* mRNA levels were analyzed by RT–qPCR in samples treated as in F ($n = 4$ independent experiments).
H T98G cells were treated with non-targeting (CTRL) or DNA-PKcs-targeting siRNAs for 72 h prior to 6 h challenge with dsDNA. *IFNB* and *CXCL10* mRNA levels were analyzed by RT–qPCR. Graphs present a representative biological triplicate ($n = 3$ independent experiments).
I T98G cells were treated or not with 0.16 μM camptothecin (CPT) for 48 h prior to immunofluorescence analysis using dsDNA- and 53BP1-specific antibodies, and DAPI nuclear staining ($n = 3$ independent experiments). Scale bar, 20 μm.
J Whole cell extracts from T98G cells treated or not for 72 h with 0.16 μM CPT were analyzed by WB using indicated antibodies.
K *IFNB* and *CXCL10* mRNA levels were analyzed by RT–qPCR in samples treated as in J ($n = 3$ independent experiments).
L T98G cells were treated or not with 0.16 μM CPT for 72 h, in presence or not of NU7441, prior to assessment of *IFNB* and *CXCL10* mRNA levels by RT–qPCR. Graphs present a representative biological triplicate ($n = 3$ independent experiments).

Data information: All immunoblots are representative experiments ($n = 3$ independent experiments). All graphs present means ± standard error from the mean (SEM). *P*-values were determined by Student's *t*-test. ns: not significant. *$P < 0.05$, **$P < 0.01$, ***$P < 0.001$, ****$P < 0.0001$.
Source data are available online for this figure.

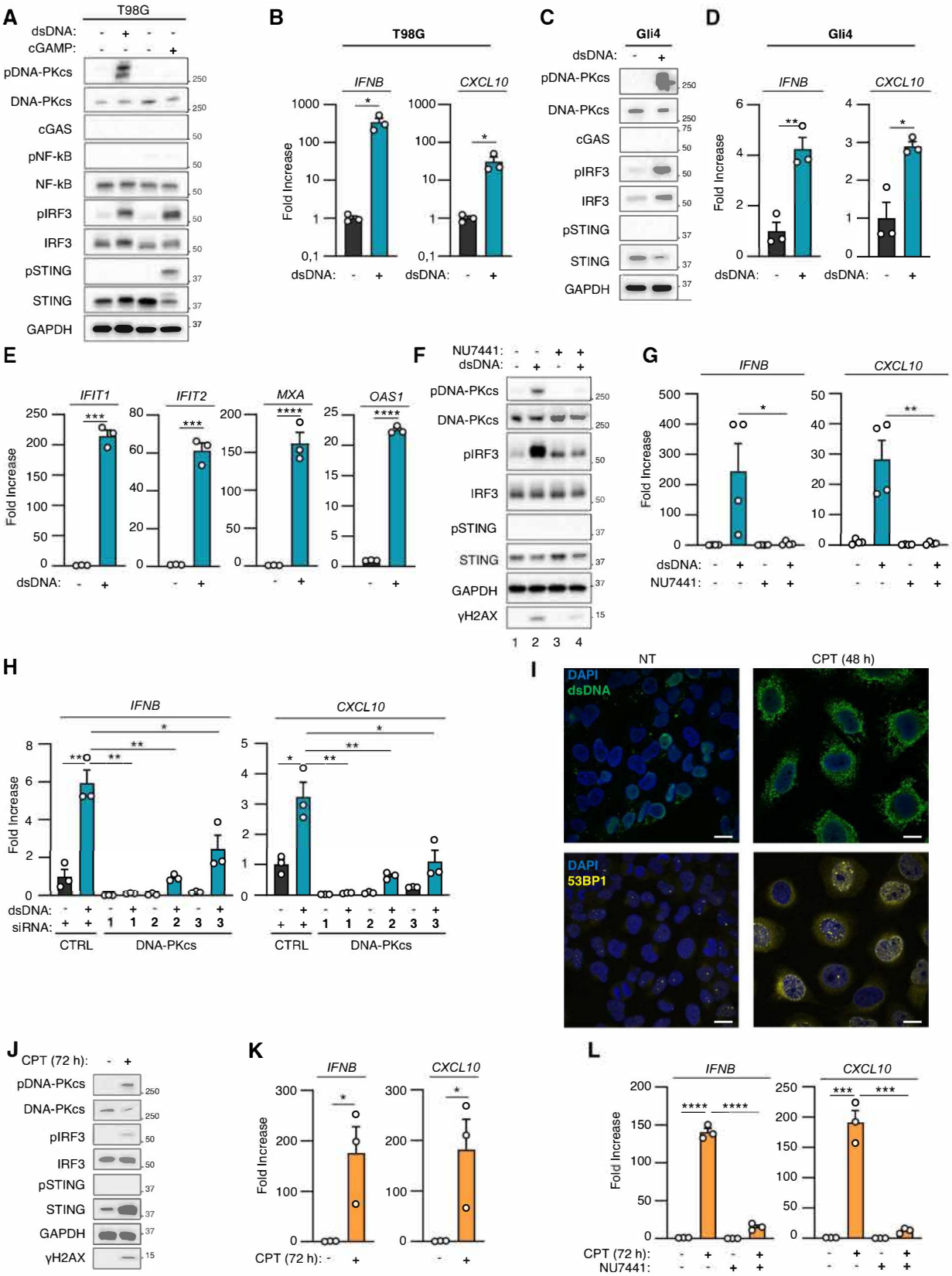

Figure 1.

with dsDNA led to DNA-PKcs phosphorylation (Figs 1A and C, and EV1B and D). Second, we tested whether DNA-PK is responsible for type I IFN responses in the absence of cGAS in glioblastoma cells by treating T98G, Gli4, and GSC9 with the NU7441 DNA-PKcs inhibitor. WB analysis showed that treatment with NU7441 inhibited dsDNA-induced DNA-PKcs auto-phosphorylation and decreased phosphorylation of the H2AX DNA-PK substrate (Figs 1F and EV1G compare lanes 2 and 4), attesting to efficient DNA-PKcs inhibition. NU7441 treatment also led to a decrease of pIRF3 (Figs 1F and EV1G), *IFNB* and *CXCL10* levels (Figs 1G and EV1F and H). Finally, T98G cells were treated with scrambled or DNA-PKcs-targeting siRNAs prior to analysis of dsDNA-dependent type I IFN responses. Knock-down of DNA-PKcs in T98G cells (Fig EV1I) abrogated dsDNA-induced type I IFN responses (Fig 1H). Thus, DNA-PKcs drives dsDNA-induced type I IFN responses in glioblastoma cells.

DNA-PK controls genotoxic stress-induced type I Interferon responses in absence of cGAS

Previous work has shown that in myeloid cells, DNA-PKcs does not induce genotoxic stress-associated type I IFN responses (Burleigh *et al*, 2020). Here, we questioned whether DNA-PK may be involved in genotoxic stress-associated type I IFN responses in cancer cells that do not express detectable cGAS levels. To this aim, T98G cells were treated with the camptothecin genotoxic agent to induce dsDNA breaks that are primarily repaired by NHEJ (Adachi *et al*, 2004). Staining with a dsDNA-specific antibody showed that such treatment is sufficient to induce cytosolic accumulation of dsDNA (Fig 1J, upper panels) together with accumulation of 53BP1 foci in the nucleus and in the cytosol, reflecting defective repair and accumulation of DNA lesions (Fig 1I, lower panels) (Gonzalez-Suarez *et al*, 2011). WB analysis showed that camptothecin treatment led to increased pDNA-PKcs, and pIRF3, but not pSTING (Fig 1J), together with increased levels of *IFNB* and *CXCL10* (Fig 1K). This suggests that DNA-PK may be responsible for cGAS-independent type I IFN responses following genotoxic stress in T98G cells.

We next treated T98G cells with camptothecin in the presence of NU7441. Since NU7441 inhibits the catalytic activity of DNA-PKcs, as reflected by decreased pDNA-PKcs (Fig EV1J), such treatment presumably impacts both DNA-PK-mediated DNA repair and signaling. Consequently, treatment with NU7441 alone was sufficient to promote the accumulation of DNA damage, as confirmed by the presence of 53BP1 foci and of cytosolic dsDNA (Fig EV1K), without triggering type I IFN responses, as attested by the absence of *IFNB* and *CXCL10* upregulation (Fig 1L). However, treatment with NU7441 abrogated camptothecin-associated *IFNB* and *CXCL10* induction (Fig 1L). Similarly, we found that NU7441 inhibited type I IFN responses elicited by treatment with the etoposide genotoxic agent (Fig EV1L). Thus, altogether, these data support that DNA-PKcs is responsible for genotoxic stress-dependent activation of type I IFN responses in T98G cells.

DNA-PK-dependent detection of cytosolic dsDNA drives STING-independent IRF3-dependent type I IFN responses in cancer cells lacking cGAS

We next questioned the molecular mechanisms involved in DNA-PK-dependent type I IFN responses following challenge with exogenous dsDNA or genotoxic stress. First, immunofluorescence analysis showed that, following dsDNA challenge in T98G and Gli4 cells, activated DNA-PKcs is found in the cytosol (Figs 2A and EV2A), suggesting DNA-PKcs translocation into the cytosol, as previously reported upon UV treatment (Tu *et al*, 2013). Second, we assessed the ability of DNA-PK to interact with cytosolic dsDNA. To this aim, we used 80 nt-long dsDNA or ssDNA, bearing a 5′ biotin on the sense strand to perform streptavidin-affinity pull-down experiments using whole cell extracts from T98G cells. We thereby observed that DNA-PKcs, KU80, and KU70 are recruited to dsDNA (Fig 2B). Similar experiments were performed following 6 h of biotinylated dsDNA transfection in the THP-1 human myeloid cell line (Fig EV2B), a time point at which transfected dsDNA are found in the cytosol (Guerra *et al*, 2020). In these conditions, together with DNA-PKcs, KU70, and KU80, recruitment of pDNA-PKcs to dsDNA was also observed (Fig EV2B). Combined, these experiments support that DNA-PK is recruited to cytosolic dsDNA.

We next tested whether the interaction of KU70:KU80 with dsDNA was required for DNA-PKcs-dependent type I IFN responses. To this aim, we performed KU70 knock-down (Fig 2C), prior to

Figure 2. DNA-PK-dependent detection of cytosolic dsDNA drives STING-independent IRF3-dependent type I IFN responses in cancer cells lacking cGAS.

A T98G cells were treated or not with dsDNA for 6 h prior to immunofluorescence analysis using DNA-PKcs- and pDNA-PKcs-specific antibodies, and DAPI nuclear staining ($n = 3$ independent experiments). Scale bar, 20 μm.

B Whole cell extracts from T98G cells were incubated with 80 nt-long biotinylated ssDNA or dsDNA prior to pull-down using streptavidin-affinity beads. Input and eluates were analyzed by WB using indicated antibodies.

C T98G cells were treated with non-targeting (CTRL) or KU70-targeting siRNAs prior to whole cell extract preparation, and pull-down as in (B). Inputs and eluates were analyzed by WB using indicated antibodies.

D T98G cells were treated with CTRL or KU70-targeting siRNAs prior to challenge with dsDNA for 6 h. *IFNB* and *CXCL10* mRNA levels were analyzed by RT–qPCR. Graphs present a representative biological triplicate ($n = 3$ independent experiments).

E CTRL or *STING*$^{-/-}$ T98G cells were transfected or not with dsDNA for 8 h prior to analysis of *IFNB* and *CXCL10* mRNA levels ($n = 3$ independent experiments).

F As in (E), except that CTRL or *IRF3*$^{-/-}$ T98G cells were transfected or not with dsDNA for 6 h prior to analysis ($n = 3$ independent experiments).

G CTRL or *STING*$^{-/-}$ T98G cells were treated or not with CPT for 72 h prior to analyses of *IFNB* and *CXCL10* mRNA levels ($n = 3$ independent experiments).

H As in (G), except that CTRL and *IRF3*$^{-/-}$ T98G cells were used. Graphs present a representative biological triplicate ($n = 3$ independent experiments). Schematic representation of cytosolic dsDNA-dependent type I IFN induction in T98G cells.

Data information: All immunoblots are representative experiments ($n = 3$ independent experiments). All graphs present means ± SEM. *P*-values were determined by Student's *t*-test. ns: not significant. $^{**}P < 0.01$, $^{***}P < 0.001$, $^{****}P < 0.0001$.
Source data are available online for this figure.

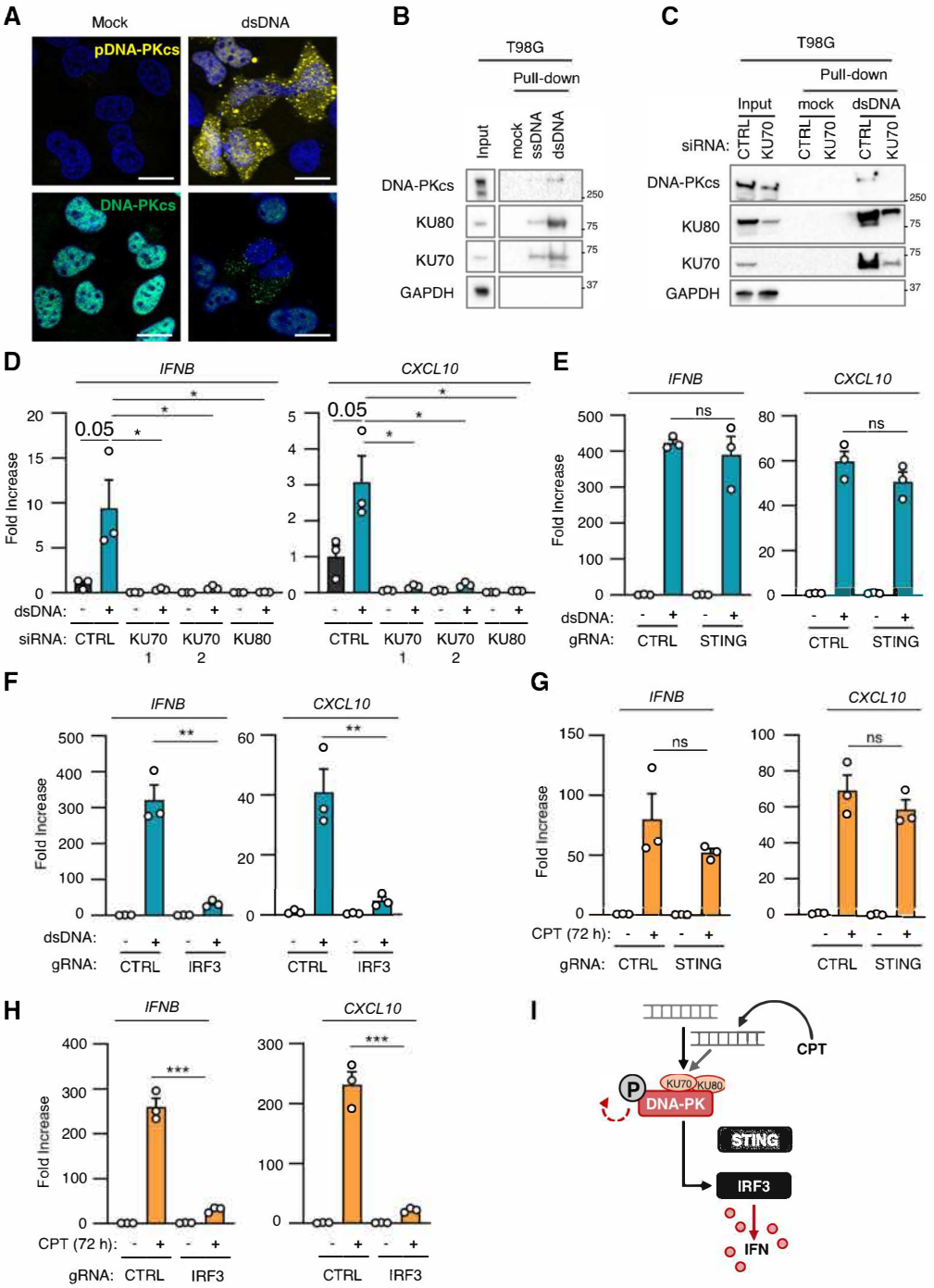

Figure 2.

assessment of the recruitment of DNA-PK to dsDNA. Knock-down of KU70 decreased the recruitment of KU80 while abolishing the recruitment of DNA-PKcs to dsDNA (Fig 2C). Of note, the total protein levels of KU80 and DNA-PKcs were also decreased following KU70 knock-down, likely reflecting destabilization of DNA-PK complexes following KU70 depletion as previously reported (Gu *et al*, 1997, Nussenzweig *et al*, 1996). Conversely, performing dsDNA pull-down using whole cell extracts from control ($HCT116^{CTRL}$) and DNA-PKcs-deficient HCT116 ($HCT116^{PRKDC-/-}$) cells showed that DNA-PKcs is not required for the recruitment of KU70 and KU80 to dsDNA (Fig EV2C). Importantly, knock-down of KU70 and KU80 (Fig EV2D) also abolished dsDNA-induced *IFNB* and *CXCL10* expression in T98G cells (Fig 2D). Thus, these data demonstrate that the recruitment of DNA-PKcs to cytosolic dsDNA through the KU70:KU80 heterodimer is required to trigger type I IFN responses.

WB analyses of STING protein levels and phosphorylation status in glioblastoma cells (Figs 1 and EV1) suggest that the DNA-PK-dependent type I IFN responses elicited by dsDNA transfection are STING-independent. To formally test the requirement for STING, we

generated STING-deficient T98G cells (T98G$^{STING-/-}$) (Fig EV2E and F) where we assessed dsDNA-induced type I IFN responses (Figs 2E and EV2G). Challenge with dsDNA of T98G$^{STING-/-}$ and of their control counterparts (T98G^{CTRL}) promoted IRF3 phosphorylation (Fig EV2G), together with *IFNB* and *CXCL10* upregulation (Fig 2E), regardless of STING expression. The presence of phosphorylated IRF3 following dsDNA challenge in absence of detectable cGAS (Figs 1A and C, and EV1B and D) also suggested that DNA-PK-associated IFN responses require IRF3. To confirm this requirement, IRF3-deficient T98G cells (T98G$^{IRF3-/-}$) (Fig EV2H) were challenged with dsDNA prior to assessment of type I IFN responses. Absence of IRF3 disrupted type I IFN responses in T98G cells (Figs 2F and EV2H), supporting that DNA-PK-dependent, STING-independent, type I IFN responses require IRF3 in cancer cells presenting undetectable cGAS levels.

We next analyzed whether genotoxic stress-induced DNA-PK-dependent type I IFN responses in absence of detectable cGAS levels are governed by similar molecular mechanisms. To this aim, T98G^{CTRL}, T98G$^{STING-/-}$, and T98G$^{IRF3-/-}$ were treated with camptothecin prior to analysis of DNA-PK activation and IFN responses. Similar to what was observed upon challenge with dsDNA, genotoxic stress induced DNA-PKcs phosphorylation, regardless of the expression of STING and IRF3 (Fig EV2I and J). In addition, while induction of type I IFN responses did not require the expression of STING (Fig 2G), the presence of IRF3 was required (Fig 2H). Thus, DNA-PKcs controls genotoxic stress-induced type I IFN responses through IRF3 activation.

Finally, we questioned whether cGAS-independent DNA-PK-associated type I IFN responses can be observed in other cell lines. To this aim, we used cGAS-knockout THP-1 cells (THP-1$^{cGAS-/-}$) and observed that, challenged with dsDNA, induced type I IFN responses (Fig EV2K and L), concomitantly to DNA-PKcs phosphorylation (Fig EV2K). However, STING ablation abolished type I IFN responses in THP-1 cells (Fig EV2K and L). Thus, in contrast to T98G cells, STING is indispensable for type I IFN responses in myeloid cells, suggesting that the requirement for STING in DNA-PK activation is cell type specific. Thus DNA-PKcs drives cytosolic dsDNA-IFN responses through IRF3 (Fig 2I).

cGAS and DNA-PKcs cooperate for optimal dsDNA-induced type I Interferon responses

Considering that DNA-PK can elicit type I IFN responses in absence of cGAS, we next interrogated the impact of co-expressing DNA-PKcs and cGAS in glioblastoma cells. To this aim, we generated T98G cells stably expressing cGAS (T98G^{cGAS}) or not (T98G^{Empty}) (Fig 3A). Expression of cGAS was sufficient to induce constitutive degradation of STING (Fig 3A, compare lanes 3 to 1) and to promote increased basal *IFNB* and *CXCL10* levels (Fig 3B). Additionally, challenge with dsDNA led to enhanced pIRF3 levels together with increased induction of type I IFN responses (Fig 3A and B), indicating that the cGAS-STING axis is efficiently restored in T98G^{cGAS} cells. Similar to what was observed in T98G cells, dsDNA transfection induced cytosolic accumulation of pDNA-PKcs (Fig EV3A). Knowing the strong affinity of cGAS for cytosolic dsDNA (Zhou *et al*, 2018), we addressed whether DNA-PK and cGAS can compete for dsDNA detection, by transfecting biotinylated dsDNA in T98G^{Empty} and T98G^{cGAS} or in THP-1^{CTRL} and THP-1$^{cGAS-/-}$ prior to streptavidin-affinity pull-down. WB analysis showed that the recruitment of subunits of DNA-PK to dsDNA is not altered in the presence of cGAS, except an increase of KU70 associated with dsDNA in T98G^{Empty} as compared to T98G^{cGAS} (Figs 3C and EV3B). Next, we transfected limiting amounts of dsDNA in T98G^{Empty} and T98G^{cGAS} prior to pull-down and assessment of the binding of DNA-PK subunits. Although increasing amounts of dsDNA led to increased cGAS recruitment to dsDNA, recruitment of DNA-PKcs and KU70 appeared unaltered. To the contrary, KU80 binding to pulled-down dsDNA appeared to increase with lower levels of dsDNA (Fig EV3C). Yet, to activate DNA-PKcs-dependent phosphorylation, subunits of DNA-PK work as an heterotrimer in which

Figure 3. cGAS and DNA-PKcs cooperate for optimal dsDNA-induced type I Interferon responses.

A T98G cells stably expressing cGAS (T98G^{cGAS}) or not (T98G^{Empty}) were transfected or not with dsDNA for 6 h prior to whole cell extraction and WB analysis using indicated antibodies.

B *IFNB* and *CXCL10* mRNA levels were analyzed by RT–qPCR in samples treated as in (A). Graphs present a representative biological triplicate (n = 5 independent experiments).

C T98G^{Empty} and T98G^{cGAS} were transfected or not with biotinylated dsDNA prior to whole cell extraction and pull-down using streptavidin-affinity beads. Inputs and eluates were analyzed by WB using indicated antibodies.

D T98G^{Empty} and T98G^{cGAS} were transfected or not with dsDNA for 6 h in the presence or not of NU7441 prior to *IFNB* and *CXCL10* expression analysis. Graphs present a representative biological triplicate (n = 5 independent experiments).

E T98G^{Empty} and T98G^{cGAS} were treated or not with CPT for 72 h in combination or not with NU7441 (48 h) prior to *IFNB* and *CXCL10* expression analysis. Graphs represent a biological triplicate (n = 4 independent experiments).

F THP-1^{CTRL} and THP-1$^{cGAS-/-}$ were transfected or not with dsDNA for 6 h in presence or not of NU7441 prior to *IFNB* and *CXCL10* expression analysis (n = 3 independent experiments).

G Intracellular cGAMP levels were analyzed in samples treated as in (E) by ELISA (n = 3 independent experiments).

H Intracellular cGAMP levels were analyzed in samples treated as in (F) by ELISA. Graphs present a representative biological triplicate (n = 2 independent experiments).

I T98G expressing a catalytic dead cGAS allele (T98G$^{cGAS\text{-}CD}$) and T98G were treated as in (A) prior to *IFNB* and *CXCL10* levels analysis. Graphs present a representative biological triplicate (n = 3 independent experiments).

J T98G^{cGAS} were transfected or not with dsDNA in presence or not of NU7441, prior to WB analysis using indicated antibodies.

K THP-1 were transfected or not with dsDNA in presence or not of NU7441, prior to WB analysis using indicated antibodies.

L Schematic representation of the molecular mechanisms involved in the cooperation between DNA-PKcs and cGAS for type I IFN induction.

Data information: All immunoblots are representative experiments (n = 3 independent experiments). All graphs present means ± SEM. P-values were determined by Student's t-test. ns: not significant. *P < 0.05, **P < 0.01, ***P < 0.001, ****P < 0.0001.
Source data are available online for this figure.

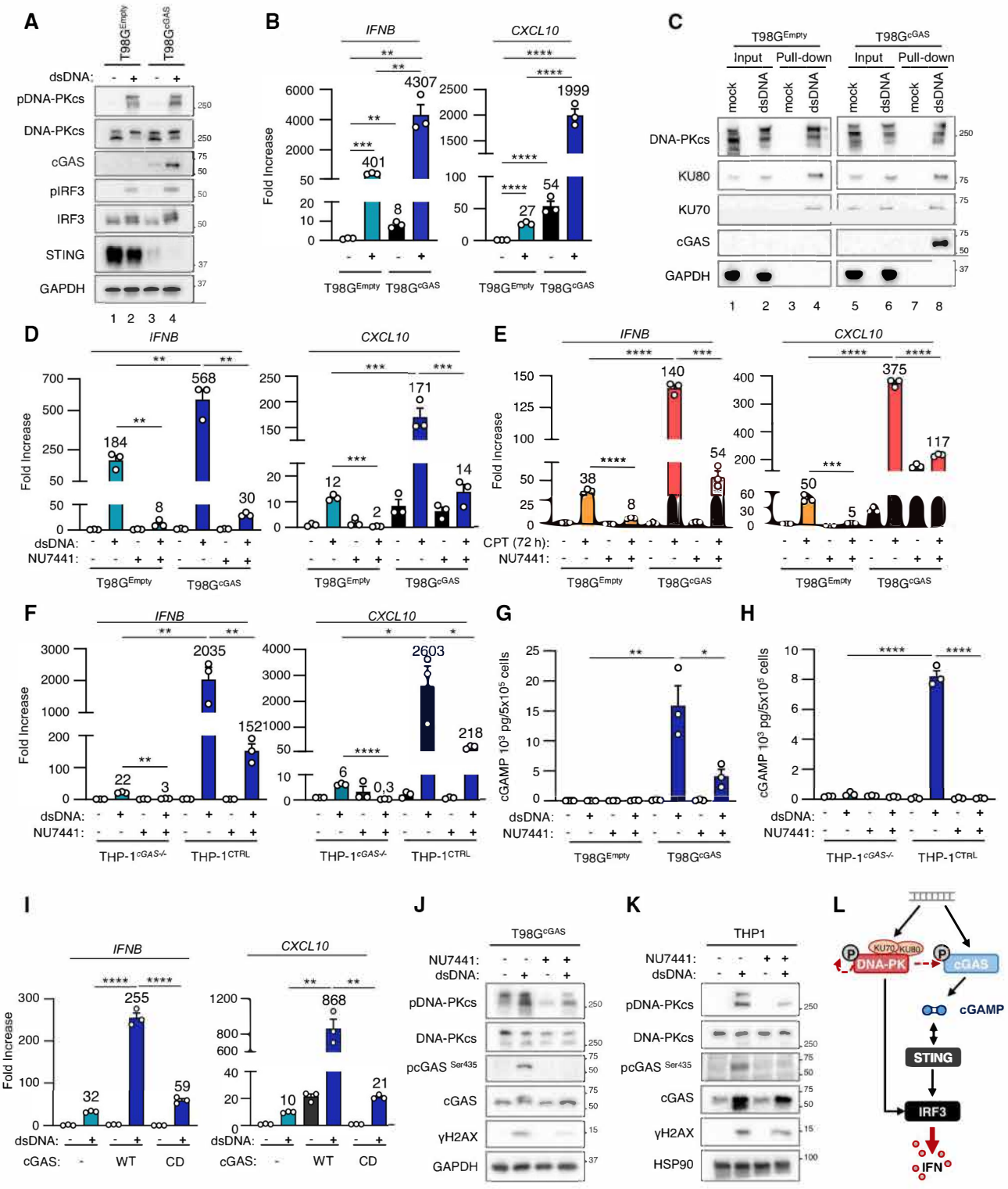

Figure 3.

DNA-PKcs is the limiting factor (Hammarsten & Chu, 1998, West *et al*, 1998). Thus, expressing cGAS in T98G cells restores the cGAS-STING signaling axis without modifying the interaction of DNA-PK with dsDNA ligands.

Given that both cGAS and DNA-PK can detect cytosolic DNA when co-expressed, we next questioned their respective contribution to dsDNA-dependent induction of type I IFN responses. To this aim, T98G^{Empty} and T98G^{cGAS} were either transfected with dsDNA

or treated with camptothecin, in the presence or not of NU7441, prior to evaluation of type I IFN responses. Intriguingly, treatment with NU7441 led to a dramatic decrease of *IFNB* and *CXCL10* expression, both in the presence and absence of cGAS, following dsDNA transfection (Figs 3D and EV3D). Similarly, treatment with camptothecin led to higher type I IFN responses in the presence of cGAS, which were abolished by treatment with NU7441 (Fig 3E). This suggested that DNA-PK and cGAS cooperate for the induction of type I IFN responses, when co-expressed. We interrogated whether a similar cooperation could be witnessed in other cell lines, using THP-1, but also the CFPAC pancreatic cancer cell line, and their *cGAS*$^{-/-}$ counterparts. Treatment with NU7441 also led to a dramatic decrease of type I IFN responses to dsDNA in both cell types, regardless of the expression of cGAS (Figs 3F and EV3E–G). We next assessed whether the cooperation between cGAS and DNA-PK is operational in murine cell lines. To this aim, mouse embryonic fibroblast (MEF) and their *cGas*-deficient counterpart, as well as the GL261 murine glioblastoma cell line knockout or not for *cGas* were transfected or not with dsDNA in the presence or not of NU7441. We thereby observed that in these murine cell lines, type I IFN responses are potentialized when cGAS and DNA-PK are both functional (Fig EV3H–J). Thus, our data suggest that the mechanism through which DNA-PK and cGAS synergize is conserved in murine models.

To identify the molecular mechanism through which cGAS and DNA-PK cooperate, we tested whether DNA-PK can control cGAS activity. To this aim, we quantified intracellular cGAMP levels in T98G^{Empty} and T98G^{cGAS}, but also in THP-1^{CTRL} and THP-1$^{cGAS-/-}$ cells, upon challenge with dsDNA in the presence or not of NU7441. Treatment with NU7441 led to a decrease of cGAMP levels in both T98G^{cGAS} and THP-1 cells (Fig 3G and H), although NU7441 did not alter cGAS activity *in vitro* (Fig EV3K). Finally, when T98G stably expressing a catalytic-dead cGAS allele (T98G$^{cGAS-CD}$) were challenged with dsDNA, type I IFN responses were drastically reduced as compared to those witnessed in T98G^{cGAS} (Figs 3I and EV3L). These data show that the cooperation between cGAS and DNA-PK operates at the level of cGAS activity, and strongly suggest that DNA-PKcs boosts the production of cGAMP by cGAS.

Phosphorylation of the Serine 435 (Ser435) of cGAS has been previously shown to be required to enable cGAS-dependent cGAMP production (Li & Shu, 2020). Because DNA-PKcs bears a Serine/Threonine kinase activity, we asked whether DNA-PKcs could be responsible for this phosphorylation. Challenge with dsDNA of cGAS-proficient cells (namely T98G^{cGAS}, THP-1, and CFPAC) showed that the phosphorylation of cGAS on Ser435 was lost upon DNA-PKcs inhibition by NU7441 (Figs 3J and K and EV3F). This supports that DNA-PKcs catalytic activity is required for cGAS phosphorylation at Ser435. Thus, altogether these data show that DNA-PKcs is required for efficient cGAS-dependent cGAMP production (Fig 3L).

cGAS re-expression in glioblastoma cancer cells promotes macrophage recruitment and impairs tumorigenesis

We next questioned whether the synergy between cGAS and DNA-PK could have an impact on glioblastoma tumor immunogenicity. First, because cGAS has been previously shown to alter proliferation (Wang *et al*, 2015, Yang *et al*, 2017), we assessed the growth of T98G^{Empty} and T98G^{cGAS} in 2D and 3D cultures. Follow-up over time showed that cGAS re-expression did not alter the proliferation of T98G cells (Fig 4A and B), nor affected their ability to form spheroids (Fig 4C), ruling out cell-intrinsic defects. However, upon subcutaneous engraftment in nude mice, T98G^{cGAS} failed to form tumors (Fig 4D and E). To visualize early steps of tumorigenesis, we next used zebrafish embryos in which we performed orthotopic transplantation of T98G^{Empty} and T98G^{cGAS} stably expressing a green fluorescence protein (GFP) reporter (T98G-GFP^{Empty} and T98G-GFP^{cGAS}). Monitoring of the intracranial GFP signal over time showed a faster decrease of the T98G-GFP^{cGAS} tumor mass, as compared to T98G-GFP^{Empty} tumors (Fig 4F). Moreover, morphological assessment of tumors showed more elongated pseudopodia, which are hallmarks of invasiveness (Lah *et al*, 2020), in T98G-GFP^{Empty} tumors as compared to T98G-GFP^{cGAS} (Fig EV4A and B). Thus, cGAS expression in T98G cells is sufficient to impair early tumorigenesis.

Since nude mice and zebrafish embryos, at the stage at which they were engrafted, do not possess an adaptive immune system, we next hypothesized that differential cytokine and chemokine production may modulate myeloid cell activity in the glioblastoma microenvironment. Migration assays showed that conditioned media from T98G^{cGAS} cells increased the migration of THP-1 cells as compared to that from T98G^{Empty} cells (Fig 5A). However, conditioned media from T98G^{cGAS} cells was not sufficient to promote THP-1 and primary myeloid cell polarization (Fig EV5A and B). Thus, soluble factors secreted by T98G^{cGAS} are sufficient to promote the recruitment of myeloid cells to the tumor mass, but not their polarization. To identify those soluble factors, we profiled cytokines and chemokines levels, using the proteome profiler qualitative array, in the supernatant of T98G^{Empty} and T98G^{cGAS}, thereby identifying C-C Motif Chemokine Ligand 2 (CCL2) and 5 (CCL5), in addition to CXCL10, as most upregulated in the supernatant of T98G^{cGAS} as compared to T98G^{Empty} cells (Fig 5B). Such upregulation was also observed at the gene expression level (Fig 5C) and was lost when comparing T98G^{cGAS} to T98G$^{cGAS-CD}$ (Fig EV5C). To assess whether DNA-PK and cGAS synergize to induce the expression of these genes, we next assessed the expression of *CCL2* and *CCL5* upon dsDNA stimulation in the presence or not of NU7441. Such analyses revealed that while NU7441 treatment abolished the expression of *CCL2* in the presence or absence of cGAS, it did not abolish cGAS-induced *CCL5* expression (Fig EV5D). Interestingly, we also observed that DNA-PK and cGAS appear to synergize to induce the expression of type III IFNs (*IFNL2/3*), *CCL3* and interleukin 6 (*IL-6*) (Fig EV5E). This suggests that while cGAS and DNA-PK synergize to induce the expression of certain genes, there are likely additional parameters controlling gene activation downstream of these two receptors. Furthermore, these data support that the synergy between DNA-PK and cGAS promotes the production of chemokines that can induce macrophage recruitment.

We thus took advantage of the optical traceability of macrophages in the *tg(mfap4:RFP)* zebrafish line, owing to the expression of a red fluorescent protein (RFP) reporter under the control of the *mfap4* promoter. Imaging over time showed enhanced recruitment of myeloid cells around and inside tumors of zebrafish embryos injected with T98G-GFP^{cGAS}, as compared to those injected with

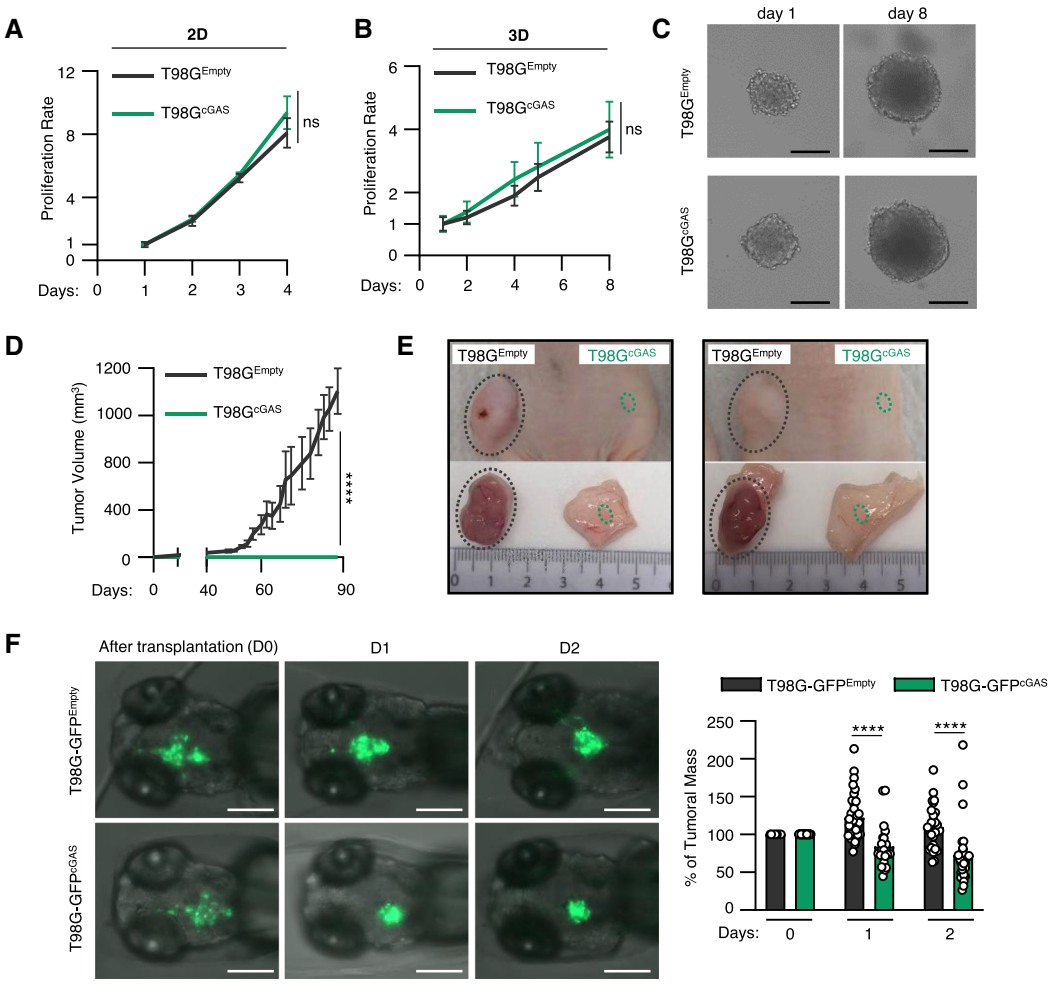

Figure 4. cGAS re-expression in glioblastoma cancer cells impairs tumorigenesis.

A The proliferation of T98G^{Empty} and T98G^{cGAS} was monitored in 2D cultures over 4 days ($n = 3$ independent experiments).

B The volume of spheroids formed by T98G^{Empty} and T98G^{cGAS} was monitored over 8 days ($n = 3$ independent experiments).

C Representative images of T98G^{Empty} and T98G^{cGAS} spheroids measured in (B), at day 1 and day 8. Scale bar, 250 µm.

D The volume of subcutaneous T98G^{Empty} and T98G^{cGAS} tumors in nude mice was measured every 3–4 days by caliper ($n = 6$ mice per group).

E Representative pictures of T98G^{Empty} and T98G^{cGAS} tumors from D, at day 90 post subcutaneous engraftment.

F T98G^{Empty} and T98G^{cGAS} stably expressing a GFP reporter (T98G-GFP^{Empty} and T98G-GFP^{cGAS}, respectively) were xenotransplanted into the head of *tg(mfap4:RFP)* zebrafish line at 3 days post fertilization (dpf). Zebrafish embryos were imaged daily over 3 days. The graph represents the mean (± SEM) percentage of tumor growth normalized by the area on the day of transplantation ($n = 21$ T98G-GFP^{Empty} and $n = 29$ T98G-GFP^{cGAS} embryos). Scale bar, 200 µm.

Data information: All graphs present means ± SEM. *P*-values were determined by Student's *t*-test. ns: not significant. *$P < 0.05$, **$P < 0.01$, ****$P < 0.0001$. One-way Anova with Tukey's multiple comparisons test was used for mice analyses. Mann–Withney test was performed to analyze tumor growth in zebrafish.
Source data are available online for this figure.

T98G-GFP^{Empty} (Fig 5D). Quantification of contacts between tumors and myeloid cells further supported increased recruitment and interaction between tumor masses formed of T98G-GFP^{cGAS} and myeloid cells, as compared to T98G-GFP^{Empty} tumor masses (Fig 5D and E). In addition, assessment of macrophage polarization markers showed increased expression of M1 markers in zebrafish heads where T98G-GFP^{cGAS} were injected, as compared to T98G-GFP^{Empty} tumors (Fig 5F). Thus, these data suggest that cGAS re-expression in T98G cells may be sufficient to promote macrophage recruitment and M1 polarization at the tumor site, impairing tumor engraftment and promoting tumor clearance.

cGAS and DNA-PKcs levels increase with tumor grade

To confirm the physiological relevance of our findings that indicate that cGAS expression impairs early tumorigenesis, we first performed a meta-analysis of glioblastoma tumors, using the GlioVis database (Bowman *et al*, 2017). We examined the co-expression of *PRKDC* and *MB21D1* (encoding cGAS) in glioblastoma tissue samples from the CGGA transcriptomic database. Of the 224 retrieved cases, three statistically well-represented populations were determined based on *PRKDC* and *MB21D1* expression levels: *PRKDC*^{low}/*MB21D1*^{low}, *PRKDC*^{high}/*MB21D1*^{low}, and *PRKDC*^{high}/*MB21D1*^{high}

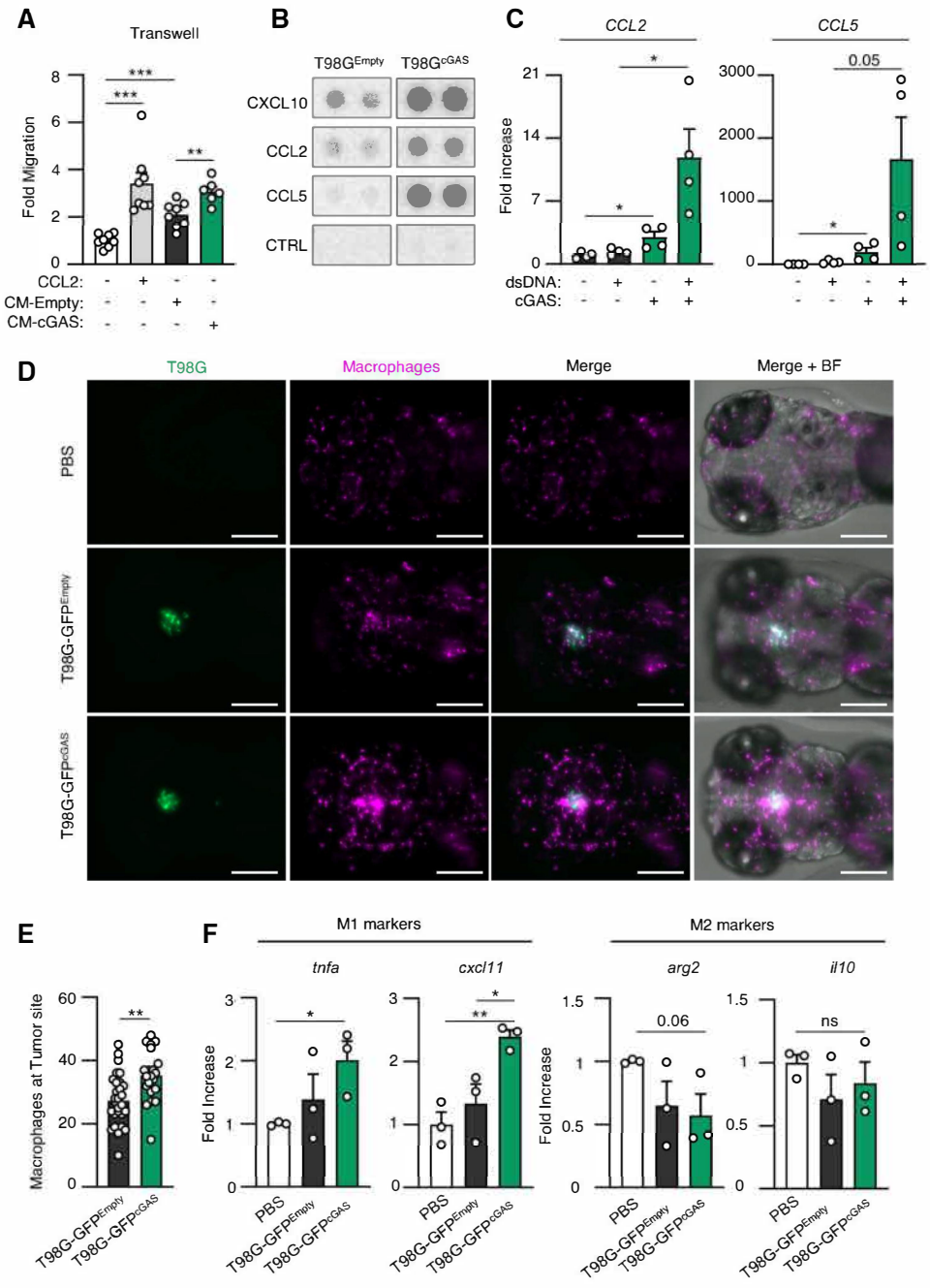

Figure 5. cGAS re-expression in glioblastoma cancer cells promotes macrophage recruitment.

A Graph represents the mean (± SEM) fold migration of THP-1 cells through a 3 μm transwell insert when conditioned media from T98G^{Empty} or T98G^{cGAS} was applied to lower chamber for 6 h. CCL2 was used as positive control (n = 8 biological replicates).

B CXCL10, CCL2 and CCL5 protein levels in conditioned media from T98G^{Empty} and T98G^{cGAS} cells were assessed using proteome profiler. Proteins that were found to be the most upregulated in T98G^{cGAS} are shown. Representative immunoblots (n = 3 independent experiments).

C T98G^{Empty} and T98G^{cGAS} were transfected or not with dsDNA prior to analyses of *CCL2* and *CCL5* by RT–qPCR (n = 4 independent experiments).

D Zebrafish embryos injected with T98G-GFP^{Empty}, T98G-GFP^{cGAS}, or PBS at 3 dpf (Fig 4E) were imaged at 24 h post transplantation. Representative images of macrophage recruitment (purple) in the head (n = 21 T98G-GFP^{Empty} and n = 29 T98G-GFP^{cGAS} embryos). Scale bar, 200 μm.

E Graph presents the quantification of macrophages recruited at tumor site 24 h post xenotransplantation in (D) (n = 21 T98G-GFP^{Empty} and n = 29 T98G-GFP^{cGAS} embryos).

F Heads of zebrafish treated as in (D) were isolated prior to RNA extraction and analysis of M1 (*tnfa* and *cxcl11*) or M2 (*arg2* and *il10*) polarization markers. Each value in the graph is the mean of 25 embryos.

Data information: All graphs present means ± SEM. P-values were determined by Student's t-test. ns: not significant. *P < 0.05, **P < 0.01, ****P < 0.0001. Mann–Whitney test was performed to analyze macrophage recruitment in zebrafish.
Source data are available online for this figure.

(Fig 6A). Owing to the low number of patients presenting a *PRKDC*^{low}/*MB21D1*^{high} profile, those were not included in the analysis. Analysis of mRNA levels of total macrophages, chemokines/cytokines, and macrophage polarization markers was performed between these groups. We found that expression of *MB21D1* correlated with high expression of *CXCL10*, *CCL2* and *CCL5* chemokines (Fig 6B) and with the increased presence of macrophages (Fig 6C–E). Calculating M1/M2 ratios did not reveal any significant enrichment of a specific subpopulation (Fig 6F). Consistent with Pan-cancer analysis (An *et al*, 2019), analysis of patient survival showed that higher *MB21D1* expression led to worst patient survival as compared to patients with low *MB21D1* expression, supporting that expression of cGAS is a poor outcome marker in glioblastoma (Fig 6G). In addition, analysis of *PRKDC* and *MB21D1* expression in glioblastoma of grades II, III, and IV, indicates that *PRKDC* and *MB21D1* expression increased significantly with the aggressiveness of the tumors (Fig 6H). Next, we performed immunohistochemistry analyses of surgical specimens of human brain tumors (Fig 6I). This showed a positive correlation between cGAS and DNA-PKcs protein levels (Table 1) and increased levels of both proteins with tumor grade (Table 2). Thus, altogether, our data support that DNA-PK and cGAS cooperate to foster a pro-inflammatory environment, by enhancing the production of cytokines and chemokines that attract macrophages to the tumor vicinity, a process that inhibits early tumorigenesis, but fuels cancer-associated inflammation at later stages (Fig 6J).

Discussion

We demonstrate that DNA-PK and cGAS synergize for the production of type I IFNs and chemokines, thus dictating the composition of the tumor microenvironment. This cooperation is therefore an attractive target to modulate tumor immunogenicity. Our data further reveal that the molecular determinants of the activation of DNA-PK-dependent signaling are governed by cell-type specific rules, that, if adequately harnessed, may allow targeting inflammatory responses in specific cells of the tumor microenvironment.

Intriguingly, previous reports have shown that DNA-PKcs can inhibit cGAS activation by direct modulation of its phosphorylation of T68 and S213 (Sun *et al*, 2020) or by inducing cytosolic translocation of PARP1 (Wang *et al*, 2022). While seemingly contradictory with our findings and the recently published description of a requirement for KU subunits for optimal cGAS activation (Tao *et al*, 2022), these studies mostly focused on the role played by DNA-PK-associated inflammatory responses in the context of HSV-1 infection. In that context, it is possible that HSV-1-associated factors and additional cellular perturbations promote activation of pathways that eventually bypass the initial requirement of DNA-PK-dependent activation of cGAS. In addition, our study mostly focused on the study of acute nucleic acid challenge, while HSV-1 infection is monitored at 16 h post infection. In this context, one may hypothesize that at early time points upon challenge with immune-stimulatory nucleic acid species, DNA-PK activation is required for priming cGAS activation, while at later time points, DNA-PK activity may be required to prevent overactivation of inflammatory responses. This ultimately indicates that assessment of the crosstalk between nucleic acid detection pathways necessitates investigation in a time-dependent manner.

Tumor-associated macrophages are the most abundant immune cell population in the glioblastoma tumor microenvironment (Buonfiglioli & Hambardzumyan, 2021) and their presence is generally an indicator of poor outcomes for glioblastoma patients (Wei *et al*, 2020). In agreement, blocking macrophage recruitment through *Ccl2* genetic ablation ameliorates mice survival (Chen *et al*, 2017). Moreover, patients with low tumoral *CCL2* expression survived significantly longer than those with high *CCL2* (Chen *et al*, 2017). Since pDNA-PKcs expression positively correlates with tumor progression (Lan *et al*, 2016), and in the light of our meta-analysis, it is tempting to hypothesize that in tumors where the cGAS-STING pathway fuels tumorigenesis, the use of DNA-PKcs inhibitor may facilitate tumor clearance.

Indeed, DNA-PK inhibitors have been used in preclinical studies in glioblastoma, bringing promising results (Lan *et al*, 2016, Timme *et al*, 2018), and several clinical trials are ongoing (NCT02977780 and NCT04555577). To fully exploit the benefit of DNA-PKcs inhibition, our data support that the expression of cGAS is an important parameter to consider. Conversely, DNA-PK agonists could allow the re-establishment of inflammatory responses in tumors in which the cGAS pathway is not functional, or boost anti-tumoral

Figure 6. cGAS and DNA-PKcs levels increase with tumor grade.

A Correlation plot between *PRKDC* and *MD21B1* expression in glioblastoma patients. Three distinct populations can be visualized: *PRKDC*^{low}/*MD21B1*^{low}; *PRKDC*^{high}/*MD21B1*^{low} and *PRKDC*^{high}/*MD21B1*^{high} (total patients $n = 224$).
B Violin plots present chemokine gene expression (*CXCL10*, *CCL2* and *CCL5*) in glioblastoma samples from (A).
C Violin plots present macrophage gene expression (*CD68* and *ITGAM*) in glioblastoma samples from (A).
D Violin plots present pro-inflammatory M1 macrophage gene expression (*CD86* and *CD80*) in glioblastoma samples from (A).
E Violin plots present anti-inflammatory M2 macrophages gene expression (*CD200R1* and *CD209*) in glioblastoma samples from (A).
F Violin plots present M1/M2 gene expression ratio, calculated using the mean expression of the genes indicated in (D) and (E).
G Graph presents the survival rate of glioblastoma patients from A that present *PRKDC*^{low}/*MB21D1*^{low}, *PRKDC*^{high}/*MB21D1*^{low} and *PRKDC*^{high}/*MB21D1*^{high} expression.
H Violin plots present the expression of *PRKDC* and *MB21D1* in datasets analyzed in A, based on tumor grade (II to IV).
I Representative images of immunohistochemical analysis of DNA-PKcs and cGAS proteins in human brain tumor samples. Scale bar, 75 μm.
J Schematic representation of the molecular mechanisms involved in the cooperation between DNA-PKcs and cGAS for type I IFN responses and chemokine secretion. In cells with undetectable cGAS levels, interaction with exogenous (1) or endogenous (2) cytosolic dsDNA leads to DNA-PK activation (3) and promotes IRF3-dependent type I IFN responses (4). In cells where both DNA-PK and cGAS are expressed, cytosolic DNA is detected by both DNA-PK and cGAS (5). DNA-PK induces cytokine and chemokine secretion through IRF3 activation and enables cGAS phosphorylation, thus promoting the activation of the cGAS-STING pathway. This cooperation fuels cancer-associated inflammation.

Data information: All graphs present means ± SEM. *P*-values were determined by Student's *t*-test. ns: not significant. *$P < 0.05$, **$P < 0.01$, ***$P < 0.001$, ****$P < 0.0001$. One-way Anova with Tukey's multiple comparisons test was used to compare gene expression among populations in glioblastoma dataset.
Source data are available online for this figure.

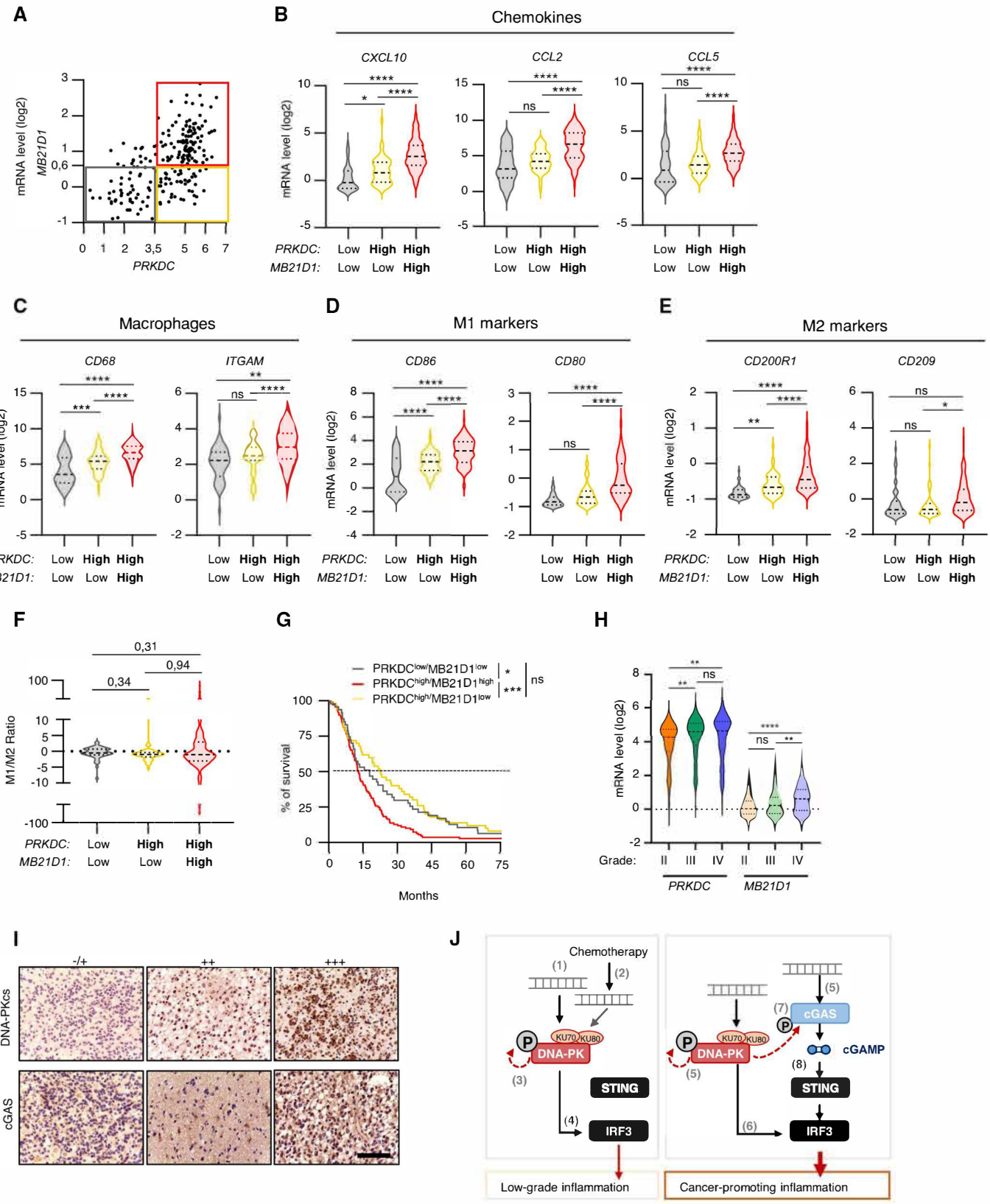

Figure 6.

Table 1. Correlation between the levels of DNA-PKcs and cGAS in surgical specimens of human brain tumors.

	DNA-PKcs expression					
		−/+	++	+++	Total	*R*/*P* value
cGAS	−/+	9 (69.2%)	6 (26.1%)	2 (22.2%)	17 (37.8%)	
	++	2 (15.4%)	13 (56.5%)	1 (11.1%)	16 (35.6%)	
	+++	2 (15.4%)	4 (17.4%)	6 (66.7%)	12 (26.6%)	$R = 0.406$
	Total	13 (100%)	23 (100%)	9 (100%)	45 (100%)	$P = 0.006$

Summary of the expression patterns of DNA-PKcs and cGAS in human glioma samples. The correlation between DNA-PKcs and cGAS protein levels was analyzed using SPSS Pearson Chi-Square test ($R = 0.406$, $P = 0.00568$). A *P*-value of < 0.05 was set as the criterion for statistical significance.

Table 2. Correlation between the levels of DNA-PKcs or cGAS and tumor grades in surgical specimens of human brain tumors.

	Tumor grades					
		I/I–II	II/II–III	III/III–IV	IV	*R*/*P* value
cGAS	−/+	6 (66.7%)	3 (18.8%)	5 (41.7%)	0 (0%)	
	++	3 (33.3%)	7 (43.8%)	5 (41.7%)	1 (25%)	
	+++	0 (0%)	6 (37.4%)	2 (16.6%)	3 (75%)	$R = 0.3211$
	Total	9 (100%)	16 (100%)	12 (100%)	4 (100%)	$P = 0.0406$
DNA-PKcs	−/+	5 (55.6%)	3 (18.8%)	6 (50%)	0 (0%)	
	++	4 (44.4%)	10 (62.5%)	1 (8.3%)	0 (0%)	
	+++	0 (0%)	3 (18.8%)	5 (41.7%)	4 (100%)	$R = 0.4335$
	Total	9 (100%)	16 (100%)	12 (100%)	4 (100%)	$P = 0.0046$

Summary of the expression patterns of DNA-PKcs and cGAS in human glioma samples. The correlation between tumor grades and DNA-PKcs or cGAS protein levels was analyzed using Pearson correlation test. A *P*-value of < 0.05 was set as the criterion for statistical significance.

inflammatory responses in those expressing cGAS. This approach may represent a promising therapeutic avenue in glioblastoma patients where STING agonists have shown benefits (preprint: Berger *et al*, 2022). Yet, the use of STING agonists has shown cell-type specific drawbacks that should not be overlooked (Gulen *et al*, 2017, Liu & Guan, 2018, Vila *et al*, 2022). Along the same line, our data support that exploring the functionality of DNA-PK and the impact of STING activation in the different cell types composing the tumor microenvironment is critical for patient stratification.

Using a transgenic zebrafish line, we revealed that the presence of cGAS in tumor cells, at early stages, is sufficient to elicit myeloid cell recruitment and polarization into M1 macrophages that are key players in the initiation of antitumor responses. However, this experimental set-up does not allow evaluation of the role played by cells of the adaptive immune system, which could contribute to shape the overall antitumor response. Yet, high levels of cGAS and STING predict poor prognosis (An *et al*, 2019), and recent reports underscore that the presence of a functional cGAS-STING axis supports tumorigenesis of chromosomally unstable cancers (Hong *et al*, 2022), which is in agreement with our glioblastoma patient data analysis. This observation, together with the fact that terminally differentiated healthy tissues do not express a functional cGAS-STING signaling axis (Dickson, 2016) and that primary tumors repress cGAS-STING activity (Bakhoum *et al*, 2018; Bakhoum & Cantley, 2018), supports that cGAS expression is acquired during tumorigenesis, to the contrary of prior assumptions that cGAS downregulation may be an immune escape mechanism.

Our study raises the possibility that in inflammatory pathologies presenting with pathological chronic STING activation, inhibition of DNA-PKcs in combination with classical Janus kinase inhibitors, which are already used in standard patient care (Sanchez *et al*, 2018), may allow better suppression of chronic type I IFN responses. Conversely, *PRKDC* mutations are associated with auto-inflammatory pathologies (Mathieu *et al*, 2015; Esenboga *et al*, 2018) in which cGAS-STING activation should be explored for the design of novel therapeutic strategies.

Materials and Methods

Reagents and Tools table

Reagent/resource	Reference or source	Identifier or catalog number
Experimental models		
Athymic Nude Mice (*M. musculus*)	Envigo	Foxn1-nu
Zebrafish	In house	tg(mfap4:RFP)

Reagents and Tools table (continued)

Reagent/resource	Reference or source	Identifier or catalog number
THP1 (*H. sapiens*)	Gift SR Paludan	RRID:CVCL_0006
HCT116 (*H. sapiens*)	Gift P. Pourquier	RRID:CVCL_B7PT
T98G (*H. sapiens*)	Gift C. Goujon	RRID:CVCL_0556
Gli4 (*H. sapiens*)	Gift J.-P. Hugnot	N/A
Gli7 (*H. sapiens*)	Gift J.-P. Hugnot	N/A
CFPAC (*H. sapiens*)	Gift N. Bonnefoy	RRID:CVCL_1119
GL261 (M.Musculus)	Gift C. Vanpouille-Box	RRID:CVCL_Y003
GSC 4, 6, 9 13, 15 (*H. sapiens*)	J.Gavard & N. Bidère	N/A
293T (*H. sapiens*)		RRID:CVCL_0063
MEF (*M. musculus*)		N/A
Recombinant DNA		
pOZ-F/HA cGAS	In house	N/A
pOZ-F/HA	In house	N/A
pOZ-F/HA cGAS-CD	In house	N/A
sfGFP-N1	Addgene	Cat #54737; RRID:Addgene_54737
LentiCRISPRv2GFP plasmid	Addgene	Cat # 82416; RRID:Addgene_82416
LentiCRISPR v2 plasmid	Addgene	Cat # 52961; RRID:Addgene_52961
pLV[CRISPR]-hCas9:T2A:Neo-U6 plasmid	VectorBuilder	
Antibodies		
pDNA-PKcs Ser2056	Abcam	Cat# ab124918, RRID:AB_11001004
pDNA-PKcs Ser2056	Abcam	Cat# ab18192, RRID:AB_869495
DNA-PKcs	Bethyl	A300-517AT
DNA-PKcs	Abcam	Cat# ab32566, RRID:AB_731981
KU70	Cell Signaling Technology	Cat# 4104, RRID:AB_1904185
KU80	Cell Signaling Technology	Cat# 2753, RRID:AB_2257526
cGAS	Cell Signaling Technology	Cat# 31659, RRID:AB_2799008
pcGAS Ser420	Abclonal	AP1228
pNF-kB p65 Ser536	Cell Signaling Technology	Cat# 3033, RRID:AB_331284
NF-kB p65	Cell Signaling Technology	Cat# 8242, RRID:AB_10859369
pSTING Ser366	Cell Signaling Technology	Cat# 19781, RRID:AB_2737062
pSTING Ser366	Cell Signaling Technology	Cat# 50907, RRID:AB_2827656
STING	Cell Signaling Technology	Cat# 13647, RRID:AB_2732796
pIRF3 Ser386	Abcam	Cat# ab76493, RRID:AB_1523836
IRF3	Cell Signaling Technology	Cat# 11904, RRID:AB_2722521
IRF3	Proteintech Europe	Cat# 11312-1-AP, RRID:AB_2127004
γH2AX	Cell Signaling Technology	Cat# 9718, RRID:AB_2118009
HSP90	Cell Signaling Technology	Cat# 4877, RRID:AB_2233307
GAPDH	Proteintech Europe	Cat# 60004-1-Ig, RRID:AB_2107436
GAPDH	Santa Cruz	Cat# sc-32233, RRID:AB_627679
αTUBULIN	Proteintech Europe	Cat# 66031-1-Ig, RRID:AB_11042766
αTUBULIN	Santa Cruz	Cat# sc-8035, RRID:AB_628408
Mouse Anti-rabbit IgG	Cell Signaling Technology	#7074; RRID:AB_2099233
Horse anti-mouse IgG	Cell Signaling Technology	#7076; RRID:AB_330924
FITC-anti-human CD38	Biolegend	Cat# 303503, RRID:AB_314355
PE-anti-human CD206	Biolegend	Cat# 321105, RRID:AB_571910

Reagents and Tools table (continued)

Reagent/resource	Reference or source	Identifier or catalog number
PE-anti-human CD209	Biolegend	Cat# 330106, RRID:AB_1134052
APC-anti-human CD86	Biolegend	Cat# 305411, RRID:AB_493232
FITC-anti-human CD14	Miltenyi Biotec	Cat# 130-110-576, RRID:AB_2655048
Oligonucleotides and other sequence-based reagents		
qPCR primers	This study	Table EV1
Guide RNA	This study	Table EV1
dsDNA probes	This study	Table EV1
Chemicals, enzymes and other reagents		
NU7441	Biotechne/Tocris	#3712
DMSO	Sigma	D2650
Puromycin	Sigma	P8833
Ethylenediamine tetraacetic acid (EDTA)	Sigma	139-33-3
Bovine Serum Albumin (BSA)	Sigma	A2153-100G
Matrigel	Corning	356234
L-glutamine	GIBCO	A2916801
FBS	Eurobio	CVFSVF00-01
Penicillin/streptomycin	GIBCO	10378016
0.25% trypsin EDTA	GIBCO	25200-056
DMEM	Lonza	BE12-614F
RPMI 1640	Lonza	LZBE12-167F
OPTIMEM	GIBCO	51985
B27	Invitrogen	0050129
N2	Invitrogen	17502048
DMEM/F12	GIBCO	11320033
EGF	Peprotech	AF-100-15
Trizol	Thermofisher	15596018
Super script IV	Thermofisher	18090050
TB Green Premix Ex Taq	TAKARA	RR420W
Rnase out	Thermofisher	10777019
dNTP mix 10mM	Thermofisher	18427013
Kit TURBO DNA-free	Thermofisher	AM1907
Protein assay dye reagent	Biorad	5000006
Jet Prime tranfection kit	Ozyme	POL114-75
GeneJuice transfection reagent	Sigma	70967-5
INTERFERin	Polyplus	POL406-50
PhosphoSTOP	Roche	4906845001
4–15% Mini-PROTEAN® TGX™ Precast Protein Gels	Bio-Rad	#4561086
NuPAGE 10 or 12% Bis-Tris Mini Protein gels	Bio-Rad	NP0302BOX ; NP0342BOX
Trans-Blot Turbo Transfer Pack 0.2 μm Nitrocellulose Midi	Biorad	1704159
SuperSignal West Pico PLUS Chemiluminescent Substrate	Thermofisher	34577
SuperSignal West Femto Maximum Sensitivity Substrate	Thermofisher	34094
Dynabeads M280	Thermofisher	11205D
2′3′-cGAMP ELISA Kit	Cayman	CAY501700
Proteome Profiler Human Chemokine Array Kit	R&D Systems	ARY017
Mammalian Protein Extraction Reagent (M-PER) buffer	Thermo Fisher	78501

Reagents and Tools table (continued)

Reagent/resource	Reference or source	Identifier or catalog number
Software		
Prism Software	GraphPad	Version 9.1
ImageJ	N/A	N/A
Image Lab	Bio-Rad Laboratories	N/A
Other		
Thermocycler	N/A	N/A
ChemiDoc Imaging System	Bio-Rad	N/A
LightCycler®	Roche Life Science	N/A
Trans-Blot® Turbo™ Transfer System	Bio-Rad	N/A

Methods and Protocols

Animals

Experiments in mice were conducted using Athymic Nude Foxn1-nu males in which subcutaneous injections were performed, prior to follow-up of tumor size over time using a caliper. These experiments were performed in agreement with European rules and regulations for animal handling (25066-2020040315236430).

In vivo experiments in zebrafish were performed using the *tg (mfap4:RFP)* zebrafish line. Each experiment was conducted using at least 21 individual fish per condition. All experimental procedures on zebrafish were performed in accordance with the European guidelines and regulations for Animal Protection and authorization no. F341725 from the French Ministry of Health.

Cells and cell cultures

THP-1^{CTRL}, THP-1$^{cGAS-/-}$ and THP-1$^{STING-/-}$ were a gift of S. R. Paludan, HCT116^{CTRL}, and HCT116$^{PRKDC-/-}$ were obtained from P. Pourquier, while parental T98G and CFPAC were provided by C. Goujon and N. Bonnefoy, respectively. Gli4 and Gli7 were a gift from J.-P. Hugnot. GL261^{CTRL} and GL261$^{cGAS-/-}$ were a gift of C. Vanpouille-Box.

293T, T98G, CFPAC and MEF and their genetically engineered derivatives were maintained in Dulbecco's modified Eagle's medium (DMEM) supplemented with 10% fetal bovine serum (FBS, Eurobio), 1% penicillin/streptomycin (Lonza), and 1% L-glutamine (Lonza).

GL261 and their genetically engineered derivatives were maintained in DMEM supplemented with 10% FBS, 1% penicillin/streptomycin, 1% L-glutamine, 50 mg/ml gentamicin, 5 mM HEPES, and 50 μM 2-mercaptoethanol. HCT116, THP-1 cells and their derivatives were cultured in RPMI media (Lonza) supplemented with 10% FBS, 1% penicillin/streptomycin, and 1% L-glutamine.

Human glioblastoma cancer stem cells Gli4 and Gli7 were cultured in T75 tissue culture flasks precoated with 40 μg/cm^2 of poly-2-hydroxyethyl methacrylate (poly-HEME, Sigma) to avoid cell adhesion. They were cultivated in DMEM/F12 1:1 (Invitrogen), N2 and B27 supplements (Invitrogen), 2 mM glutamine (Invitrogen), 0.6% glucose (Sigma), 20 μg/ml bovine insulin (Sigma) supplemented by 2 μg/ml Heparin (Sigma), 20 ng/ml EGF (Peprotech) and 10 ng/ml FGF2 (Peprotech). Patient-derived glioblastoma stem-like cells (GSC 4, 6, 9, 13, and 15) were maintained as nonadherent spheroids in serum-free medium (DMEM/F12, with N2, G5 and B27 supplements, GlutaMAX and antibiotics, Life Technologies), as described in (Harford-Wright *et al*, 2017).

Compounds

NU7441: PubChem SID 249565690.

Camptothecin: PubChem CID 24360.

Viral particle production and transduction

To generate knockout and control cell lines, lentiviral particles were produced by co-transfection of 2 × 10^6 293T cells with 5 μg of LentiCRISPRv2GFP or LentiCRISPR v2 plasmids expressing the gRNA targeting the gene of interest or non-targeting control (CTRL) gRNA, 5 μg of psPAX2 and 1 μg of pMD2.G, using the standard calcium phosphate transfection protocol. To generate the T98G cell lines stably expressing WT-cGAS, cGAS-CD, or the corresponding control cell line, retroviral particles containing the transgene encoding Flag- and HA-tagged cGAS (F/HA-cGAS) alleles were produced by co-transfecting 1 × 10^6 293T cells with 5 μg of pOZ-F/HAcGAS or pOZ-F/HAcGAS-CD or pOZ-F/HA, 2.5 μg of MLV GagPol, and 2.5 μg of A-MLV envelope.

Viral particles were harvested 48 h after transfection, filtered with 0.45 μM filters prior to transduction of 6 × 10^5 T98G cells. Medium was replaced 8 h post transduction. Selection was performed 72 h post transduction using 2 μg/ml puromycin for at least 3 days. Selected cells were amplified and the levels of the protein of interest analyzed by Western blot (WB).

Generation of knock-out cell lines

T98G$^{IRF3-/-}$ and T98G^{CTRL} cell lines were generated using the LentiCRISPRv2GFP plasmid (Addgene # 82416). T98G cells were transduced with lentiviral particles and 72 h post-transduction GFP-positive cells were sorted and pooled in a 6-well plate using a BD FACS melody. Cells were next amplified and levels of IRF3 controlled by WB.

Generation of T98G$^{STING-/-}$ and T98G^{CTRL} cell lines was conducted as above, except that the LentiCRISPR v2 plasmid (Addgene #5296) was used, and cells were selected 72 h post transduction using 2 μg/ml puromycin for 7 days. Cells were subsequently amplified and expression of STING controlled by WB. CFPAC$^{cGAS-/-}$ and CFPAC^{CTRL} cell lines were generated using a similar protocol except that puromycin-selected cells were further subjected to clonal selection using limiting dilutions. Clones were subsequently selected based on cGAS protein levels as evaluated by WB.

GL261$^{cGas-/-}$ and GL261^{CTRL} were generated using the lentiviral vector pLV[CRISPR]-hCas9:T2A:Neo-U6 plasmid containing specific guide RNA (VectorBuilder). Seventy-two hours after lentiviral transduction, cells underwent G418 selection (1 mg/ml) and were subjected to clonal selection using limiting dilutions. Resulting cGAS-deficient clones were screened by WB.

Guide RNAs for the generation of knock-out cell lines are available in Table EV1.

Generation of cell lines stably expressing cGAS

T98G overexpressing F/HA-cGAS (T98G^{cGAS}) or a catalytic dead cGAS allele (T98G$^{cGAS\text{-}CD}$), and their control cell line (T98G^{Empty}) were generated by transducing parental T98G with retroviral particles produced by using the pOZ-F/HAcGAS; pOZ-F/HAcGAS-CD construct or empty vector, respectively, and selected with 2 μg/ml puromycin for 7 days.

Generation of fluorescent glioblastoma cell line for zebrafish experiments

To obtain T98G-GFP^{Empty} and T98G-GFP^{cGAS}, T98G^{Empty}, and T98G^{cGAS} cell lines were stably transfected with sfGFP-N1 (Addgene #54737) using phosphate calcium. After transfection, cells were selected using Geneticin (800 μg/ml) for 4–6 weeks prior to zebrafish experiments.

Site directed mutagenesis

To generate the catalytic dead mutant of cGAS, site-directed mutagenesis was performed using the Quickchange Lightning kit (Agilent) following the manufacturer's instruction and primers (Fwd: 5′-ggcggttttcacgtgatagtcgctgaacttgtccaagtgt-3′; rev: 5′-acacttggacaa gttcagcgactatcacgtgaaaaccgcc-3), purchased from Eurofins Genomics.

Gene silencing

Silencing of KU70, KU80, and DNA-PKcs was achieved in T98G cells using siRNAs and INTERFERin (Polyplus) following the manufacturer's instructions.

siRNAs (Dharmacon™—Horizon Discovery) were used and sequences are available in Table EV1.

Synthetic dsDNA probes

To generate non-biotinylated or biotinylated dsDNA probes, annealing was performed as described in (Guerra *et al*, 2020), using single strand probes obtained by IDT (Stetson & Medzhitov, 2006). Probe sequences are available in Table EV1.

Whole-cell extract preparation and immunoblot

Cells were lysed in 5 packed cell volume of TENTG-150 (20 mM Tris–HCl [pH 7.4], 0.5 mM EDTA, 150 mM NaCl, 10 mM KCl, 0.5% Triton X-100, 1.5 mM $MgCl_2$, and 10% glycerol, supplemented with 10 mM β-mercaptoethanol and 0.5 mM PMSF) for 30 min at 4°C. Lysates were centrifuged 30 min at 14,000 *g*, and supernatants were collected for WB. For phosphorylated protein analysis, buffer was supplemented with PhosphoSTOP (Sigma) before whole-cell extraction. Protein quantification was performed using Bradford assay (Bio-Rad). Samples were run on either 4–15% Mini-PROTEAN® TGX™ Precast Protein Gels (Bio-Rad) (when analysis of DNA-PKcs and γH2AX was required) or on NuPAGE 10 or 12%, Bis-Tris Mini Protein gels (Invitrogen). Proteins were transferred onto nitrocellulose membranes. Membranes were incubated with primary antibodies (1:1,000 dilution except when indicated) for 2 h at RT or overnight at 4°C. Primary antibodies used include: anti-pDNA-PKcs Ser2056 (ab124918, Abcam), anti-pDNA-PKcs Ser2056 (ab18192, Abcam) for mouse cell lines, anti-DNA-PKcs (A300-517AT, Bethyl, 1:500), anti-DNA-PKcs (ab32566, Abcam) for mouse cell lines, anti-KU70 (4104S, Cell Signaling Technology), anti-KU80 (2753S, Cell Signaling Technology), anti-pcGAS Ser420 (AP1228, Abclonal), anti-cGAS (15102, Cell Signaling Technology), anti-cGAS (31659, Cell Signaling Technology) for mouse cell lines, anti-pNF-kB p65 Ser536 (3033P, Cell Signaling Technology), NF-kB p65 (8242, Cell Signaling Technology), anti-pSTING Ser366 (19781, Cell Signaling Technology), anti-pSTING Ser366 (50907, Cell Signaling Technology) for GSC cells, anti-STING (13647, Cell Signaling Technology), anti-pIRF3 Ser386 (ab76493, Abcam), anti-IRF3 (11904, Cell Signaling Technology), anti-IRF3 (11312-1-AP, Proteintech Europe) for GSC cells, anti-γH2AX (9718, Cell Signaling Technology), anti-HSP90 (4877, Cell Signaling Technology), anti-GAPDH (60004-1-Ig, Proteintech Europe, 1:5,000), anti-GAPDH (sc-32233, Santa Cruz, 1:50,000) for GSC cells, anti-αTUBULIN (66031-1-Ig, Proteintech Europe, 1:10,000), anti-αTUBULIN (sc-8035, Santa Cruz) for GSC cells. Membranes were incubated with secondary antibodies (Cell Signaling Technology) at 1:2,000 dilution, for 1 h at RT. Signal was visualized with SuperSignal West Pico Chemiluminescent Substrate (Thermo Fisher Scientific) or SuperSignal West Femto Maximum Sensitivity Substrate (Thermo Fisher Scientific), and images were acquired on a ChemiDoc (Bio-Rad) or using Amersham Hyperfilm™ ECL (GE Healthcare) films.

Biotinylated nucleic acid pull-down using cell extracts following dsDNA transfection

Interaction of endogenous proteins and transfected biotinylated nucleic acids was assessed by transfecting T98G and THP-1 cells with nucleic acids (1 μg/ml) using JetPrime, according to the manufacturer's protocol. Six hours after transfection, cells were harvested and lysed in TENTG-150 on ice for 30 min. Lysates were centrifuged at 14,000 *g* for 30 min at 4°C. Equal amounts of whole-cell lysates were incubated for 3 h at 4°C on a wheel with 30 μl Dynabeads M280 pre-blocked in (100 mM NaCl, 2 mM DTT, 20 mg/ml BSA) overnight at 4°C on a wheel. After three washes in buffer (20 mM Tris–HCl [pH 7.4], 0.5 mM EDTA, 0.05% Triton, 0.1% Tween, 150 mM NaCl, 10% glycerol, and 5 mM $MgCl_2$), bound material was eluted in 30 μl Laemmli buffer. Protein interaction with the transfected biotinylated nucleic acids was assessed by WB.

In vitro biotinylated nucleic acid pull-down

Pull-down was carried out using 30 μl of Dynabeads M280 per condition. Beads were blocked overnight as described above. After three washes in Washing Buffer (5 mM Tris–HCl [pH 7.5], 1 mM EDTA, 2 M NaCl), 3 μg of nucleic acids was coupled to 30 μl of beads according to the manufacturer's instructions before equilibration in TENTG-150. Beads were then washed once with Washing Buffer and equilibrated in TENTG-150. Whole cell extracts were diluted in TENTG-150. One milliliter of diluted lysate was added to the beads and incubated at 4°C on a wheel for 3 h in low-binding tubes (Axygen). Three consecutive washes were performed as above. Bound material was eluted in 30 μl of Laemmli buffer.

Protein interaction with the biotinylated nucleic acids was assessed by WB.

RNA extraction and RT–qPCR

RNA was extracted using TRIzol (Invitrogen) and treated with TURBO DNase (Ambion) according to manufacturer's protocols. RNA was quantified with a Nanodrop spectrophotometer (ND-1000, Nanodrop Technologies). RNA (1–2 μg) was reverse transcribed using SuperScript IV reverse transcriptase (Invitrogen). Expression of specific mRNAs was determined with a LightCycler 480 (Roche) using the SYBR green PCR master mix (Takara). Reactions were performed in duplicate or triplicate, and relative amounts of cDNA were normalized to Glyceraldehyde3-phosphate dehydrogenase (*GAPDH*) for mouse and human cells, except for GSC9 cDNA where Actin beta (ACTB) was used for normalization or eukaryotic translation elongation factor 1 alpha 1, like 1 (*ef1a*) for zebrafish analyses.

Primers used for RT–qPCR analysis are available in Table EV1.

cGAMP ELISA

For cGAMP quantification, $T98G^{Empty}$, $T98G^{cGAS}$, $THP\text{-}1^{CTRL}$, and $THP\text{-}1^{cGAS-/-}$ were seeded 18 h before dsDNA transfection. One hour before dsDNA transfection (1 μg/ml), cells were pretreated with 2 μM NU7441 (#3712, Biotechne/Tocris) in OptiMEM. Cells were harvested 6 h post transfection, counted, washed in phosphate-buffered saline (PBS) (Sigma), pelleted, and frozen at −80°C until extraction. cGAMP extraction was performed using the commercially available Mammalian Protein Extraction Reagent (M-PER) buffer (Thermo Fisher), accordingly to the manufacture protocol. The recovered supernatants were used for cGAMP measurement, following adequate sample dilution. cGAMP enzyme-linked immunosorbent assay (ELISA) was performed according to the manufacturer's protocol using the Cayman Chemical 2′3′-cGAMP ELISA Kit (CAY501700).

Cell treatment and transfection

dsDNA transfections were conducted using previously published protocols (Chamma *et al*, 2022b). In brief, cells were plated in 6-well plate, 100 mm, or 150 mm dishes 18 h before transfection. The day of transfection, media was carefully removed, plates were washed once with 1× PBS (room temperature) and 2, 10 or 20 ml Opti-MEM added, depending on the plate size. 2, 10 or 20 μg of dsDNA was transfected with the JetPrime transfection reagent (Polyplus) at 1:2 ratio. 6 h after transfection, cells were harvested and stored at −80°C prior to protein or RNA extraction.

For dsDNA transfection in GSC9 cells. the GeneJuice transfection reagent (Sigma) was used following manufacturer's protocol. To perform DNA-PKcs inhibition followed by dsDNA transfection, cells were pretreated with 2 μM of NU7441 in Opti-MEM, 1 h prior the transfection.

When transfection was performed on Gli4 or Gli7, glioblastoma spheres were dissociated in Trypsin (0.2%, Sigma) at 37°C for 4 min. Trypsin inhibitor (Sigma, 50 mg/ml), DNase I (0.015%, Roche), and $CaCl_2$ (20 mM) were subsequently added. After mechanical dissociation, cells were resuspended in PBS 1×. Following 2 washes with PBS 1×, cells were counted and 1×10^6 cells were plated per well of a 6-well plate, precoated with poly-D-lysine (25 μg/ml) and laminin (2 μg/cm^2, Sigma).

For cGAMP transfection, 10 μM of 2′3′ cGAMP were transfected for 6 h using Lipofectamine 2000 (Thermo Fischer Scientific) following the manufacturer's instructions.

For chemotherapy treatment, cells were treated with 0.16 μM camptothecin (CPT) for 48 or 72 h, or with 25 μM etoposide (ETO) for 72 h in DMEM. When the treatment was in combination with the NU7441 DNA-PKcs inhibitor, 2 μM of NU7441 was added at 24 and 48 h post CPT or ETO treatment.

Conditioned media

For conditioned media preparation, 3.5×10^6 $T98G^{Empty}$ and $T98G^{cGAS}$ cells were seeded in 150 mm dishes 18 h prior dsDNA transfection. Six hours post transfection Opti-MEM was replaced with 13.5 ml of DMEM media. Conditioned media was collected 24 h post transfection, centrifugated and filtered using 2 μm filters and frozen at −80°C.

THP-1 polarization assay

THP-1 cell lines were treated with PMA (Phorbol 12-myristate 13-acetate) at 150 nM during 24 h. Forty-eight hours later PMA-treated THP-1 were incubated with 2/3 of conditioned media complemented with 1/3 of fresh DMEM for 24 h. Cells were then harvested and samples analyzed by RT–qPCR.

Human blood-derived cells

Buffy coats from healthy donors were obtained from the Etablissement Français du Sang (EFS, Montpellier, France). Isolation and differentiation of human $CD14^+$ monocytes were performed according to previously reported protocols (Blanchet *et al*, 2010; Maarifi *et al*, 2021). Briefly, freshly isolated $CD14^+$ monocytes were incubated with indicated conditioned media for 72 h. Cells were then harvested and samples processed for flow cytometry. As control, $CD14^+$ monocytes were also incubated for 3 days in complete media prior to analysis of polarization status by flow cytometry analysis.

Flow cytometry

Cells (10^5 cells/staining) were harvested and fixed in 1% paraformaldehyde for 15 min. Cells were then washed in PBS/1% BSA buffer and incubated for 30 min on ice with the following antibodies from Biolegend (San Diego, USA): FITC-anti-human CD38 (#303503), PE-anti-human CD206 (#321105), PE-anti-human CD209 (#330106), and APC-anti-human CD86 (#305411). After washes in PBS/1% BSA buffer, cells were acquired on a Novocyte flow cytometer (Agilent Technologies). For blood-derived monocytes phenotyping, FITC-anti-human CD14 (Miltenyi, #130-110-576) antibody from Biolegend was also used.

Mouse xenograft tumor model

Athymic Nude Foxn1-nu males (Envigo) of 7 weeks were subcutaneously injected with 5×10^6 $T98G^{Empty}$ or $T98G^{cGAS}$ in the right or left flank, respectively. Cells were injected in a total volume of 100 μl in a mix of DMEM/Matrigel (v/v). Subcutaneous tumor growth was monitored over time and tumor size measured with a caliper. Tumor volume was estimated using the formula: volume = length × width^2 × 0.526.

THP-1 migration assay

24-well cell culture inserts 3.0 μm PET clear (Cell QART) were placed into the wells of a 24-well plate, containing 500 μl of

conditioned media. DMEM containing FBS was used as a negative control, while DMEM with 30 ng/ml of CCL2 as a positive control. THP-1 cells were counted, resuspended at a concentration of 3×10^5 cells/ml in RPMI without FBS and 100 µl of cell suspension added to the insert. Six hours later, the upper surface of the transwell membrane was washed twice with cold PBS and nonmigrated cells were gently scrapped with a cotton swab. Remainder cells were fixed in 100% methanol for 10 min and nuclei stained with 4′,6-diamidino-2-phenylindole (DAPI). Transwell inserts were mounted on coverslips. Apotome Z3 microscope (Zeiss) was used to visualize and count the cells that migrated through the insert.

Proteome profiler

To assess differential chemokine expression, Proteome Profiler Human Chemokine Array Kit (ARY017) was used following manufacturer's instructions. Conditioned media from $T98G^{Empty}$ and $T98G^{cGAS}$ cells were used.

Immunofluorescence and microscopy analysis

Cells were seeded on glass coverslips 18 h prior to dsDNA or CPT treatment and fixed either in methanol or with 4% PFA in 2% sucrose PBS. PFA fixation was followed by permeabilization in 0.1% Triton X-100 in PBS for 5 min at room temperature (RT). After blocking in PBS containing 0.1% Tween (PBS-T) and 5% BSA for 30 min at RT, cells were incubated overnight at 4°C with dilution in PBS-T, 5% BSA. Primary antibodies used in immunofluorescence include anti-dsDNA (ab27156, Abcam, 1:100), anti-53BP1 (MAB 3802, Sigma-Aldrich, 1:300), anti-pDNA-PKcs Ser2056 (ab18192, Abcam,1:200), and anti-DNA-PKcs (ab32566, Abcam, 1:100). Secondary antibody incubation was performed for 1 h at RT. Secondary antibodies used are Alexa Fluor 488 goat anti-Mouse IgG, (#A11001, Thermofischer) and Alexa Fluor 594-coupled goat anti-Rabbit IgG (#R37117, Thermofischer). Nuclei were stained with DAPI and coverslips mounted in Vectashield mounting media. Images were acquired by Apotome Z3 microscope by Zeiss with ZEN (blue edition) software with a 63X oil objective, and images were processed with Omero or Fiji.

Spheroids

T98G cells lines were prepared in DMEM media, and 600 cells were distributed per well of 96 well plates (Corning ultralow attachment) prior to centrifugation for 2 min at 200 g. Cells were kept in the incubator during 72 h to allow spheroid formation prior to daily scanning using a Celigo cell imaging cytometer (Nexcelom) apparatus until day 8. Volume was estimated using Celigo software.

Zebrafish experiments

The homozygous transgenic zebrafish (*Danio rerio*) line *tg(mfap4:RFP)* were maintained at 28°C at a maximum density of 50 larvae per Petri dish in fish water, containing methylene blue. After 24 h, larvae were placed in fish water, containing 200 µM 1-phenyl 2-thiourea (PTU), to prevent melanin synthesis.

Transplantation needles were prepared from borosilicate glass capillaries (outer diameter: 1 mm, inner diameter: 0.75 mm, 10 cm length, Sutter Instrument), lacking the internal filament. Using microloader tips, the transplantation needle was filled with 10 µL of cell suspension. The needle was next inserted in a needle holder, mounted on a manipulator (Narishige) and connected to the oil manual microinjector (Eppendorf CellTram vario). After anesthesia, larvae were placed in PBS containing Tricaïne, aligned and positioned dorsally between smooth forceps and 50–100 cells were transplanted in the brain region of each embryo. Transplanted larvae were next maintained at 33°C in fish water, containing PTU.

Xenotransplantation was conducted in 3 dpf embryos from the same spawn using $T98G\text{-}GFP^{Empty}$ and $T98G\text{-}GFP^{cGAS}$. Control embryos were injected with PBS. Xenotransplanted fish were used for either gene expression analysis or imaging. Briefly, for gene expression analysis, 24 h post transplantation, anesthetized embryos were manually transected with a sterile blade under a stereomicroscope to isolate the head region. Twenty-five embryo heads were then pooled in a tube (#72.693.465, Sarstedt) and frozen at −80°C prior to RNA extraction in trizol using Fastprep 24™ (MP) machine. The relative expression of M1 and M2 zebrafish macrophage markers were normalized to *ef1a*. For image acquisition embryos were placed individually in wells of a 96-well plate-adapted molds (Azelead), anesthetized using 0.16 mg/ml PBS/Tricaine (MS-222) and imaged from the day of transplantation (D0) up to D2. Z-stack Images were acquired through a Cell Discoverer 7 system (Zeiss).

Analysis of zebrafish images

To estimate tumor mass, Z-projections were performed using the Zen software (ZEISS). A threshold was then applied on the Fiji software for each embryo at D0, D1, and D2 to determine tumor area. Tumor area was next normalized to the day of transplantation (D0) to evaluate tumor growth of the injected cell lines. Macrophage recruitment around the tumor site was estimated by manual counting on Fiji, by moving the focus in all Z stacks. To characterize invasiveness, the elongated cells were counted manually on Fiji. Images were prepared for publication using the Fiji program by setting the same parameters in all compared images.

Glioblastoma RNA seq data retrieval and correlation analysis

For mRNA expression analysis, RNA seq data of CGGA-GBM data set, containing 224 glioblastoma samples was used. The data set was accessed from the GlioVis web server (http://gliovis.bioinfo.cnio.es/) and mRNA levels retrieved using the correlation tool. After plotting the mRNA level of *PRKDC* against *MB21D1*, we applied a filter cutoff to determine low and high expression allowing the definition of 4 populations: $PRKDC^{low}/MB21D1^{low}$; $PRKDC^{low}/MB21D1^{high}$; $PRKDC^{high}/MB21D1^{low}$; $PRKDC^{high}/MB21D1^{high}$. mRNA levels of genes of interest were plotted based on these populations. One-way ANOVA with Tukey's multiple comparisons test was used to compare gene expression among populations in glioblastoma dataset.

Human tumor tissue array analysis

The human nervous system glioma tissue array (NGL961) was obtained from Pantomics Inc (Fairfield, CA, USA). The study cohort comprised 41 gliomas of various grades and stages and four healthy tissues. This work was performed in accordance with the Institutional Review Board (IRB) approval at MD Anderson Cancer Center (Houston, TX, USA). The tissue array slides were incubated with primary antibodies against DNA-PKcs (1:100; Abcam, ab32566) and cGAS (1:200; Abcam, ab224144) and biotin-conjugated secondary antibodies, and then incubated with an avidin-biotin-peroxidase

complex. Visualization was performed using 3,3′-diaminobenzidine (DAB) chromogen. The tissue array cores were scored by two researchers blind to cancer outcomes. According to histologic scoring, the intensity of staining was ranked into one of three groups: high (+++, for scores 1.5 and 2), medium (++, for score 1), and low or negative (−/+, for scores 0 and 0.5). While Table 1 includes the entire cohort, Table 2 includes the analyses of the 41 gliomas tissues.

Statistical analysis

Statistical analysis was performed using GraphPad Prism version 7. For statistical analysis of *in vitro* experiments, unpaired Student's *t*-test was performed as indicated in figure legends. One-way Anova with Tukey's multiple comparisons test was used to analyze gene expression among populations in glioblastoma datasets. One-way ANOVA was used for mice studies. Mann-Whitney test was performed to analyze tumor growth and macrophage recruitment in zebrafish. The number of replicates in each experiment (including number of mice or zebrafish) are indicated in the figure legends. All data are expressed as mean ± SEM. The statistical parameters can be found in the figures and the figure legends. Ns: non-significant. $*P < 0.05$, $**P < 0.01$, $***P < 0.001$ and $****P < 0.0001$.

Data availability

This study includes no data deposited in external repositories. Glioblastoma patient data are available at http://gliovis.bioinfo.cnio.es/ (Bowman *et al*, 2017). Source data for Figs 4F and EV4B can be found on the BioImage Archive using accession number S-BIAD571.

Expanded View for this article is available online.

Acknowledgements

We thank P. Pourquier for the HCT116 cell lines, N. Bonnefoy for the parental CFPAC cell line, Soren Paludan for THP-1 cell lines, C. Vanpouille-Box for the GL261^{CTRL} and GL261$^{cGAS-/-}$ cell lines and E. Chevet for the gift of parental GL261 cells. We thank C. Goujon for the parental T98G cell line and CRISPR/Cas9 gRNA sequences. We thank C. Langevin and all members of the molecular basis of inflammation laboratory for discussions. We thank N. Dupuis and A. Blömeke-Eiben for technical assistance. We acknowledge iExplore-RAM animal facility, the MRI imaging facility, member of the national infrastructure France-BioImaging infrastructure supported by the French National Research Agency (ANR-10-INBS-04, "Investments for the future") and the SIRIC Montpellier Cancer (INCa_Inserm_DGOS_12553). Work in NL's laboratory was funded by the European Research Council (ERC-Stg CrIC: 637763, ERC-PoC DIM-CrIC: 893772), LA LIGUE pour la recherche contre le cancer, Agence Nationale de Recherche sur le SIDA et les Hépatites virales (ANRS: ECTZ117448), La Région Languedoc Roussillon, and the CNRS. CT was supported by the Merck Sharp and Dohme Avenir (MSD-Avenir—GnoSTic) program and ANRS (ECTZ119088). HC was supported by LA LIGUE pour la recherche contre le cancer. SG was supported by a LabMuse EpiGenMed. ALCV was supported by ERC-Stg CrIC: 637763, and MSD-Avenir. KP was supported by the Laboratoire d'Excellence EpiGenMed. IKV was supported by ERC-Stg CrIC: 637763, followed by Fondation pour la Recherche Médicale (FRM: ARF20170938586 "Prix Roger PROPICE pour la recherche sur le cancer du pancreas"). JM was supported by an "Agence Nationale de Recherche Technologie" (ANRT). Work in NB laboratory was funded by Fondation de France (JJ), Fondation ARC contre le Cancer (PJA to JG and NB), Institut National du Cancer (INCa PAIR-CEREB INCa_16285), Ligue nationale contre le cancer (Equipe labellisée) et comités de Loire-Atlantique, Maine et Loire, Vendée, Ille-et-Vilaine (JG, NB). CM received a fellowship from Ligue Régionale contre le Cancer and Région Pays-de-la-Loire. Work in MSS laboratory is funded by grants from National Institutes of Health (CA196740, CA258100) and Department of Defense (W81XWH-20-1-0379). Work in CVB laboratory is funded by grants from the Uncle Kory Foundation, the StacheStrong Foundation and the St. Baldrick's Foundation. MDM is supported by a 2022-SITC Nektar Therapeutics Equity and Inclusion in Cancer Immunotherapy fellowship. FPB was supported by ANRS AO1-2019-193123 and AO1-2022-192763.

Author contributions

Clara Taffoni: Conceptualization; investigation; visualization; methodology; writing – original draft; writing – review and editing. **Johanna Marines:** Investigation; visualization; methodology; writing – original draft; writing – review and editing. **Hanane Chamma:** Investigation. **Soumyabrata Guha:** Investigation. **Mathilde Saccas:** Investigation. **Amel Bouzid:** Investigation. **Ana Luiza Chaves Valadão:** Investigation; methodology. **Clément Maghe:** Investigation. **Jane Jardine:** Investigation. **Mi Kyung Park:** Investigation. **Katarzyna Polak:** Investigation; methodology. **Mara De Martino:** Investigation. **Claire Vanpouille-Box:** Supervision. **Maguy Del Rio:** Supervision. **Céline Gongora:** Supervision. **Julie Gavard:** Supervision. **Nicolas Bidere:** Supervision. **Min Sup Song:** Supervision. **Donovan Pineau:** Methodology. **Jean-Philippe Hugnot:** Supervision. **Karima Kissa:** Supervision. **Laura Fontenille:** Supervision. **Fabien P Blanchet:** Supervision; methodology. **Isabelle K Vila:** Investigation; visualization; methodology; writing – review and editing. **Nadine Laguette:** Conceptualization; supervision; visualization; methodology; writing – original draft; writing – review and editing.

Disclosure and competing interests statement

J.M. is a joint PhD student in Azelead, a startup company, and the Laguette laboratory. L.F. and K.K. are co-founders of the Azelead startup company that hosted J.M. All other authors declare that they have no competing interests.

References

Adachi N, So S, Koyama H (2004) Loss of nonhomologous end joining confers camptothecin resistance in DT40 cells. Implications for the repair of topoisomerase I-mediated DNA damage. *J Biol Chem* 279: 37343 – 37348

An X, Zhu Y, Zheng T, Wang G, Zhang M, Li J, Ji H, Li S, Yang S, Xu D *et al* (2019) An analysis of the expression and association with immune cell infiltration of the cGAS/STING pathway in pan-cancer. *Mol Ther Nucleic Acids* 14: 80 – 89

Bakhoum SF, Cantley LC (2018) The multifaceted role of chromosomal instability in cancer and its microenvironment. *Cell* 174: 1347 – 1360

Bakhoum SF, Ngo B, Laughney AM, Cavallo JA, Murphy CJ, Ly P, Shah P, Sriram RK, Watkins TBK, Taunk NK *et al* (2018) Chromosomal instability drives metastasis through a cytosolic DNA response. *Nature* 553: 467 – 472

Berger G, Knelson EH, Jimenez-Macias JL, Nowicki MO, Han S, Panagioti E, Lizotte PH, Adu-Berchie K, Stafford A, Dimitrakakis N *et al* (2022) STING activation promotes robust immune response and NK cell-mediated tumor regression in glioblastoma models. *bioRxiv* https://doi.org/10.1101/2022.02.28.481908

Blanchet FP, Moris A, Nikolic DS, Lehmann M, Cardinaud S, Stalder R, Garcia E, Dinkins C, Leuba F, Wu L *et al* (2010) Human immunodeficiency virus-1

inhibition of immunoamphisomes in dendritic cells impairs early innate and adaptive immune responses. *Immunity* 32: 654 – 669

Bowman RL, Wang Q, Carro A, Verhaak RG, Squatrito M (2017) GlioVis data portal for visualization and analysis of brain tumor expression datasets. *Neuro Oncol* 19: 139 – 141

Buonfiglioli A, Hambardzumyan D (2021) Macrophages and microglia: the cerberus of glioblastoma. *Acta Neuropathol Commun* 9: 54

Burleigh K, Maltbaek JH, Cambier S, Green R, Gale M Jr, James RC, Stetson DB (2020) Human DNA-PK activates a STING-independent DNA sensing pathway. *Sci Immunol* 5: eaba4219

Chamma H, Vila IK, Taffoni C, Turtoi A, Laguette N (2022a) Activation of STING in the pancreatic tumor microenvironment: a novel therapeutic opportunity. *Cancer Lett* 538: 215694

Chamma H, Guha S, Laguette N, Vila IK (2022b) Protocol to induce and assess cGAS-STING pathway activation *in vitro*. *STAR Protoc* 3: 101384

Chen BP, Chan DW, Kobayashi J, Burma S, Asaithamby A, Morotomi-Yano K, Botvinick E, Qin J, Chen DJ (2005) Cell cycle dependence of DNA-dependent protein kinase phosphorylation in response to DNA double strand breaks. *J Biol Chem* 280: 14709 – 14715

Chen Q, Boire A, Jin X, Valiente M, Er EE, Lopez-Soto A, Jacob L, Patwa R, Shah H, Xu K *et al* (2016) Carcinoma-astrocyte gap junctions promote brain metastasis by cGAMP transfer. *Nature* 533: 493 – 498

Chen Z, Feng X, Herting CJ, Garcia VA, Nie K, Pong WW, Rasmussen R, Dwivedi B, Seby S, Wolf SA *et al* (2017) Cellular and molecular identity of tumor-associated macrophages in glioblastoma. *Cancer Res* 77: 2266 – 2278

Corrales L, McWhirter SM, Dubensky TW Jr, Gajewski TF (2016) The host STING pathway at the interface of cancer and immunity. *J Clin Invest* 126: 2404 – 2411

Dickson I (2016) Viral hepatitis: a lack of hepatocyte STING favours HBV infection. *Nat Rev Gastroenterol Hepatol* 13: 438

Esenboga S, Akal C, Karaatmaca B, Erman B, Dogan S, Orhan D, Boztug K, Ayvaz D, Tezcan I (2018) Two siblings with PRKDC defect who presented with cutaneous granulomas and review of the literature. *Clin Immunol* 197: 1 – 5

Ferguson BJ, Mansur DS, Peters NE, Ren H, Smith GL (2012) DNA-PK is a DNA sensor for IRF-3-dependent innate immunity. *Elife* 1: e00047

Gonzalez-Suarez I, Redwood AB, Grotsky DA, Neumann MA, Cheng EH, Stewart CL, Dusso A, Gonzalo S (2011) A new pathway that regulates 53BP1 stability implicates cathepsin L and vitamin D in DNA repair. *EMBO J* 30: 3383 – 3396

Gu Y, Jin S, Gao Y, Weaver DT, Alt FW (1997) Ku70-deficient embryonic stem cells have increased ionizing radiosensitivity, defective DNA end-binding activity, and inability to support V(D)J recombination. *Proc Natl Acad Sci USA* 94: 8076 – 8081

Guerra J, Valadao AL, Vlachakis D, Polak K, Vila IK, Taffoni C, Prabakaran T, Marriott AS, Kaczmarek R, Houel A *et al* (2020) Lysyl-tRNA synthetase produces diadenosine tetraphosphate to curb STING-dependent inflammation. *Sci Adv* 6: eaax3333

Guichet PO, Bieche I, Teigell M, Serguera C, Rothhut B, Rigau V, Scamps F, Ripoll C, Vacher S, Taviaux S *et al* (2013) Cell death and neuronal differentiation of glioblastoma stem-like cells induced by neurogenic transcription factors. *Glia* 61: 225 – 239

Gulen MF, Koch U, Haag SM, Schuler F, Apetoh L, Villunger A, Radtke F, Ablasser A (2017) Signalling strength determines proapoptotic functions of STING. *Nat Commun* 8: 427

Hammarsten O, Chu G (1998) DNA-dependent protein kinase: DNA binding and activation in the absence of Ku. *Proc Natl Acad Sci USA* 95: 525 – 530

Hammel M, Yu Y, Mahaney BL, Cai B, Ye R, Phipps BM, Rambo RP, Hura GL, Pelikan M, So S *et al* (2010) Ku and DNA-dependent protein kinase dynamic conformations and assembly regulate DNA binding and the initial non-homologous end joining complex. *J Biol Chem* 285: 1414 – 1423

Harford-Wright E, Andre-Gregoire G, Jacobs KA, Treps L, Le Gonidec S, Leclair HM, Gonzalez-Diest S, Roux Q, Guillonneau F, Loussouarn D *et al* (2017) Pharmacological targeting of apelin impairs glioblastoma growth. *Brain* 140: 2939 – 2954

Hartmann G (2017) Nucleic acid immunity. *Adv Immunol* 133: 121 – 169

Hong C, Schubert M, Tijhuis AE, Requesens M, Roorda M, van den Brink A, Ruiz LA, Bakker PL, van der Sluis T, Pieters W *et al* (2022) cGAS-STING drives the IL-6-dependent survival of chromosomally instable cancers. *Nature* 607: 366 – 373

Ishikawa H, Ma Z, Barber GN (2009) STING regulates intracellular DNA-mediated, type I interferon-dependent innate immunity. *Nature* 461: 788 – 792

Lah TT, Novak M, Breznik B (2020) Brain malignancies: glioblastoma and brain metastases. *Semin Cancer Biol* 60: 262 – 273

Lan T, Zhao Z, Qu Y, Zhang M, Wang H, Zhang Z, Zhou W, Fan X, Yu C, Zhan Q *et al* (2016) Targeting hyperactivated DNA-PKcs by KU0060648 inhibits glioma progression and enhances temozolomide therapy via suppression of AKT signaling. *Oncotarget* 7: 55555 – 55571

Larkin B, Ilyukha V, Sorokin M, Buzdin A, Vannier E, Poltorak A (2017) Cutting edge: activation of STING in T cells induces type I IFN responses and cell death. *J Immunol* 199: 397 – 402

Li M, Shu HB (2020) Dephosphorylation of cGAS by PPP6C impairs its substrate binding activity and innate antiviral response. *Protein Cell* 11: 584 – 599

Liu S, Guan W (2018) STING signaling promotes apoptosis, necrosis, and cell death: an overview and update. *Mediators Inflamm* 2018: 1202797

Maarifi G, Lagisquet J, Hertel Q, Bonaventure B, Chamontin C, Fuchs K, Moncorge O, Tauziet M, Mombled M, Papin L *et al* (2021) Alarmin S100A9 restricts retroviral infection by limiting reverse transcription in human dendritic cells. *EMBO J* 40: e106540

Mathieu AL, Verronese E, Rice GI, Fouyssac F, Bertrand Y, Picard C, Chansel M, Walter JE, Notarangelo LD, Butte MJ *et al* (2015) PRKDC mutations associated with immunodeficiency, granuloma, and autoimmune regulator-dependent autoimmunity. *J Allergy Clin Immunol* 135: e5

Mayca Pozo F, Geng X, Tamagno I, Jackson MW, Heimsath EG, Hammer JA, Cheney RE, Zhang Y (2021) MYO10 drives genomic instability and inflammation in cancer. *Sci Adv* 7: eabg6908

Morchikh M, Cribier A, Raffel R, Amraoui S, Cau J, Severac D, Dubois E, Schwartz O, Bennasser Y, Benkirane M (2017) HEXIM1 and NEAT1 long non-coding RNA form a multi-subunit complex that regulates DNA-mediated innate immune response. *Mol Cell* 67: e5

Nussenzweig A, Chen C, da Costa SV, Sanchez M, Sokol K, Nussenzweig MC, Li GC (1996) Requirement for Ku80 in growth and immunoglobulin V(D)J recombination. *Nature* 382: 551 – 555

Sanchez GAM, Reinhardt A, Ramsey S, Wittkowski H, Hashkes PJ, Berkun Y, Schalm S, Murias S, Dare JA, Brown D *et al* (2018) JAK1/2 inhibition with baricitinib in the treatment of autoinflammatory interferonopathies. *J Clin Invest* 128: 3041 – 3052

Sen T, Rodriguez BL, Chen L, Corte CMD, Morikawa N, Fujimoto J, Cristea S, Nguyen T, Diao L, Li L *et al* (2019) Targeting DNA damage response promotes antitumor immunity through STING-mediated T-cell activation in small cell lung cancer. *Cancer Discov* 9: 646 – 661

Sivick KE, Desbien AL, Glickman LH, Reiner GL, Corrales L, Surh NH, Hudson TE, Vu UT, Francica BJ, Banda T *et al* (2018) Magnitude of therapeutic

STING activation determines CD8(+) T cell-mediated anti-tumor immunity. *Cell Rep* 25: e5

Song S, Peng P, Tang Z, Zhao J, Wu W, Li H, Shao M, Li L, Yang C, Duan F *et al* (2017) Decreased expression of STING predicts poor prognosis in patients with gastric cancer. *Sci Rep* 7: 39858

Stetson DB, Medzhitov R (2006) Recognition of cytosolic DNA activates an IRF3-dependent innate immune response. *Immunity* 24: 93 – 103

Sui H, Zhou M, Imamichi H, Jiao X, Sherman BT, Lane HC, Imamichi T (2017) STING is an essential mediator of the Ku70-mediated production of IFN-lambda1 in response to exogenous DNA. *Sci Signal* 10: eaah5054

Sun L, Wu J, Du F, Chen X, Chen ZJ (2013) Cyclic GMP-AMP synthase is a cytosolic DNA sensor that activates the type I interferon pathway. *Science* 339: 786 – 791

Sun X, Liu T, Zhao J, Xia H, Xie J, Guo Y, Zhong L, Li M, Yang Q, Peng C *et al* (2020) DNA-PK deficiency potentiates cGAS-mediated antiviral innate immunity. *Nat Commun* 11: 6182

Taffoni C, Steer A, Marines J, Chamma H, Vila IK, Laguette N (2021) Nucleic acid immunity and DNA damage response: new friends and old foes. *Front Immunol* 12: 660560

Tanaka Y, Chen ZJ (2012) STING specifies IRF3 phosphorylation by TBK1 in the cytosolic DNA signaling pathway. *Sci Signal* 5: ra20

Tao X, Song J, Song Y, Zhang Y, Yang J, Zhang P, Zhang D, Chen D, Sun Q (2022) Ku proteins promote DNA binding and condensation of cyclic GMP-AMP synthase. *Cell Rep* 40: 111310

Timme CR, Rath BH, O'Neill JW, Camphausen K, Tofilon PJ (2018) The DNA-PK inhibitor VX-984 enhances the Radiosensitivity of glioblastoma cells grown *in vitro* and as Orthotopic xenografts. *Mol Cancer Ther* 17: 1207 – 1216

Tu Y, Ji C, Yang B, Yang Z, Gu H, Lu CC, Wang R, Su ZL, Chen B, Sun WL *et al* (2013) DNA-dependent protein kinase catalytic subunit (DNA-PKcs)-SIN1 association mediates ultraviolet B (UVB)-induced Akt Ser-473 phosphorylation and skin cell survival. *Mol Cancer* 12: 172

Vila IK, Chamma H, Steer A, Saccas M, Taffoni C, Turtoi E, Reinert LS, Hussain S, Marines J, Jin L *et al* (2022) STING orchestrates the crosstalk between polyunsaturated fatty acid metabolism and inflammatory responses. *Cell Metab* 34: e8

Wang Y, Su GH, Zhang F, Chu JX, Wang YS (2015) Cyclic GMP-AMP synthase is required for cell proliferation and inflammatory responses in rheumatoid arthritis Synoviocytes. *Mediators Inflamm* 2015: 192329

Wang F, Zhao M, Chang B, Zhou Y, Wu X, Ma M, Liu S, Cao Y, Zheng M, Dang Y *et al* (2022) Cytoplasmic PARP1 links the genome instability to the inhibition of antiviral immunity through PARylating cGAS. *Mol Cell* 82: e7

Wei J, Chen P, Gupta P, Ott M, Zamler D, Kassab C, Bhat KP, Curran MA, de Groot JF, Heimberger AB (2020) Immune biology of glioma-associated macrophages and microglia: functional and therapeutic implications. *Neuro Oncol* 22: 180 – 194

West RB, Yaneva M, Lieber MR (1998) Productive and nonproductive complexes of Ku and DNA-dependent protein kinase at DNA termini. *Mol Cell Biol* 18: 5908 – 5920

Xia T, Konno H, Ahn J, Barber GN (2016) Deregulation of STING signaling in colorectal carcinoma constrains DNA damage responses and correlates with tumorigenesis. *Cell Rep* 14: 282 – 297

Yang H, Wang H, Ren J, Chen Q, Chen ZJ (2017) cGAS is essential for cellular senescence. *Proc Natl Acad Sci USA* 114: E4612 – E4620

Yue X, Bai C, Xie D, Ma T, Zhou PK (2020) DNA-PKcs: a multi-faceted player in DNA damage response. *Front Genet* 11: 607428

Zhang X, Brann TW, Zhou M, Yang J, Oguariri RM, Lidie KB, Imamichi H, Huang DW, Lempicki RA, Baseler MW *et al* (2011) Cutting edge: Ku70 is a novel cytosolic DNA sensor that induces type III rather than type I IFN. *J Immunol* 186: 4541 – 4545

Zhou W, Whiteley AT, de Oliveira Mann CC, Morehouse BR, Nowak RP, Fischer ES, Gray NS, Mekalanos JJ, Kranzusch PJ (2018) Structure of the human cGAS-DNA complex reveals enhanced control of immune surveillance. *Cell* 174: 300 – 311.e11

Zhu Y, An X, Zhang X, Qiao Y, Zheng T, Li X (2019) STING: a master regulator in the cancer-immunity cycle. *Mol Cancer* 18: 152

The FEBS Journal

FEBS PRESS science publishing by scientists

Plakophilin 1 deficiency in prostatic tumours is correlated with immune cell recruitment and controls the up-regulation of cytokine expression post-transcriptionally

Martin Kim[1,2], Sonja Reidenbach[1], Tanja Schlechter[3], Ann Christin Rothmann[1], Rainer Will[4] and Ilse Hofmann[1,3,5]

1 Division of Vascular Oncology and Metastasis, German Cancer Research Center, DKFZ-ZMBH Alliance, Heidelberg, Germany
2 Department of Urology and Pediatric Urology, University Hospital Erlangen, Friedrich-Alexander-University Erlangen-Nürnberg (FAU), Erlangen, Germany
3 GPCF Unit Antibodies, German Cancer Research Center, Heidelberg, Germany
4 GPCF Unit Cellular Tools, German Cancer Research Center, Heidelberg, Germany
5 Department of Vascular Biology and Tumor Angiogenesis, European Center for Angioscience (ECAS), Medical Faculty Mannheim, Heidelberg University, Heidelberg, Germany

Keywords
cytokine mRNA stability; immune cell recruitment; plakophilin 1; prostate cancer; tumour environment

Correspondence
I. Hofmann, Division of Vascular Oncology and Metastasis, German Cancer Research Center, DKFZ-ZMBH Alliance, Im Neuenheimer Feld 280, 69120 Heidelberg, Germany
Tel: +49 (0) 6221 42 3351
E-mail: i.hofmann@dkfz.de

(Received 10 December 2021, revised 11 October 2022, accepted 1 November 2022)

doi:10.1111/febs.16680

Plakophilin (PKP1) 1 is a member of the arm-repeat family of catenins and acts as a structural component of desmosomes, which are important stabilizers of cell–cell adhesion. Besides this, PKP1 also occurs in a non-junctional, cytoplasmic form contributing to post-transcriptional regulation of gene expression. Moreover, PKP1 is expressed in the prostate epithelium but its expression is frequently downregulated in prostate cancers with a more aggressive phenotype. This observation may imply a tumour-suppressive role of PKP1. We found that, in prostatic adenocarcinomas with PKP1 deficiency, the occurrence of T-cells, B-cells, macrophages and neutrophils were significantly increased. In a PKP1-deficient prostatic cancer cell line expressing IL8, these levels were statistically meaningfully reduced upon PKP1 re-expression. When analysing prostatic PKP1 knockdown cell lines, the mRNA and protein levels of additional cytokines, namely CXCL1 and IL6, were upregulated. The effect was rescued upon re-expression of a *PKP1* RNAi-resistant form. The corresponding mRNAs were co-precipitated with cytoplasmic PKP1, indicating that they are components of PKP1-containing mRNA ribonucleoprotein particles. Moreover, the mRNA half-lives of *CXCL1*, *IL8* and *IL6* were significantly increased in PKP1-deficient cells, showing that these mRNAs were stabilized by PKP1. In an *in vitro* migration assay, the higher cytokine concentrations led to higher migration rates of THP1 and PBMC cells. This finding implies that PKP1 loss of expression *in vivo* correlates with the recruitment of immune cells into the tumour area to set up a tumour-specific environment. One may speculate that this newly established tumour environment has tumour-suppressive characteristics and thereby accelerates tumour progression and metastasis.

Introduction

Plakophilin 1 (PKP1) belongs to the PKP protein family comprising three different members PKP1, 2 and 3 that are specifically recruited to desmosomal plaques in a highly cell-type-specific manner where they

Abbreviations
CXCL1, growth-regulated alpha protein/C-X-C motif chemokine 1; IL6, interleukin 6; IL8, interleukin 8; PBMC, peripheral mononuclear cells; PKP1, plakophilin; TLS, tertiary lymphoid organ.

support desmosome assembly and stability [1,2]. Additionally, PKPs act as crucial regulators of specific signalling programmes and control diverse cellular processes that range from transcription, mRNA abundance, protein synthesis, growth, proliferation and migration to invasion and tumour development [3,4]. Besides a localization in cell–cell contacts such as desmosomes, PKP1 is found both in the cytoplasm and the nucleus and can bind to single-stranded DNA [5,6]. Moreover, PKP1 and/or PKP3 have also been detected as part of mRNA ribonuclein complexes, cytoplasmic stress granules and ribosomal complexes implying modulatory roles in mRNA localization, stability and translation [7]. In fact, PKP1 and PKP3 affect the mRNA stability of desmosomal proteins [8] and PKP1 may serve as a regulator of mRNA translation by promoting eIF4A1 activity [9].

Prostate cancer is one of the most frequent malignancies in men in the Western world [10]. In recent years, the therapy of prostate cancer has been improved, but there is still a strong demand for accurate diagnosis and improved treatment options to decrease mortality. Prostate tumour initiation and progression are a multistep process where prostatic epithelial cells gain new biological capabilities [11]. These changes in cellular behaviour are due to altered gene expression that may be regulated directly by epigenetic alterations, transcription factors or by RNA-binding proteins influencing RNA metabolism and translation [12]. Interestingly, PKP1 expression in prostate cancer is largely reduced in more aggressive cancer types and associated with lymph node metastasis [13,14]. For PKP1, methylation-mediated epigenetic alterations lead to loss of expression [15–17]. Hence, PKP1 may have a tumour-suppressive function and PKP1 loss of function may be a critical event during prostate cancer progression.

Over the past years, the tumour-associated stroma comprising different cells that are recruited to the area of solid tumours constitute altogether the tumour environment that has gained strong interest regarding tumour progression and metastasis [11]. Immune cells of the innate and adaptive response such as macrophages, neutrophils or T-cells and B-cells infiltrate the tumour area and thereby may inhibit or, on the contrary, promote tumour progression [18,19]. The dynamic crosstalk between these diverse cell types, through direct cell–cell contact or soluble factors, such as cytokines, creates a specific niche. Cytokines such as CXCL1, IL6 and IL8 comprise a family of low-molecular-weight proteins involved in host defence, inflammation and tumour immunobiology [20,21]. They may directly have an impact on tumorigenesis by regulating tumour cell growth, invasiveness and metastasis, or act indirectly by exerting modulatory effects on various cells of the tumour microenvironment [22]. Moreover, T-cells and B-cells may also accumulate in organized cellular aggregates, so-called tertiary lymphoid structures (TLS), that develop in non-lymphoid tissues at sites of chronic inflammation including tumours [23,24] and drive the immune response against tumour development and progression [25].

In the present study, we observed that in prostatic adenocarcinomas cell counts for T-cells, B-cells, macrophages and neutrophils were increased in PKP1-deficient areas implying a correlation between PKP1 loss of expression and recruitment of immune cells. In *in vitro* experiments with a PKP1-deficient prostatic cancer cell line, IL8 expression was influenced by PKP1. Moreover, in PKP1 knockdown cell lines, the mRNA and protein level of CXCL1, IL6 and IL8 were increased. The mRNAs of these cytokines were part of PKP1-containing complexes and their mRNA stability was influenced by PKP1. The higher cytokine concentrations in cultures of PKP1-deficient cell lines led to higher migration rates of THP1 and PBMC *in vitro*.

Results

Immune cells are recruited to PKP1-deficient tumour areas in prostatic adenocarcinoma

In earlier studies, we noticed that in prostatic adenocarcinoma showing a dedifferentiated state, such as in a high Gleason pattern, PKP1 expression was partially lost [13]. To find out if PKP1 loss correlates with immune cell recruitment *in vivo*, we re-analysed tissue samples with known heterogeneity in PKP1 expression. Serial sections of such tissue samples together with corresponding tumour-free samples from the same patient were stained with PKP1- and keratin 8/18-specific antibodies (Fig. 1). Here, keratin 8/18 staining, an epithelial marker, indicated tumour areas negative for PKP1. These serial sections were counterstained with markers for T-cells (CD3), B-cells (CD19), neutrophils (myeloperoxidase) or macrophages (CD163) (Fig. 2). As a control, all markers were used in parallel on samples with diagnosed prostatitis to verify the specific reaction of the individual antibodies meant as markers for T-cells, B-cells, neutrophils and macrophages.

After a careful inspection in three similar-sized, rectangular areas in prostatic adenocarcinomas, single cells were counted in PKP1-positive or -negative tumour areas as well as in corresponding tumour-free areas. For all four cell types, we noticed an increase in cell

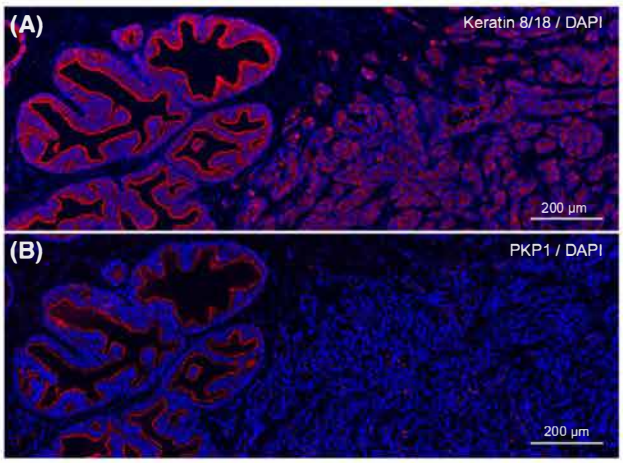

Fig. 1. Immunolocalization of PKP1 (A) and K8/K18 (B) on formaldehyde-fixed, paraffin-embedded tissue of prostatic adenocarcinoma. Serial sections from 13 different prostatic adenocarcinoma were incubated with PKP1- or K8/K18-specific antibodies. Representative images are shown. The bar represents 200 µm. Note, loss of PKP1 expression in tumour areas with high Gleason pattern.

counts in PKP1-deficient tumour areas compared not only to PKP1-positive tumour areas but also to tumour-free areas. We also carefully counted the number of TLS found in tumour-free as well as in PKP1-positive and PKP1-negative tumour regions by using CD3 staining and accumulation of T-cells as a marker for TLS (Fig. 3A,B). In some areas, individual TLS were partially located in a PKP1-deficient and PKP1-positive area. As here, no unambiguous assignment was possible and therefore a new category named border was opened (Fig. 3C). Although the total count of TLS in PKP1-negative tumour areas was higher compared to PKP1-positive ones, the statistical analysis with the Dunnett procedure indicated no significant enrichment of TLS in PKP1-negative tumour areas. Taken together, single immune cells such as T-cells, B-cells, neutrophils and macrophages were recruited to PKP1-negative tumour areas, however, TLS were not accumulating in these tumour areas.

PKP1 influences IL8 expression in a prostatic cancer cell line

Recently, it was reported that IL8 as detected by RNA *in situ* hybridization (RISH) was expressed in prostate adenocarcinomas and was associated with prostate cancer aggressiveness [26]. Moreover, with this method, the expression of IL8 in tumour cells *in vivo* and *in vitro* was validated. To find out if PKP1 may influence IL8 expression, we compared IL8 expression in the prostatic cancer cell lines LNCaP and DU145 (Fig. 4A). Although both cell lines are PKP1 deficient only, DU145 cells showed a high IL8 level. A *PKP1*-cDNA construct comprising aa235-726 [6] was re-expressed in DU145 cells. The truncated PKP1 form has lost desmosomal targeting capacity and is shown to accumulate in the cytoplasm. The effect on the IL8 level was compared to DU145 control cells (Fig. 4B). Noteworthy, the IL8 level was significantly reduced suggesting that PKP1 influenced the IL8 level.

Cytokine expression is deregulated in PKP1 knockdown cells

To understand how PKP1 loss might contribute to immune cell recruitment in prostatic adenocarcinoma, we decided to use the prostatic cell line BPH1 that expressed PKP1 (Fig. 4A) and established different PKP1 knockdown cell lines and characterized the expression profile [27]. When we grouped the altered genes into categories immunological disease, inflammatory disease and inflammatory response were identified with highly significant values above the threshold. We had a closer look into the deregulated genes and noticed that components known to be involved in immunological responses, the cytokines *CXCL1*, *IL8* and *IL6* were upregulated with fold changes 3.97, 3.85 and 2.55 respectively. To verify the expression profiling data, qPCR analysis using *CXCL1*-, *IL8*- and *IL6*-specific primers was performed. Indeed, in two different PKP1-deficient cell lines, BPH1-shPKP1-2411 and BPH1-shPKP1-2357 cells, the relative mRNA level for *CXCL1*, *IL6* and *IL8* was significantly increased (Fig. 5A). Moreover, we quantified the protein concentration of CXCL1, IL6 and IL8 and noticed that

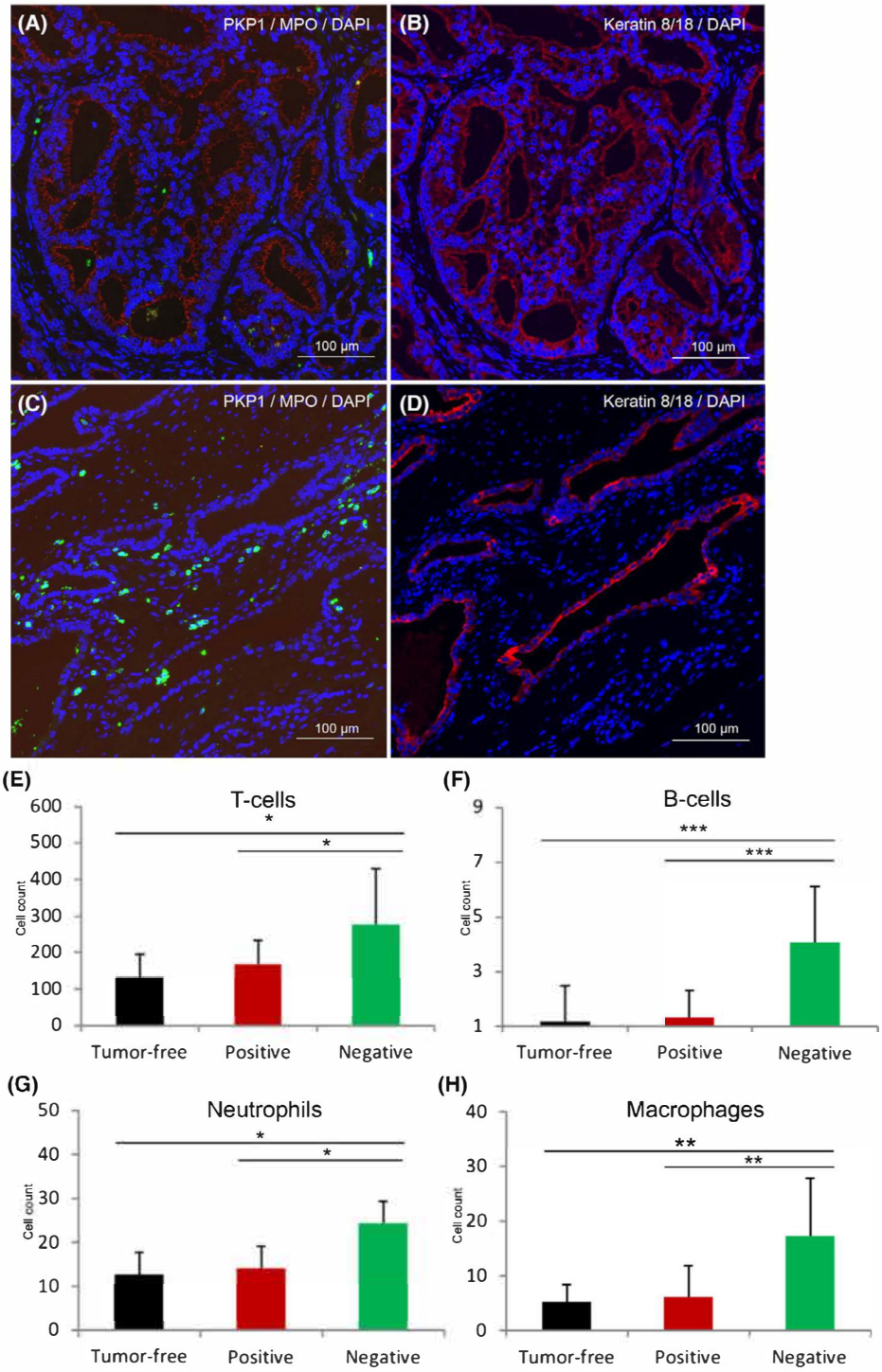

Fig. 2. Immune cells are enriched in PKP1-deficient prostatic tumour areas. (A–D) Serial sections of prostatic adenocarcinoma from 12 different prostatic adenocarcinoma were incubated with PKP1 and myeloperoxidase (MPO) (A, C) or K8/K18-specific antibodies (B, D). Bar represents 100 µm. Representative images are shown. (E–H) The occurrence of single T-cells (anti-CD3 staining) (E), single B-cells (anti-CD19 staining) (F), neutrophils (anti-myeloperoxidase staining) (G) or macrophages (anti-CD163 staining) (H) was counted in tumour-free prostatic tissue samples and compared to PKP1-positive or -negative areas in the corresponding prostatic adenocarcinoma with 11 samples in (E, F) and 12 samples in (G, H). A tumour-free section from the same patient was analysed from 11 tumour samples. Error bars show SD. Statistical comparisons between experimental groups were analysed using one-way analysis of variance (ANOVA) with pairwise *post hoc* comparison according to the Holm–Sidak. $*P < 0.05$; $**P < 0.01$, $***P < 0.001$.

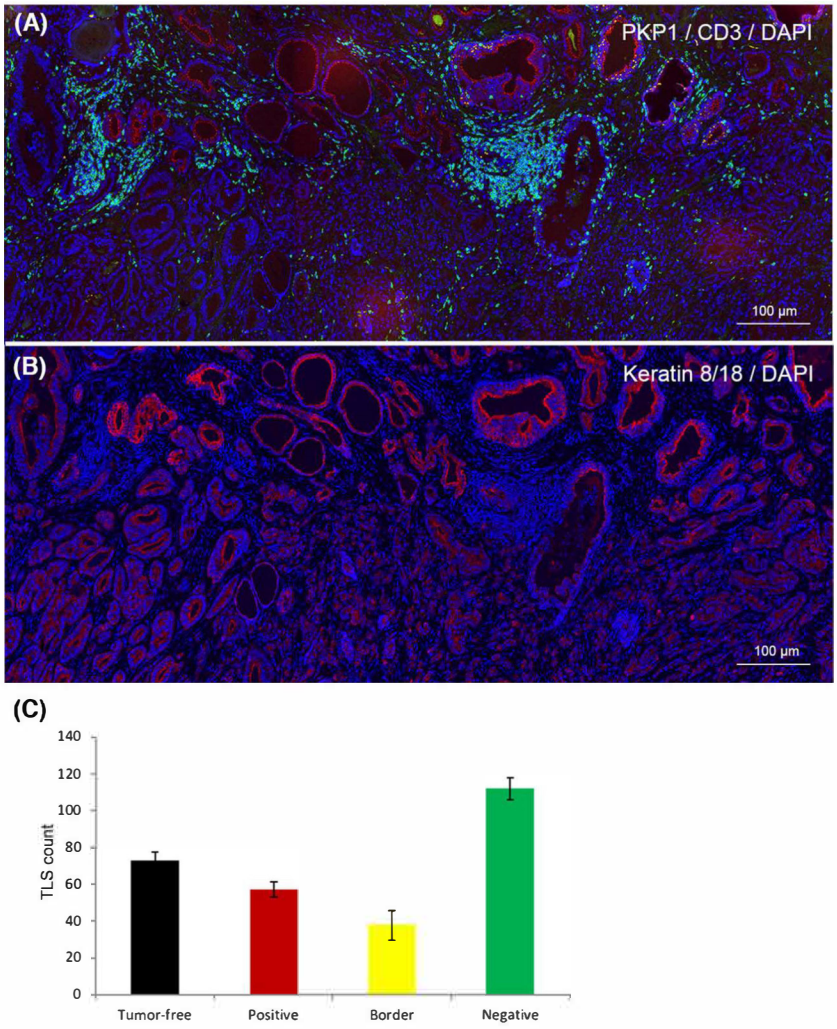

Fig. 3. Tertiary lymphatic organs are not accumulating in PKP1-deficient prostatic tumour areas. Serial sections of prostatic adenocarcinoma, 13 in total, were incubated with PKP1 and CD3 (A) or K8/K18 (B) specific antibodies. Representative images are shown. The bar represents 100 µm. (C) The total number of tertiary lymphatic organs (TLS) in tumour-free prostatic tissue samples was counted and compared to PKP1-positive or -negative areas in the corresponding prostatic adenocarcinoma. In parallel, for 12 tumour samples, the corresponding tumour-free section from the same patient was analysed. Areas that covered both (border) were counted separately. Representative images are shown. Error bars show SD.

protein levels were also significantly increased in the two different PKP1-decificient cell lines (Fig. 5B). To rule out off-target effects, we performed a rescue experiment. A *PKP1*-cDNA construct comprising aa235-726 [6] containing no shRNA targeting sites was re-expressed in the knockdown cell line BPH1-shPKP1-2357 (Fig. 5C). Upon stable PKP1 re-expression of a cytoplasmic PKP1 form, the relative CXCL1 level was significantly reduced. Taken together, the knockdown of PKP1 led to higher expression of *CXL1*, *IL6* and *IL8* mRNAs. Importantly, higher expression levels of CXCL1, IL6 and IL8 were also observed at the protein level, indicating that PKP1 is physiologically important for the regulation of the expression of the cytokines CXCL1, IL6 and IL8.

Cytokine mRNA levels are regulated by PKP1

We have shown that the non-junctional, cytoplasmic form of PKP1 is part of ribonuclein complexes [7,8]. These complexes also contain mRNA and regulate mRNA stability of desmosomal mRNAs [8,14]. To verify if *CXCL1*, *IL6* and *IL8* mRNA are also part of PKP1 complexes, we immunoprecipitated PKP1 from BPH1 cell lysates and tested for the presence of these specific mRNAs by RT-PCR. Indeed, *CXCL1*, *IL6* and

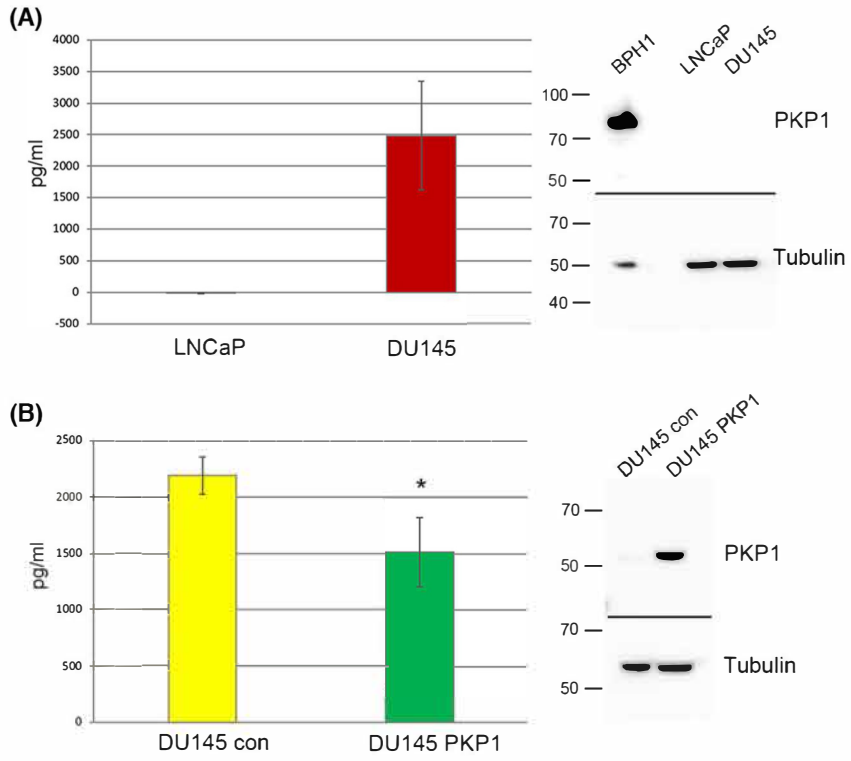

Fig. 4. Comparison of IL8 expression in different prostatic adenocarcinoma cell lines with different PKP1 levels. The protein level of IL8 was measured in LNCaP and DU145 cell lines in three biological replicates (A). Note, both cell lines do not express PKP1 in contrast to BPH1 cells. (B) Upon expression of *PKP1*-cDNA-containing aa235-726 in DU145 cells (DU145 PKP1), the IL8 concentration was reduced compared to DU145 cells (DU145 con). The detection of tubulin is provided as a loading control. The molecular mass marker in kDa is indicated on the left. The error bar shows SD. In (B), four biological replicates were statistically compared using one-way analysis of variance (ANOVA) with pairwise *post hoc* comparison according to the Holm–Sidak procedure. $*P < 0.05$.

IL8 mRNA were detected in PKP1 immunoprecipitate but not the control snoRNA *ACA44* (Fig. 6A).

Given that the PKP1 knockdown leads to increased mRNA levels of *CXCL1*, *IL6* and *IL8*, we investigated the influence of PKP1 on the mRNA stability of *CXCL1*, *IL6* and *IL8*. Transcription was blocked with actinomycin D, and RNA was isolated after 0, 15, 30 or 60 min. The amount of *CXCL1*, *IL6* or *IL8* mRNA over time was then measured by quantitative RT-PCR. The half-lives of the specific mRNAs were estimated and compared between the control and PKP1 knockdown cell line (Fig. 6B). Indeed, for all three transcripts, the half-lives were significantly increased in the PKP1 knockdown cell line indicating that PKP1 regulates the mRNA stability of *CXCL1*, *IL6* and *IL8*.

PKP1 depletion increased the ability of immune cells to migrate *in vitro*

To test if the higher chemokine levels in PKP1-deficient cells affected the cell migration of immune cells, we applied a transwell cell migration assay. Conditioned medium from the two different PKP1-deficient cell lines, BPH1-shPKP1-2411 and BPH1-shPKP1-2357 cells, and the control cell line was placed in the bottom chamber. THP1 cells or PBMC were filled in the top chambers of the wells and the number of cells that migrated through the transwell filter into the bottom chamber was counted. Indeed, the chemokines produced by PKP1-deficient cell lines induced the cell migration of THP1 cells and PBMC (Fig. 7A,B). These data support that PKP1 regulates the cell migration of immune cells *in vitro*.

Discussion

In PKP1-deficient areas of prostatic adenocarcinomas, cell counts for T-cells, B-cells, macrophages and neutrophils were increased implying a correlation between PKP1 loss of expression and recruitment of immune cells. *In vitro*, in a PKP1-deficient prostate cancer cell line, the expression of the chemokine IL8 was

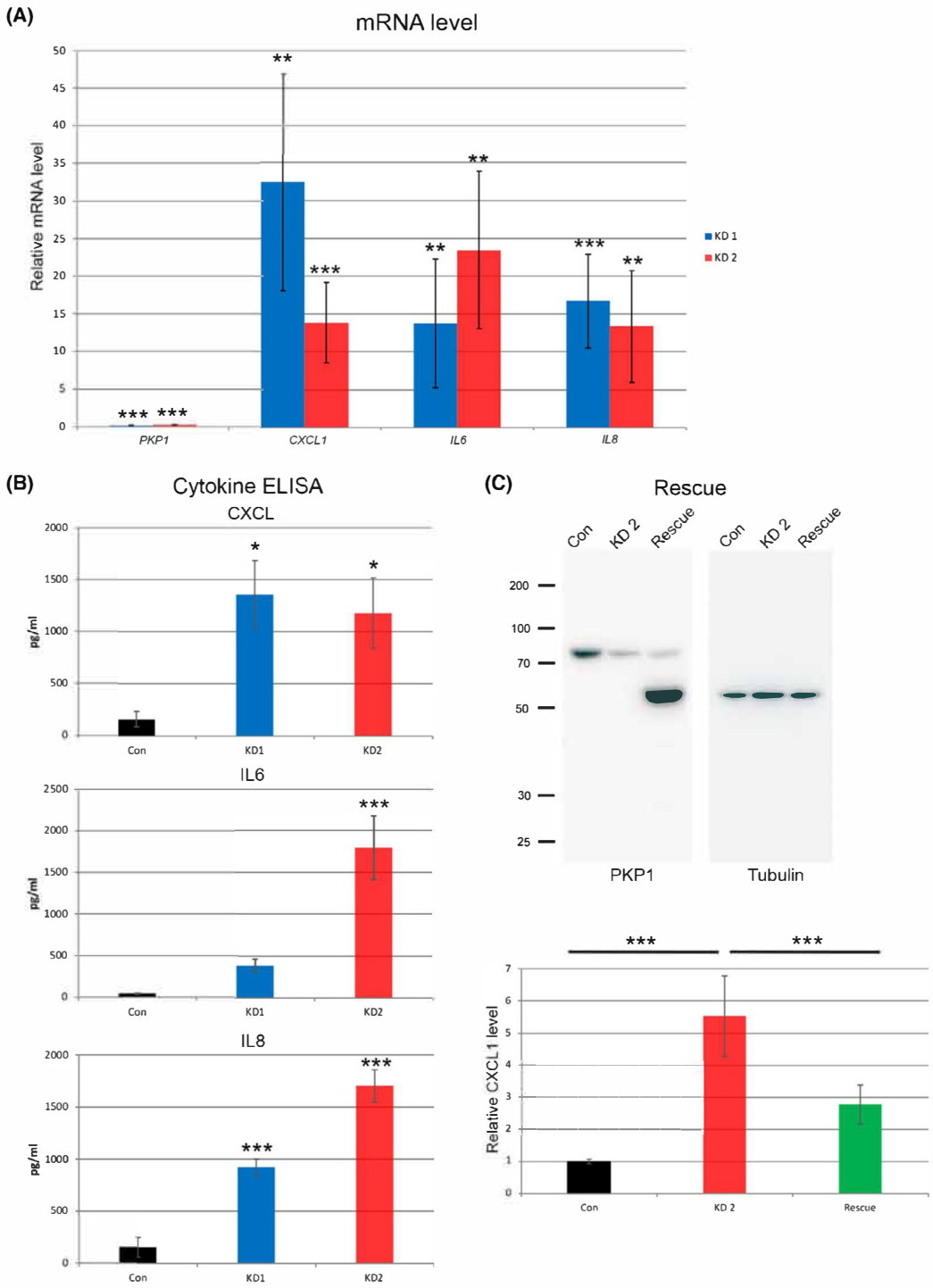

Fig. 5. Comparison of RNA and protein levels of CXCL1, IL6 and IL8 in cells with different PKP1 levels. (A) Relative mRNA expression levels of *CXCL1*, *IL6* and *IL8* (A) and protein levels of CXCL1, IL6 and IL8 (B) were measured in BPH1-shPKP1-2411 (KD1) and BPH1-shPKP1-2357 (KD2) showing a stable PKP1 knockdown and BPH1-shLac (con) cells. (C) Upon expression of a RNAi-resistant *PKP1*-cDNA containing aa235-726 in BPH1-shPKP1-2357 (KD2) cells, the relative CXCL1 concentration was reduced. The detection of tubulin is provided as a loading control. The molecular mass marker in kDa is indicated on the left. Error bars show SD. In (A), statistical comparisons between the two experimental groups of seven biological replicates were analysed using the unpaired Student's *t*-test. In (B), 3 and in (C), 5 biological replicates were statistically compared by one-way analysis of variance (ANOVA) with pairwise *post hoc* comparison according to the Holm–Sidak procedure. $*P < 0.05$; $**P < 0.01$; $***P < 0.001$.

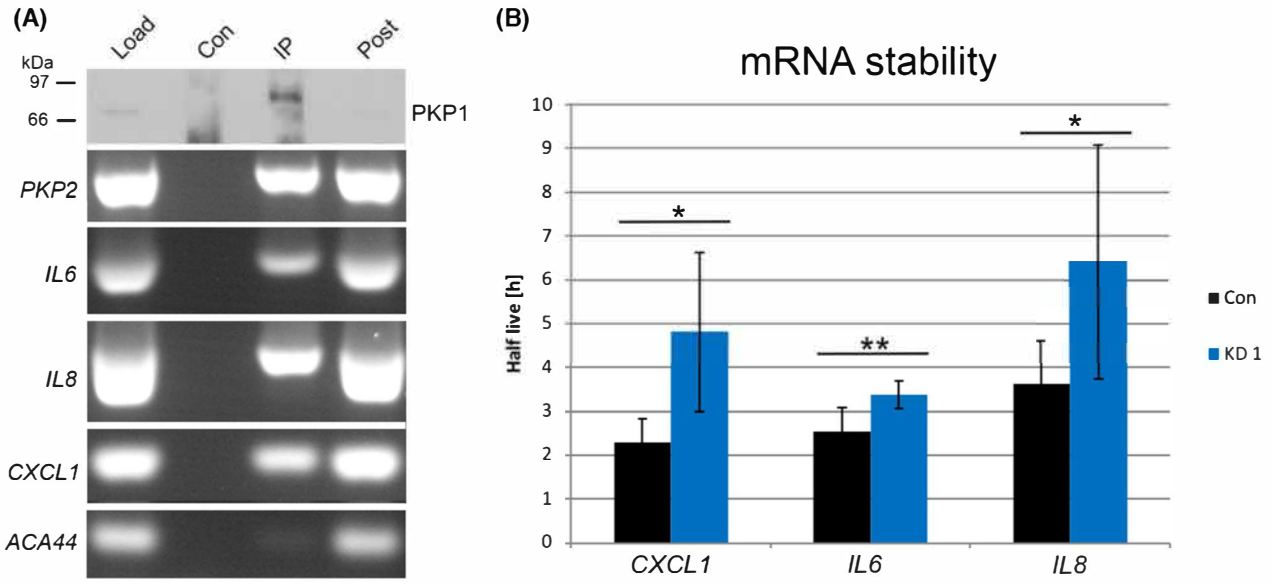

Fig. 6. *CXCL1*, *IL6* and *IL8* mRNAs are part of PKP1 complexes (A) and the mRNA stability of *CXCL1*, *IL6* and *IL8* are increased in PKP1-deficient cells (B). (A) By immunoprecipitation using lysates from BPH1 wild-type cells with PKP1-specific antibodies PKP1 was enriched, compared to control (con) and immunoprecipitated (IP). In corresponding samples, the occurrence of specific mRNAs was determined after RNA isolation by RT-PCR. Note that *IL6*, *IL8*, *CXCL1* and *PKP2* but not *ACA44* mRNA could be detected in total lysates (Load, Post) and the PKP1 immunoprecipitate (IP). (B) mRNA stability measurements for *CXCL1*, *IL6* and *IL8* were performed in BPH1-shPKP1-2357 (KD2) and negative control BPH1-shLac (con) after actinomycin D treatment. RNA was isolated after 0, 15, 30 and 60 min and the amount of specific mRNA was detected by quantitative RT-PCR. The data of seven independent biological replicates were normalized to 0 h time point and the mRNA half-live was determined. Error bars show SD. Statistical comparisons between the two experimental groups were analysed using the unpaired Student's *t*-test. $*P < 0.05$; $**P < 0.01$. Note that the differences in mRNA half-lives are significant for *CXCL1*, *IL6* and *IL8* mRNA.

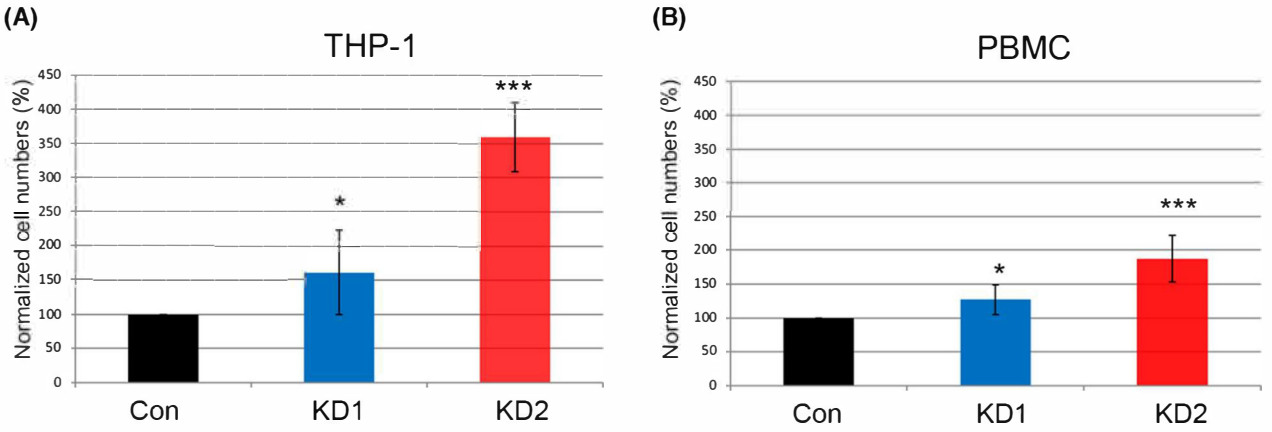

Fig. 7. PKP1-deficient cells show an increased migration of THP-1 cells (A) and PBMC (B). Conditioned cell culture media obtained from the cell lines BPH1-shPKP1-2411 (KD1) and BPH1-shPKP1-2357 (KD2) showing a stable PKP1 knockdown, and from the control cell line BPH1-shLac (con) were analysed in a transwell cell migration assay regarding their ability to induce the migration of THP1 cells or PBMC. The data of five independent biological replicates were normalized to the control. Error bars show SD. In (A), 5 and in (B), 7 biological replicates were statistically compared using one-way analysis of variance (ANOVA) with pairwise *post hoc* comparison according to the Holm–Sidak procedure. $*P < 0.05$; $***P < 0.001$. Note, for medium from PKP1 knockdown cells with increased concentrations of CXCL1, IL6 and IL8, an increased migration of THP-1 cells and PBMC was observed.

regulated by PKP1. Moreover, in PKP1 knockdown cell lines, the mRNA and protein level of CXCL1, IL6 and IL8 were increased. The mRNAs of these cytokines were part of PKP1-containing complexes and their mRNA stability was influenced by PKP1. The higher cytokine concentrations in cultures of PKP1-deficient cell lines led to higher migration rates of THP1 and PBMC *in vitro*.

Our finding that in PKP1-deficient prostatic tumour areas significantly higher counts of B-cells, T-cells, neutrophils and macrophages were observed is in line with numerous studies exploring evidence regarding immune infiltration as a potential mediator and indicator of aggressive prostate cancer, reviewed by Strasner and Karin [18]. From these studies, using mostly cell biological methods such as immunohistochemistry, it is suggested that growing tumours can induce the recruitment of immune cells into the prostate microenvironment and initiate a reciprocal interaction that promotes disease progression. Here, especially tumour-infiltrating T-cells and macrophages were found to be pro-tumorigenic.

However, all these studies, including this one, are impaired by the complexity of infiltrating immune cells. A newly developed bioinformatic approach using the CIBERSORT program allows differentiating among 22 tumour-infiltrating immune cells [28]. By using this method, it was shown that five different immune cell types accumulated in prostate cancer tissue. In accordance with our data, these were B-cells, M1/M2 macrophages and neutrophils. Interestingly, a higher infiltration of M1 macrophages and neutrophils significantly reduced the survival of prostate cancer patients [29]. It has to be mentioned that depending on the data sets analysed other results may be obtained with this method [30–32]. Moreover, this bioinformatic analysis does not consider the occurrence of tertiary lymphoid organs that consist of T-cells, B-cells and other cells and their specific function in tumour progression [23].

Increased numbers of immune cells are also found in both acute and chronic prostatic inflammation [33]. Chronic inflammation has been designated as an enabling characteristic of cancer development [11] and has an impact at each stage of tumour development – from tumour initiation and promotion to progression and metastasis [34]. Therefore, it would be interesting to analyse if PKP1 deficiency is also occurring in inflammation-associated regions of prostate atrophy (PIA) or prostatic intraepithelial neoplasia (PIN).

Intra-tumoral cytokine expression of, for example IL6 or IL8 has been already reported [26,35] and this expression is proposed as a key regulator of infiltrating immune cell recruitment. It is well documented that cytokines such as IL6 or IL8 may be secreted by prostate epithelial cancer cells and thereby may promote prostate cancer growth [20,26,35,36]. Indeed, we were able to verify IL8 expression in a prostate cancer cell line and noticed that IL8 expression decreased upon re-expression of PKP1, suggesting that PKP1 is involved in regulating its expression. The expression of cytokines is regulated on the one hand by transcription factors such as androgen receptor (AR) or erythroblast transformation-specific-related gene (ERG) [26,35]. Especially, AR plays a central role in prostate cancer initiation and progression, and therefore androgen ablation therapy is in clinical use for several decades [37–39]. Here, we, however, were able to show that PKP1 is part of an mRNA ribonucleoprotein particle that contains the mRNAs of *CXCL1*, *IL8* or *IL6*. This observation is in line with earlier findings on the occurrence of PKP1/3 mRNPs in cytoplasmic extracts [7]. Moreover, in this study, we present evidence that PKP1 deficiency stabilizes the mRNAs of *CXCL1*, *IL8* and *IL6*. An effect of PKP1 on mRNA half-lives has been already reported, although here the mRNAs of desmosomal proteins were destabilized [8]. One may assume that additional factors in these PKP1-containing mRNPs may trigger the destabilization or stabilization of specific mRNAs. Indeed, the regulation of cytokine expression is an excellent example of the complex network of cis-acting sequence elements and trans-acting factors controlling mRNA stability [40]. Some trans-acting factors (e.g. TTP or HuR) may bind to the same sequence elements (e.g. AU-rich elements), compete for binding and once bound may have opposite effects on mRNA stability [41]. In addition, mRNAs with AU-rich elements are prone to accumulate in the so-called P-bodies, storage sites for translationally repressed mRNAs and inactive mRNA decay enzymes [42,43]. PKP1 loss may lead to a cytokine mRNA release from these sites of long-term storage and the mRNAs are now ready to be translated leading to the accumulation of the protein [44].

Besides analysing the occurrence of specific immune cells in the prostatic tumour environment, it is also important to search if there is an immune cell-specific correlation with the expression of certain proteins. It has been shown that PTEN deficiency in prostate cancer is associated with an immunosuppressive tumour environment [45]. Likewise, it is intriguing to assume that PKP1 loss is also linked to an immunosuppressive state in prostate cancer, and determining PKP1 status may help to indicate which patients might benefit from immunotherapies.

Materials and methods

Patients and tissue samples

In total, 27 formaldehyde-fixed, paraffin-embedded sections were applied in this study [13]. Thirteen of 27 contained prostatic adenocarcinoma, 12 were tumour free and in two samples prostatitis was diagnosed. For 11 tumour samples, the corresponding tumour-free section from the same patient was used. The mean age was 64.8 years and ranged from 60 to 68 years. Gleason scores in prostatic adenocarcinoma were above 7 and for all samples, a heterogenous PKP1 expression was reported [13]. Tissue samples were provided by the tissue bank of the National Center for Tumour Diseases (NCT, Heidelberg, Germany) in accordance with the regulations of the tissue bank and the approval of the ethics committee of Heidelberg University. The regulations follow the standards set by the Declaration of Helsinki and include a written patients' consent on the use of tissue samples for research purposes.

Antibodies

The antibodies used for western blotting and immunohistochemistry were as follows: anti-PKP1 guinea pig (GP-PP1; Progen Biotechnik, Heidelberg, Germany), anti-PKP1 mouse (clone PP1-5C2; Progen Biotechnik), anti-K8/18 guinea pig (K8/18; Progen Biotechnik), anti-α-tubulin (mouse monoclonal clone DM1A, CP06, Sigma Aldrich, Merck, Darmstadt, Germany), anti-CD19 (rabbit monoclonal clone SP110, SAB 5500047; Sigma Aldrich, Steinheim, Germany), anti-CD3 (rabbit monoclonal clone SP7, RM 9107; Thermo Fisher Scientific, Karlsruhe, Germany), anti-CD163 (mouse monoclonal clone 10D6, MA5-11458; Thermo Fisher Scientific), anti-myeloperoxidase, specific for human (rabbit serum, A0398; Dako, Hamburg, Germany) and secondary antibodies conjugated with horseradish peroxidase (115-035-044 or 106-035-003; Jackson ImmunoReserach, West Grove, PA, USA) for immunoblot and Cy3 (706-165-148 or 715-165-150; Jackson ImmunoReserach) or Alexa Fluor 488 (715-545-151 or 711-545-152; Thermo Fisher Scientific) for immunohistochemistry.

Cell lines and isolation of PBMCs

Cancer cell lines used (LNCaP and DU145) were described earlier [13] and further information on the two cell lines may also be found in the catalogue of the American Tissue Culture Collection (ATCC, Manassas, VA, USA). DU145 cells were transduced with the pLenti plasmid 6.2/V5-dest PKP1-cDNA construct containing aa235-726 [6] or an empty vector as control according to the transduction protocol of the manufacturer, and cells were selected with 10 $\mu g \cdot mL^{-1}$ blasticidin (Invitrogen, Thermo Fisher Scientific, Karlsruhe, Germany). The cell lines BPH1-shPKP1-2411 (KD1) and BPH1-shPKP1-2357 (KD2) show a stable PKP1 knockdown, and the control cell line BPH1-shLac (con) and BPH1 cells have been already described [27]. For a rescue experiment, an RNAi-resistant *PKP1*-cDNA construct containing aa235-726 [6] including a C-terminal myc-tag [13] was expressed in the BPH1-shPKP1-2357 (KD2) cell line using the pLenti plasmid 6.2/V5-dest according to the transduction protocol of the manufacturer and cells were selected with 10 $\mu g \cdot mL^{-1}$ blasticidin (Invitrogen, Thermo Fisher Scientific) and single-cell clones obtained by limited dilution [13]. THP-1 cells [46] were cultivated in RPMI-1640 medium. All cell lines were authenticated by multiplex cell line authentication and regularly tested for mycoplasma contamination [47,48]. Peripheral mononuclear blood cells (PBMC) were isolated from human whole blood by density gradient centrifugation with Lympho-Paque solution (Genaxxon Bioscience, Ulm, Germany) using Leucosep tubes (Greiner Bio-One, Frickenhausen, Germany). Separated blood cells were sedimented and suspended in ACK lysing buffer (Gibco, Life Technology Cooperation, Grand Island, NY, USA) to remove red blood cells. PBMC were then kept in RPMI-1640 medium until use.

Transwell cell migration assay

Conditioned medium from epithelial cell lines was placed in 24-well culture dishes, and transwell filter inserts (Greiner Bio-One) were inserted [49]. Here, filters with 8 µm pore size for THP-1 cells and filters with 3 µm pore size for PBMC were used. A total of 100 000 cells in the cell culture medium were filled into the upper reservoir and incubated for 3 h in a cell incubator. Then, the inserts were removed, and the plate and cells that had moved into the lower reservoir were collected and counted in a Neubauer chamber.

RNA isolation and quantitative, real-time PCR

RNA isolation and quantitative, real-time PCR was performed as described [50]. Specific primers applied in this study were as follows: *PKP1* (for) 5′-GACCAGGACA ACTCCACGTT-3′ and (rev) 5′-CTGCTGGTGGTCCCAT AGTT-3 5; *CXCL1* (for) 5′-CTTGCCTCAATCCTGC ATCC-3′ and (rev) 5′-GGTCAGTTGGATTTGTCACTG T-3′; *IL6* (for) 5′- AGAGGCACTGGCAGAAAACA-3′ and (rev) 5′- TCACCAGGCAAGTCTCCTCA; *IL8* (for) 5′-CCAAACCTTTCCACCCCAAAT-3′ and (rev) 5′-GCC CTCTTCAAAAACTTCTCCA-3′; *GAPDH* (for) 5′-ATGT TCGTCATGGGTGTGAA-3′ and (rev) 5′-GTCTTCTGG GTGGCAGTGAT-3′ and *EEF1A1* (for) 5′-TTGTCGTC ATTGGACACGTAG-3′ and (rev) 5′-CACGTTCACGCT CAGCTTTC-3′. Values were normalized to the geometric mean of the relative expression levels of the internal references *GAPDH* and *EEF1A1*. All procedures were performed according to the manufacturer's protocol and performed in technical and biological triplicate.

Immunofluorescence and counting of immune cells

Serial sections of formalin-fixed, paraffin-embedded tissue sections were first deparaffinized, and antigen retrieval was performed as described previously in a steamer with 0.1 M Tris–HCl buffer containing 5% urea, pH 9.0 [13]. Sections were then treated with 0.2% Triton X-100 in PBS, and blocked with 2% milk powder and 5% donkey serum in PBS. For double localization markers for immune cells were incubated with either PKP1- or Keratin 8/18-specific polyvalent sera. An incubation step with DAPI (1 $\mu g \cdot mL^{-1}$, #18860, Serva for Electrophoresis, Heidelberg, Germany) was included to stain nuclei. To reduce unspecific background, an incubation step in Vector True View (SP8400; Biozol Diagnostics, Eching, Germany) was included. The specimens were then inspected at a fluorescence microscope (Axioscan, Zeiss, Oberkochen, Germany), and images were taken. For quantification, three random PKP1-positive and -negative areas (1.69 mm^2) were identified in prostatic adenocarcinoma and the number of single T-cells, B-cells, neutrophils and macrophages were manually counted. In parallel, in tumour-free samples, three similar-sized squares of these cells were also counted. For counting TLS, the whole image was inspected and the counted TLS were categorized in PKP1 positive, negative or being at the border of both.

Cytokine ELISA

To measure the concentration of CXCL1, IL6 and IL8 in the supernatant of cultured cell lines, the following kits were used: Human CXCL1 (GRO alpha) Human SimpleStep ELISA Kit (ab190805), Human IL-6 (interleukin-6) SimpleStep ELISA Kit (ab178013) and Human IL-8 (interleukin-8) SimpleStep ELISA Kit (ab214030). All procedures were performed according to the manufacturer's protocol and performed in technical and biological triplicate (Abcam, Cambridge, UK).

RNA stability assay

For mRNA stability measurements, the cells were treated with 5 $\mu g \cdot mL^{-1}$ actinomycin D (Serva Electrophoresis) and incubated for 15 min, 30 min or 1 h in an incubator at 37 °C. RNA isolation and quantitative, real-time PCR were performed as described above. mRNA half-lives were calculated assuming a first-order decay rate. Curves were fitted by linear regression, and mRNA half-lives were calculated as follows: $t_{1/2} = \ln(2)/k$ [8].

Immunoprecipitation of proteins and protein-associated RNA

For immunoprecipitation analysis, magnetic beads conjugated with secondary protein A beads (both DYNAL Magnetic Beads, Invitrogen) were used. Immunoprecipitation of proteins (IP) has been described in detail [8,51]. Incubation of lysates with beads only was used as a negative control for unspecific binding. RNA was isolated with Trizol (Ambion, Life Technologies, Darmstadt, Germany), transcribed into cDNA (High Capacity cDNA kit; Applied Biosystems) and then further used for RT-PCR. Specific primers were used as mentioned above for quantitative, real-time PCR, and primers for controls have been described in [51] [8].

Gel electrophoresis and western blot

Tissues lysates were generated and analysed by western blot as previously described [13]. Light emission was recorded by a photomultiplier in a gel documentation system (Amersham Imager 680, Cytiva, Marlborough, MA, USA).

Statistical analysis

Values are representative of at least three independent biological experiments including technical replicates. Data are shown as mean ± SD. Statistical comparisons between experimental groups were analysed using unpaired Student's *t*-test or one-way analysis of variance (ANOVA) with pairwise *post hoc* comparison according to the Holm–Sidak procedure; a *P*-value < 0.05 was considered to be significant ($*P < 0.05$; $**P < 0.01$; $***P < 0.001$). The analysis was performed with SIGMAPLOT 13 (Systat Software GmbH, Erkrath, Germany).

Acknowledgements

This study was funded by grants from the German Cancer Aid (109248) and the 'Deutsche Forschungsgemeinschaft' (HO 2455/3-1). The present work was done in fulfillment of the requirements for obtaining the degree "Dr. med." Open Access funding enabled and organized by Projekt DEAL.

Conflict of interest

The authors declare no conflict of interest.

Author contributions

IH designed the study; MK, SR, TS, ACR and RW performed the experiments; MK, SR, TS, ACR and IH analysed and interpreted the data; and MK and IH wrote the manuscript. All authors read and approved the submitted manuscript.

Peer review

The peer review history for this article is available at https://publons.com/publon/10.1111/febs.16680.

Data availability statement

The data that support the findings of this study are available from the corresponding author (i.hofmann@dkfz.de) upon reasonable request.

References

1 Schmidt A, Jager S. Plakophilins–hard work in the desmosome, recreation in the nucleus? *Eur J Cell Biol*. 2005;**84**:189–204.
2 Nekrasova O, Green KJ. Desmosome assembly and dynamics. *Trends Cell Biol*. 2013;**23**:537–46.
3 Hofmann I. Plakophilins and their roles in diseased states. *Cell Tissue Res*. 2020;**379**:5–12.
4 Broussard JA, Getsios S, Green KJ. Desmosome regulation and signaling in disease. *Cell Tissue Res*. 2015;**360**:501–12.
5 Schmidt A, Langbein L, Rode M, Pratzel S, Zimbelmann R, Franke WW. Plakophilins 1a and 1b: widespread nuclear proteins recruited in specific epithelial cells as desmosomal plaque components. *Cell Tissue Res*. 1997;**290**:481–99.
6 Sobolik-Delmaire T, Reddy R, Pashaj A, Roberts BJ, Wahl JK 3rd. Plakophilin-1 localizes to the nucleus and interacts with single-stranded DNA. *J Invest Dermatol*. 2010;**130**:2638–46.
7 Hofmann I, Casella M, Schnolzer M, Schlechter T, Spring H, Franke WW. Identification of the junctional plaque protein plakophilin 3 in cytoplasmic particles containing RNA-binding proteins and the recruitment of plakophilins 1 and 3 to stress granules. *Mol Biol Cell*. 2006;**17**:1388–98.
8 Fischer-Keso R, Breuninger S, Hofmann S, Henn M, Rohrig T, Strobel P, et al. Plakophilins 1 and 3 bind to FXR1 and thereby influence the mRNA stability of desmosomal proteins. *Mol Cell Biol*. 2014;**34**:4244–56.
9 Wolf A, Krause-Gruszczynska M, Birkenmeier O, Ostareck-Lederer A, Huttelmaier S, Hatzfeld M. Plakophilin 1 stimulates translation by promoting eIF4A1 activity. *J Cell Biol*. 2010;**188**:463–71.
10 Taitt HE. Global trends and prostate cancer: a review of incidence, detection, and mortality as influenced by race, ethnicity, and geographic location. *Am J Mens Health*. 2018;**12**:1807–23.
11 Hanahan D, Weinberg RA. Hallmarks of cancer: the next generation. *Cell*. 2011;**144**:646–74.
12 Buccitelli C, Selbach M. mRNAs, proteins and the emerging principles of gene expression control. *Nat Rev Genet*. 2020;**21**:630–44.
13 Breuninger S, Reidenbach S, Sauer CG, Strobel P, Pfitzenmaier J, Trojan L, et al. Desmosomal plakophilins in the prostate and prostatic adenocarcinomas: implications for diagnosis and tumor progression. *Am J Pathol*. 2010;**176**:2509–19.
14 Yang C, Strobel P, Marx A, Hofmann I. Plakophilin-associated RNA-binding proteins in prostate cancer and their implications in tumor progression and metastasis. *Virchows Arch*. 2013;**463**:379–90.
15 Zhang W, Flemington EK, Deng HW, Zhang K. Epigenetically silenced candidate tumor suppressor genes in prostate cancer: identified by modeling methylation stratification and applied to progression prediction. *Cancer Epidemiol Biomarkers Prev*. 2019;**28**:198–207.
16 Kaz AM, Luo Y, Dzieciatkowski S, Chak A, Willis JE, Upton MP, et al. Aberrantly methylated PKP1 in the progression of Barrett's esophagus to esophageal adenocarcinoma. *Genes Chromosomes Cancer*. 2012;**51**:384–93.
17 Haase D, Cui T, Yang L, Ma Y, Liu H, Theis B, et al. Plakophilin 1 is methylated and has a tumor suppressive activity in human lung cancer. *Exp Mol Pathol*. 2019;**108**:73–9.
18 Strasner A, Karin M. Immune infiltration and prostate cancer. *Front Oncol*. 2015;**5**:128.
19 Hsu BE, Shen Y, Siegel PM. Neutrophils: orchestrators of the malignant phenotype. *Front Immunol*. 2020;**11**:1778.
20 Nguyen DP, Li J, Tewari AK. Inflammation and prostate cancer: the role of interleukin 6 (IL-6). *BJU Int*. 2014;**113**:986–92.
21 Waugh DJ, Wilson C. The interleukin-8 pathway in cancer. *Clin Cancer Res*. 2008;**14**:6735–41.
22 Adekoya TO, Richardson RM. Cytokines and chemokines as mediators of prostate cancer metastasis. *Int J Mol Sci*. 2020;**21**:4449.
23 Sautès-Fridman C, Petitprez F, Calderaro J, Fridman WH. Tertiary lymphoid structures in the era of cancer immunotherapy. *Nat Rev Cancer*. 2019;**19**:307–25.
24 Gago da Graça C, van Baarsen LGM, Mebius RE. Tertiary lymphoid structures: diversity in their development, composition, and role. *J Immunol*. 2021;**206**:273–81.
25 N J, J T, Sl N, Gt B. Tertiary lymphoid structures and B lymphocytes in cancer prognosis and response to immunotherapies. *Onco Targets Ther*. 2021;**10**:1900508.
26 Maynard JP, Ertunc O, Kulac I, Baena-Del Valle JA, De Marzo AM, Sfanos KS. IL8 expression is associated with prostate cancer aggressiveness and androgen receptor loss in primary and metastatic prostate cancer. *Mol Cancer Res*. 2020;**18**:153–65.
27 Yang C, Fischer-Keso R, Schlechter T, Strobel P, Marx A, Hofmann I. Plakophilin 1-deficient cells upregulate SPOCK1: implications for prostate cancer progression. *Tumour Biol*. 2015;**36**:9567–77.
28 Newman AM, Liu CL, Green MR, Gentles AJ, Feng W, Xu Y, et al. Robust enumeration of cell subsets

from tissue expression profiles. *Nat Methods*. 2015;**12**:453–7.
29 Wu Z, Chen H, Luo W, Zhang H, Li G, Zeng F, et al. The landscape of immune cells infiltrating in prostate cancer. *Front Oncol*. 2020;**10**:517637.
30 Zhang E, Dai F, Mao Y, He W, Liu F, Ma W, et al. Differences of the immune cell landscape between normal and tumor tissue in human prostate. *Clin Transl Oncol*. 2020;**22**:344–50.
31 Zhu S, Han X, Qiao X, Chen S. The immune landscape and prognostic immune key genes potentially involved in modulating synaptic functions in prostate cancer. *Front Oncol*. 2020;**10**:1330.
32 Meng J, Liu Y, Guan S, Fan S, Zhou J, Zhang M, et al. The establishment of immune infiltration based novel recurrence predicting nomogram in prostate cancer. *Cancer Med*. 2019;**8**:5202–13.
33 Sfanos KS, Yegnasubramanian S, Nelson WG, De Marzo AM. The inflammatory microenvironment and microbiome in prostate cancer development. *Nat Rev Urol*. 2018;**15**:11–24.
34 Hibino S, Kawazoe T, Kasahara H, Itoh S, Ishimoto T, Sakata-Yanagimoto M, et al. Inflammation-induced tumorigenesis and metastasis. *Int J Mol Sci*. 2021;**22**:5421.
35 Merz C, von Mässenhausen A, Queisser A, Vogel W, Andrén O, Kirfel J, et al. IL-6 overexpression in ERG-positive prostate cancer is mediated by prostaglandin receptor EP2. *Am J Pathol*. 2016;**186**:974–84.
36 Baron VT, Pio R, Jia Z, Mercola D. Early growth response 3 regulates genes of inflammation and directly activates IL6 and IL8 expression in prostate cancer. *Br J Cancer*. 2015;**112**:755–64.
37 Tang Q, Cheng B, Dai R, Wang R. The role of androgen receptor in cross talk between stromal cells and prostate cancer epithelial cells. *Front Cell Dev Biol*. 2021;**9**:729498.
38 Labbé DP, Brown M. Transcriptional regulation in prostate cancer. *Cold Spring Harb Perspect Med*. 2018;**8**:a030437.
39 Aurilio G, Cimadamore A, Mazzucchelli R, Lopez-Beltran A, Verri E, Scarpelli M, et al. Androgen receptor signaling pathway in prostate cancer: from genetics to clinical applications. *Cell*. 2020;**9**:2653.
40 Kovarik P, Ebner F, Sedlyarov V. Posttranscriptional regulation of cytokine expression. *Cytokine*. 2017;**89**:21–6.
41 Wang H, Ding N, Guo J, Xia J, Ruan Y. Dysregulation of TTP and HuR plays an important role in cancers. *Tumour Biol*. 2016;**37**:14451–61.
42 Luo Y, Na Z, Slavoff SA. P-bodies: composition, properties, and functions. *Biochemistry*. 2018;**57**:2424–31.
43 Courel M, Clément Y, Bossevain C, Foretek D, Vidal Cruchez O, Yi Z, et al. GC content shapes mRNA storage and decay in human cells. *Elife*. 2019;**8**:e49708.
44 Zhang B, Herman PK. It is all about the process(ing): P-body granules and the regulation of signal transduction. *Curr Genet*. 2020;**66**:73–7.
45 Vidotto T, Saggioro FP, Jamaspishvili T, Chesca DL, Picanço de Albuquerque CG, Reis RB, et al. PTEN-deficient prostate cancer is associated with an immunosuppressive tumor microenvironment mediated by increased expression of IDO1 and infiltrating FoxP3^{+} T regulatory cells. *Prostate*. 2019;**79**:969–79.
46 Bosshart H, Heinzelmann M. THP-1 cells as a model for human monocytes. *Ann Transl Med*. 2016;**4**:438.
47 Castro F, Dirks WG, Fähnrich S, Hotz-Wagenblatt A, Pawlita M, Schmitt M. High-throughput SNP-based authentication of human cell lines. *Int J Cancer*. 2013;**132**:308–14.
48 Schmitt M, Pawlita M. High-throughput detection and multiplex identification of cell contaminations. *Nucleic Acids Res*. 2009;**37**:e119.
49 Justus CR, Leffler N, Ruiz-Echevarria M, Yang LV. In vitro cell migration and invasion assays. *J Vis Exp*. 2014;e51046. https://doi.org/10.3791/51046
50 Even I, Reidenbach S, Schlechter T, Berns N, Herold R, Roth W, et al. DLIC1, but not DLIC2, is upregulated in colon cancer and this contributes to proliferative overgrowth and migratory characteristics of cancer cells. *FEBS J*. 2019;**286**:803–20.
51 Rappe U, Schlechter T, Aschoff M, Hotz-Wagenblatt A, Hofmann I. Nuclear ARVCF protein binds splicing factors and contributes to the regulation of alternative splicing. *J Biol Chem*. 2014;**289**:12421–34.

Article

TRANSPARENT PROCESS OPEN ACCESS

EMBO Molecular Medicine

A whole-genome scan for Artemisinin cytotoxicity reveals a novel therapy for human brain tumors

Jasmin Taubenschmid-Stowers[1,*,†,‡], Michael Orthofer[2], Anna Laemmerer[3,4], Christian Krauditsch[1], Marianna Rózsová[2], Christian Studer[5], Daniela Lötsch[3,6], Johannes Gojo[4], Lisa Gabler[3,7,8], Matheus Dyczynski[2], Thomas Efferth[9], Astrid Hagelkruys[1], Georg Widhalm[6], Andreas Peyrl[4], Sabine Spiegl-Kreinecker[10], Dominic Hoepfner[5], Shan Bian[1,11,12], Walter Berger[3], Juergen A Knoblich[1], Ulrich Elling[1], Moritz Horn[2] & Josef M Penninger[1,13,**]

Abstract

The natural compound Artemisinin is the most widely used antimalarial drug worldwide. Based on its cytotoxicity, it is also used for anticancer therapy. Artemisinin and its derivates are endoperoxides that damage proteins in eukaryotic cells; their definite mechanism of action and host cell targets, however, have remained largely elusive. Using yeast and haploid stem cell screening, we demonstrate that a single cellular pathway, namely porphyrin (heme) biosynthesis, is required for the cytotoxicity of Artemisinins. Genetic or pharmacological modulation of porphyrin production is sufficient to alter its cytotoxicity in eukaryotic cells. Using multiple model systems of human brain tumor development, such as cerebral glioblastoma organoids, and patient-derived tumor spheroids, we sensitize cancer cells to dihydroartemisinin using the clinically approved porphyrin enhancer and surgical fluorescence marker 5-aminolevulinic acid, 5-ALA. A combination treatment of Artemisinins and 5-ALA markedly and specifically killed brain tumor cells in all model systems tested, including orthotopic patient-derived xenografts *in vivo*. These data uncover the critical molecular pathway for Artemisinin cytotoxicity and a sensitization strategy to treat different brain tumors, including drug-resistant human glioblastomas.

Keywords 5-ALA; Artemisinin; genome wide screen; glioblastoma therapy; porphyrin biogenesis

Subject Categories Cancer; Pharmacology & Drug Discovery

DOI 10.15252/emmm.202216959 | Received 29 September 2022 | Revised 14 December 2022 | Accepted 22 December 2022 | Published online 6 February 2023

EMBO Mol Med (2023) 15: e16959

Introduction

Artemisia annua, or *sweet wormwood*, extracts have been used in traditional Chinese medicine for thousands of years to treat fever, colds, and other maladies (Efferth, 2017). In the 1970s, the active compound of *Artemisia annua*, called Artemisinin, was first isolated and described as an antimalarial drug by the Chinese scientist Tu Youyou, who was awarded the Nobel Prize in Medicine in 2015 for its discovery. Artemisinin, and its derivatives such as dihydroartemisinin (DHA) or artesunate (ARS), is one of the most commonly used antimalarial drugs worldwide (Klayman, 1985; Bosman & Mendis, 2007). It kills the unicellular parasite *P. falciparum* that causes malaria, in all of its life stages (Aweeka & German, 2008). More recently, potent anticancer properties of Artemisinin have been recognized (Krishna *et al*, 2008). The variety of the different functions of Artemisinin and its applications have

1 IMBA, Institute of Molecular Biotechnology of the Austrian Academy of Sciences, Vienna Biocenter, Vienna, Austria
2 JLP Health GmbH, Vienna, Austria
3 Center for Cancer Research and Comprehensive Cancer Center-Central Nervous System Tumor Unit, Medical University of Vienna, Vienna, Austria
4 Department of Pediatrics and Adolescent Medicine and Comprehensive Center for Pediatrics, Medical University of Vienna, Vienna, Austria
5 Novartis Institutes for BioMedical Research, Basel, Switzerland
6 Department of Neurosurgery, Medical University Vienna, Vienna, Austria
7 Department of Pediatric Oncology, Dana-Farber Boston Children's Cancer and Blood Disorders Center, Boston, MA, USA
8 Broad Institute of Harvard and MIT, Cambridge, MA, USA
9 Department of Pharmaceutical Biology, Institute of Pharmaceutical and Biomedical Sciences, Johannes Gutenberg University, Mainz, Germany
10 Department of Neurosurgery, Kepler University Hospital GmbH, Johannes Kepler University Linz, Linz, Austria
11 Institute for Regenerative Medicine, Shanghai East Hospital, School of Life Sciences and Technology, Tongji University, Shanghai, China
12 Frontier Science Center for Stem Cell Research, Tongji University, Shanghai, China
13 Department of Medical Genetics, Life Sciences Institute, University of British Columbia, Vancouver, BC, Canada
*Corresponding author. Tel: +1 604 822 2421; E-mail: jstowers@altoslabs.com
**Corresponding author. Tel: 1 604 397 3222; E-mail: josef.penninger@ubc.ca
†Present address: Epigenetics Programme, Babraham Institute, Cambridge, UK
‡Present address: Altos Labs Cambridge Institute of Science, Cambridge, UK

pointed toward a wide-ranging mechanism of action in eukaryotic cells.

Biochemically, Artemisinin is an endoperoxide. Its endoperoxide properties are required for its antimalarial effect (Meshnick *et al*, 1996). Once the endoperoxide bridge is being cleaved, Artemisinin gets activated and leads to the production of reactive oxygen species (ROS) and free radicals, which subsequently alkylate susceptible proteins and macromolecules in the cell. This alkylation reaction alters the structure and function of proteins, damages DNA, and induces cellular stress, eventually resulting in cell death. In addition, it has been reported that Artemisinin associates with a wide range of cellular proteins thereby affecting multiple pathways, including glycolysis, protein biosynthesis, mitochondrial processes, and antioxidant responses (Zhang *et al*, 2015; Ismail *et al*, 2016). While definite regulators or activators of Artemisinin are still being debated, free or complexed iron, such as in haem of hemoglobin, are considered strong candidates. However, Artemisinin's promiscuous binding properties, together with the high number of reported functions, have so far hindered the identification of its definite cellular targets (Mbengue *et al*, 2015; Straimer *et al*, 2015; Tilley *et al*, 2016). As an increasing number of Artemisinin-resistant malaria cases are surfacing and at high doses, Artemisinin exerts strong cytotoxic activity, it is imperative to delineate the compound's mechanism of action.

To identify the essential endogenous Artemisinin targets in eukaryotic cells, we employed two independent, genetically tractable screening systems: HIP-HOP profiling in *S. cerevisiae* and haploid mutagenesis in mouse embryonic stem cells (ESCs). Using genome-wide screens, we identified mitochondrial function and specifically, porphyrin biosynthesis, as the essential pathway for dihydroartemisinin toxicity in eukaryotic cells. Genetic and pharmacological manipulation of porphyrin production was sufficient to alter the sensitivity of multiple murine and human tumor cells to DHA *in vitro*. Sensitization of this pathway using the clinically approved photodynamic porphyrin enhancer and surgical fluorescence marker 5-ALA markedly increased the anticancer activity of Artemisinin and its derivatives not just in human cerebral tumor organoids and patient-derived brain tumor spheroids but also in orthotopic patient-derived xenografts *in vivo*—thus identifying a novel treatment option for yet largely untreatable brain tumors such as glioblastomas.

Results

HIP-HOP yeast screens identify porphyrin biosynthesis as target for Artemisinin toxicity

To identify factors and pathways required for Artemisinin activity in eukaryotic cells in an unbiased manner, we used two independent, genetically tractable model systems for high-throughput screening: We first employed HIP-HOP chemogenomic phenotypic profiling in yeast (*Saccharomyces cerevisiae*), and second, insertional mutagenesis and forward genetic screening in haploid mouse ESCs (Fig 1A; Elling *et al*, 2011; Hoepfner *et al*, 2014). Chemogenomic approaches in yeast have identified primary targets or mechanism of action of compounds, for instance, finding mTOR as a Rapamycin target (Roemer *et al*, 2011a). Haploinsufficiency profiling (HIP) exploits the increased sensitivity toward a compound after lowering the dosage of the target-encoding gene from two copies to one copy in diploid yeast. In the complementary approach, homozygous deletion profiling (HOP), both copies of nonessential genes are deleted, identifying synthetic lethality upon target inhibition (Giaever *et al*, 1999; Roemer *et al*, 2011b; Hoepfner *et al*, 2014).

Haploinsufficiency profiling was performed as previously described (Hoepfner *et al*, 2014). The sensitivity of diploid wild-type yeast strains to dihydroartemisinin was assessed based on growth rates in the presence of the compound (Fig EV1A–C). HIP profiling of dihydroartemisinin in yeast revealed a single, prominent hit—the mitochondrial inner membrane protease complex (iAAA) subunit Yme1 (Fig 1B). Yme1 is required for mitochondrial protein folding and degradation, as well as its structure, turnover, and function (Dunn *et al*, 2006). Additional genes identified from the dihydroartemisinin HIP profile included the second major protease complex (mAAA) constituents Yta10 (AFG3) and Yta12 (RCA1) (Arlt *et al*, 1996) and the mitochondrial intermembrane space import and assembly protein 40, Mia40 (Morales *et al*, 1992; Chacinska *et al*, 2004) (Fig 1B).

Homozygous profiling (HOP) of yeast mutants was performed under similar conditions as HIP but based on growth rates of haploid strains. Sensitivity and relevance analysis identified Dap1 as the strongest growth altering factor in the presence of dihydroartemisinin (Fig 1C). Dap1 is a heme-binding protein that is involved in the regulation of cytochrome P450 and DNA damage responses (Craven *et al*, 2007). The HOP profile also included several mitochondrial factors such as the mitochondrial inner membrane complex proteins Fcj1 (MIC60) and Aim13 (MIC19), the mitochondrial membrane chaperone Tim13 and the overlapping ORF *YGR182c*. Analysis for abundant cellular processes in both the HIP and HOP yeast profiles by GO-term analysis confirmed strong enrichment for genes involved in mitochondrial processes (Fig 1D).

Notably, profiling of wild-type yeast strains revealed marked colony growth differences in the presence of Artemisinin. High concentrations of the compound induced the appearance of small yeast colonies that displayed increased resistance to dihydroartemisinin (Fig EV1B). Dihydroartemisinin treated wild-type yeast showed normal budding and growth phenotypes on fermentable (YPD, glucose) carbon sources (Fig EV1C), but were not viable on nonfermentable (YPEG, ethanol/glycerol) carbon sources (Fig EV1D). Additionally, such small colonies had lost their functional mitochondria (Nunnari & Walter, 1996; Fig 1E; Fig EV1E). These growth properties and deficient phenotypes are reminiscent of yeast petite mutants that display smaller colony size and oxidative phosphorylation defects, preventing them to grow on nonfermentable carbon sources.

Our most significant HIP hit, YME1, has been previously described as petite-negative (thus unable to form such small colonies) and highly dependent on intact mitochondria even in the presence of fermentable carbon sources (Thorsness *et al*, 1993). The identification of the YME1 strain in the HIP profile together with the phenotype of reduced growth rates in the presence of dihydroartemisinin (Fig 1F) suggested a general hypersensitivity of petite-minus strains to the compound. We thus assessed the growth rates of two other well-characterized yeast strains that are deficient for the mitochondrial import proteins Tom70 and Tim18, upon dihydroartemisinin treatment. Both mutant strains failed to form petites

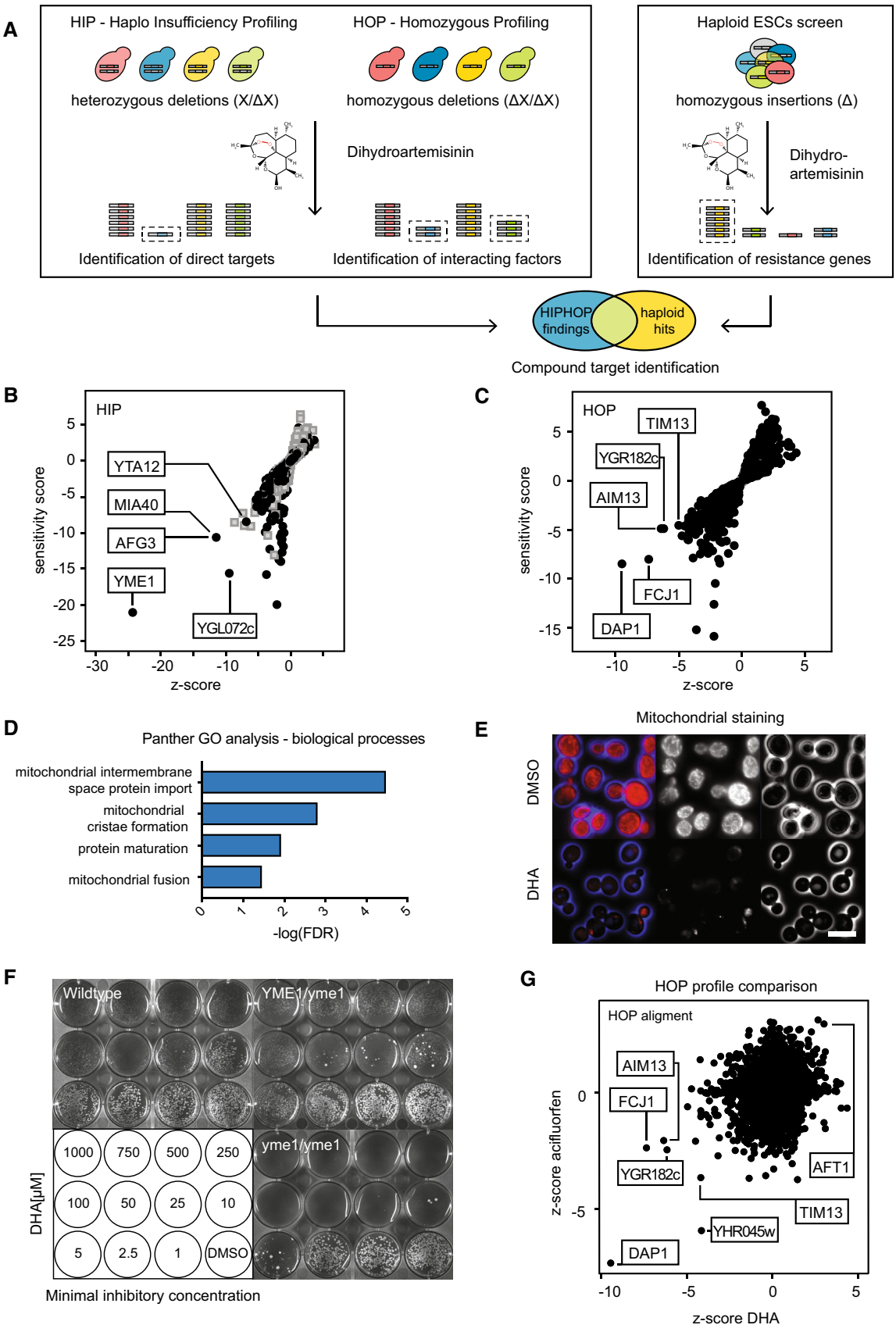

Figure 1.

Figure 1. Mitochondria are key modulators of dihydroartemisinin toxicity in yeast.

A Schematic of yeast HIP-HOP and haploid embryonic stem cell screening for compound target identification.
B Haploinsufficiency profiling (HIP) of a yeast deletion collection at sublethal concentrations (IC_{30}, 3 μM) of dihydroartemisinin (DHA). Profile is plotted by sensitivity and z-score (i.e., relevance, for more information see materials and methods). Strains with essential genes are indicated in gray, relevant mutants of nonessential genes (black) are labeled.
C Homozygous profile (HOP) of the yeast deletion collection with DHA (IC_{10}, 10 μM). Sensitivity and z-scores are plotted.
D GO-term analysis of HIP-HOP hits.
E Mitochondrial (MitoTracker) staining of DMSO (upper panel) or DHA (lower panel) treated cells. Scale bar 5 μm.
F Minimal inhibitory concentrations of DHA treated wild-type, heterozygous, (*YME1*/*yme1*) and homozygous (*yme1*/*yme1*) mutant strains. Plates were imaged after 72 h.
G HOP profile alignment of z-scores (significances) of DHA and acifluorfen. Z-scores couple the sensitivity score of a strain in a given profile to the variability in sensitivity of that strain across all the compounds tested.

(i.e., small yeast colonies) resulting in higher susceptibility to the antimalarial compound (Dunn *et al*, 2006; Fig EV1F), thus confirming the requirement of functional mitochondria for dihydroartemisinin toxicity in yeast. Lastly, comparison of the dihydroartemisinin HOP profile to ~ 4,000 independent compound analyses in the HIP-HOP chemogenomics database identified acifluorfen (Matringe *et al*, 1989) as the most analogous substance to the antimalarial compound (Fig 1G). Acifluorfen is an inhibitor of protoporphyrinogen oxidase, PPOX, an inner mitochondrial membrane enzyme that is involved in porphyrin or heme production in cells and targets the same set of mitochondrial proteins as those that were found by our dihydroartemisinin screen (Tim13, Aim13 (MIC19), Fcj1 (MIC60), and Ubx2) (Witkowski & Halling, 1989). These results point toward a specific role of mitochondrial porphyrin production in Artemisinin toxicity in yeast.

Haploid stem cell screens identify porphyrin biosynthesis as target for Artemisinin toxicity

We conducted a reciprocal screen to identify targets of dihydroartemisinin in haploid murine stem cells (haESC) using genome-wide mutagenesis (Fig 2A). In order to establish screening conditions, we determined LD values (lethal dosage) for the compound in wild-type haploid ESCs and assessed growth rates in different murine and human tumor cell lines (Fig EV1G and H). For the generation of genome-wide mutant ESC libraries, we used two targeting systems for insertional mutagenesis: Retrovirus and Tol2 transposons (Schnütgen *et al*, 2008; Elling *et al*, 2011). Selection of those two independent libraries led to the identification and recovery of dihydroartemisinin-resistant colonies from the mutagenized cell pools, but not from control cells. Upon expansion and mapping of their insertion sites, enrichment scores based on loss-of-function (LOF) analysis were determined (Datasets EV1 and EV2).

Haploid mutagenesis and dihydroartemisinin compound screening identified the enzyme, protoporphyrinogen oxidase, PPOX, as the top hit in both mutant libraries. PPOX is an inner mitochondrial membrane enzyme involved in cellular porphyrin or heme production. Its inhibitor, acifluorfen, also had the most similar HOP chemogenomic profile to dihydroartemisinin in yeast (Fig 1G). Intriguingly, genetic mutants of every single enzyme of the porphyrin biosynthesis pathway, both in mitochondria (Alas1, Cpox, Ppox, Fech) and the cytoplasm (Alad, Hmbs, Uros, Urod), were recovered from the screen, as well as essentially all relevant co-factor-producing enzymes (Lias, Ogdh, Dlst, Lipt1, Lipt2, Pdxk) and pathways feeding into the protoporphyrin or heme biosynthesis (Fig 2B; Fig EV1I; Datasets EV1 and EV2). GO term analysis of the dihydroartemisinin screening profile confirmed porphyrin biosynthesis as the only significantly targeted pathway in the context of dihydroartemisinin toxicity (Fig 2C). Thus, similar to HIP-HOP chemogenomic profiling, forward genetic screening in haESCs delineates porphyrin biosynthesis as the definitive and essential pathway for dihydroartemisinin cytotoxicity.

To confirm the hits from the high-throughput dihydroartemisinin screen, we tested single mutant ESC clones for their susceptibility to dihydroartemisinin. Resistant colonies were recovered from both mutant libraries from the screen and tested individually. We separately transduced cell lines with a Cre expression construct to invert the splice acceptor knockout cassette by recombination (Cre_Cherry_puroR) or maintained it in the original orientation (GFP-puro). Sister cell lines were mixed, cultured together and their relative growth rates were monitored in the presence and absence of dihydroartemisinin in a competition assay. While the relative amounts of labeled cells in a mixed population of mutant and wildtype cells did not change over time in the absence of the compound, dihydroartemisinin exposure resulted in selective loss of wild-type haploid ESCs (mCherry_Cre) and strong expansion of knockout sister cells (GFP) and thus a shift in the ratios of fluorescent cells. Insertion site mapping of resistant, competition assay validated cell lines by inverse PCR and Sanger sequencing confirmed disruption of porphyrin biosynthesis pathway components in those cells (Fig 2D). These results show that mutations of porphyrin biosynthesis pathway enzymes cause resistance to the cytotoxic effects of dihydroartemisinin.

Porphyrin biosynthesis is sufficient to alter cellular sensitivity to Artemisinin toxicity

To corroborate that modulation of cellular porphyrin biosynthesis is sufficient to alter susceptibility to dihydroartemisinin, we used a pharmacological inhibitor of porphyrin/heme biosynthesis, the protoporphyrinogen oxidase (PPOX) inhibitor acifluorfen, which blocks conversion of protoporphyrinogen IX to protoporphyrin IX. Treatment of mouse ESCs with acifluorfen markedly increased their resistance to dihydroartemisinin (Fig 3A; Witkowski & Halling, 1989). Conversely, when we enhanced porphyrin production using the nonproteinogenic amino acid and endogenous alanine analogue precursor δ-aminolaevulinic acid (5-ALA), and the sensitivity of ESCs to dihydroartemisinin cytotoxicity was significantly increased (Fig 3B). We next assayed if different murine and human cancer cell lines respond similarly to the combinatorial treatment,

independent of basal growth and sensitivity rates (Fig EV1G and H). We could confirm that all tested cancer cell lines gained hypersensitivity to dihydroartemisinin (Fig EV2A and B). Importantly, we also observed that the protoporphyrin inhibitor acifluorfen increased resistance of glioblastoma cells to dihydroartemisinin (Fig 3C) and reciprocally, 5-ALA-induced hypersensitivity in three independently

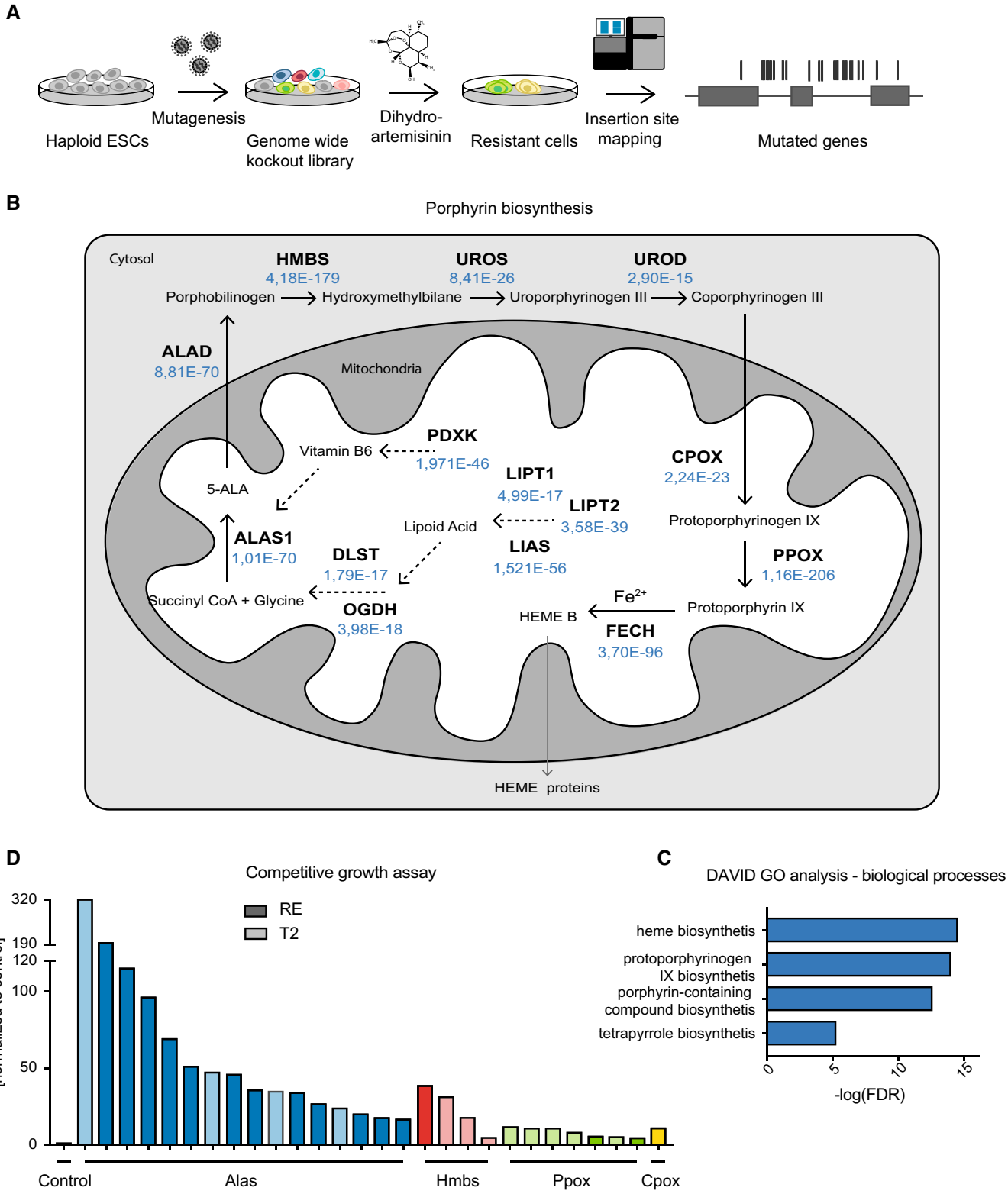

Figure 2.

Figure 2. Haploid screening in mouse stem cells delineates porphyrin biosynthesis as an essential prerequisite for dihydroartemisinin toxicity.

A Schematic of haploid embryonic stem cell screens for compound target identification.

B Porphyrin biogenesis pathway. Subcellular location (cytosol, mitochondria) and loss-of-function scores (italic blue) of major enzymes (bold, capitalized) and co-factors (normal, capitalized) of retroviral mutagenesis screen are indicated. 5-aminolevulinic acid (5-ALA), ALA synthase 1 (ALAS1), ALA dehydratase (ALAD), porphobilinogen deaminase (HMBS), uroporphyrinogen III synthase (UROS), uroporphyrinogen III decarboxylase (UROD), coproporphyrinogen III oxidase (CPOX), protoporphyrinogen oxidase (PPOX), ferrochelatase (FECH), pyridoxal kinase (PDXK), lipoyltransferase 1, 2 (LIPT1, LITP2), lipoic acid synthetase (LIAS), oxoglutarate dehydrogenase (OGDH), dihydrolipoamide S-succinyltransferase (DLST).

C GO-term analysis reveals porphyrin biogenesis as the major pathway targeted by DHA.

D Competitive growth assay of DHA-resistant single cell clones. Wild-type ($mCherry^+$_Cre_Puro) and knockout (GFP^+_Puro) sister clones were derived from mutant (retrovirus—intron RE, darker shading, Tol2 transposon—intron T2, lighter shading) resistant colonies, treated with DHA, analyzed with flow cytometry and Sanger sequenced for insertion site mapping.

derived human primary glioblastoma cell lines (Fig 3D; Fig EV2C and D).

Mechanistically, dihydroartemisinin has been shown to lead to the production of ROS (Witkowski & Halling, 1989; Antoine *et al*, 2014). Assessing ROS levels (using the redox-sensitive fluorescent probe dihydroethidium, DHE) confirmed increased levels of ROS upon dihydroartemisinin treatment (Fig EV2E and F). We next assessed if 5-ALA had any effect on ROS production in the absence or presence of dihydroartemisinin. While low concentrations of dihydroartemisinin and 5-ALA alone had little or no effect on ROS levels or viability, the combination of both resulted in elevated ROS as well as a strong increase in cell death in human Jurkat T cells as well as human SHSY5Y neuroblastoma cells (Fig 3E and F; Fig EV2G and H). Similarly, and previously associated with dihydroartemisinin-induced ROS induction (Antoine *et al*, 2014), mitochondrial polarization ($\Delta\Psi m$, as assessed by the mitochondrial membrane potential probe JC-1) was strongly elevated when cells were exposed to both dihydroartemisinin and 5-ALA (Fig EV2I). Importantly, all of these phenotypes (ROS induction, mitochondrial depolarization, and cell death) could be suppressed by pharmacological inhibition of porphyrin production using a Ppox inhibitor (Fig 3E and F; Fig EV2G–I). These data indicate that modification of porphyrin biosynthesis is sufficient to modulate the sensitivity of multiple murine and human tumor cell lines to dihydroartemisinin toxicity.

5-ALA and Artemisinin therapy in engineered human cerebral brain tumor organoids

Altered cell metabolism and upregulation of porphyrin production are frequently observed in human cancer cells (Navone *et al*, 1990). In human glioblastoma patients, elevated porphyrin biosynthesis is used diagnostically and therapeutically to localize and target tumor tissue, as porphyrin precursors (i.e., protoporphyrins) show strong fluorescence that can be monitored and functionally exploited *in vivo* (Batlle, 1993; Zhao *et al*, 2013; Hadjipanayis *et al*, 2015). Importantly, during fluorescence-guided resection of brain tumors, preoperative oral administration of the clinically approved porphyrin enhancer 5-ALA is used to distinguish high-grade glioma from brain tissue, as fluorescent protoporphyrins, such as protoporphyrin IX, accumulate specifically in tumor cells but not the surrounding tissue, thus demonstrating selectively altered porphyrin biosynthesis in cancer (Stummer *et al*, 1998). Similarly to 5-ALA, Artemisinin and its derivatives can readily pass through the blood brain barrier (de Vries & Dien, 1996). Since 5-ALA is used to mark brain tumors for surgery, and the porphyrin pathway was found to be essential for Artemisinin toxicity, we wanted to apply our findings to treat therapy-resistant brain cancer. We thus assessed if altered porphyrin biosynthesis in brain tumors can be therapeutically exploited, using a combination treatment of 5-ALA and dihydroartemisinin.

We used a recently established human cerebral tumor organoid model, which is based on genetic manipulation of neuronal precursors in the course of brain organoid development, thus recapitulating key aspects of human tumor formation under controlled *in vitro* conditions (Lancaster *et al*, 2013; Bian *et al*, 2018). Tumor cells in the organoids were simultaneously labeled with GFP, allowing monitoring of tumor growth over time and controlled compound profiling *in vitro* (Fig 4A). We first assessed tumor growth rates in the presence of dihydroartemisinin and/or 5-ALA in a central nervous system primitive neuroectodermal tumor (CNS-PNET-like) neoplasm model, which is based on the overexpression of the c-MYC oncogene (Bian *et al*, 2018; Fig EV2J). The highly malignant brain tumor organoids were treated with different doses of 5-ALA, dihydroartemisinin, or a combination of both (Fig 4B). Since very high concentrations of 5-ALA or dihydroartemisinin alone resulted in notable growth inhibition of GFP-positive tumor organoids (Fig EV2J), concentrations were chosen for all subsequent experiments where the individual compounds had no notable effects on tumor or organoid growth. Strikingly, the combination of both 5-ALA and dihydroartemisinin together markedly decreased GFP-positive tumor cells in human cerebral organoids (Fig 4C and D; Fig EV2K). Quantification of the tumor tissue area at different time points (d3, d5) (Fig 4E; Fig EV2L) as well as FACS analysis (d5, d7) (Fig 4F) confirmed strong reduction of GFP-positive cells upon 5-ALA and dihydroartemisinin combination treatment. Immunohistochemistry and histology of sectioned brain organoids further showed that 5-ALA treatment resulted in the loss of GFP-positive tumor tissue, but had no apparent effect on nontransformed neuronal tissue in the cerebral organoids, such as rosette-like structures and MAP2 or SOX2 expressing neuronal and progenitor cells (Figs EV2M and EV3A–C). Altogether, these data suggest that 5-ALA and dihydroartemisinin combination strongly reduces the number of tumor cells in a human primitive neuroectodermal tumor (CNS-PNET-like) organoid model *in vitro*.

Since we observed a marked effect of 5-ALA and dihydroartemisinin on ROS levels in cells, we performed DHE staining and analysis of the Myc overexpressing brain tumor organoids. Whereas GFP-positive tumor cells displayed slightly higher basal ROS signals as compared to GFP-negative wild-type cells (as assessed by DHE staining and FACS analysis), ROS levels markedly increased upon 5-ALA and dihydroartemisinin double treatment,

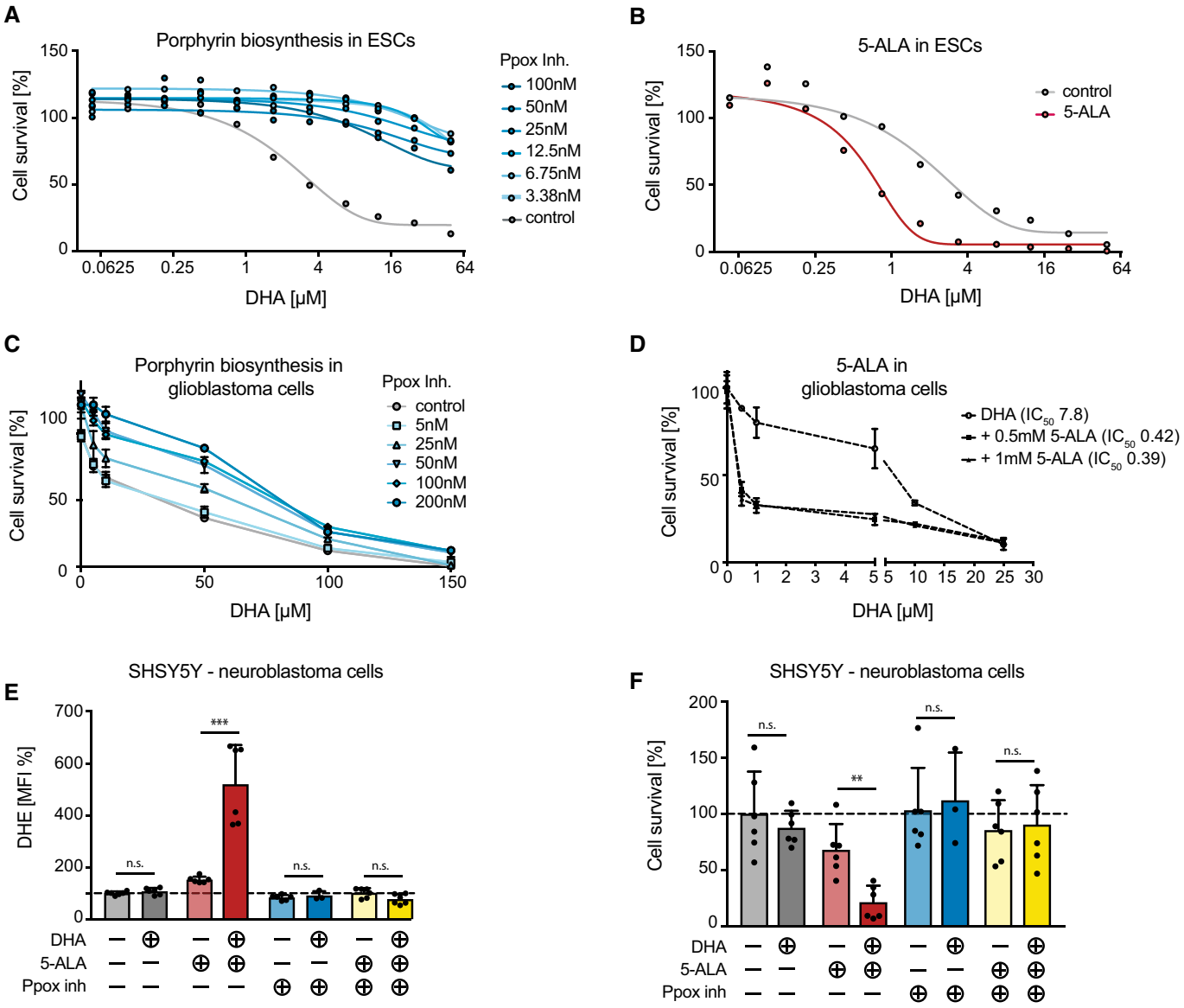

Figure 3. Modulation of porphyrin biosynthesis is sufficient to alter dihydroartemisinin toxicity via ROS generation.

A, B Cell survival of dihydroartemisinin-treated ESCs in combination with (A) the Ppox inhibitor acifluorfen or upon and (B) 5-ALA administration. Alamar Blue staining was used to assess viability after 72 h of treatment.

C, D Cell survival of DHA treated primary human glioblastoma cells from cancer patients and in combination with (C) the Ppox inhibitor acifluorfen (BTL90 cells) or upon (D) 5-ALA administration (VBT12 cells). Viability was assessed using CellTiter-Glo after 72 h. Experiments were performed in triplicate. Values are mean ± SD.

E, F (E) ROS levels (DHE staining, PE 582/15 nm—MFI) and (F) cell survival of DHA (0.5 μM), 5-ALA (0.25 mM) or Ppox inhibitor (10 μM) treated human neuroblastoma cells (SHSY5Y). Fluorescence of DHE (ROS levels) and cell numbers (survival) were assessed by flow cytometry and automated cell counting. The experiments were performed two times, in triplicate each. Values indicate mean ± SD. n.s. nonsignificant, $^{**}P < 0.01$, $^{***}P < 0.001$, unpaired Student's *t*-test.

especially in GFP-positive cancer cells (Fig 4G; Fig EV3D). As elevated intracellular ROS also causes DNA damage (Cadet & Wagner, 2013), we assessed the amount of DNA double-strand breaks (DSB) on organoid sections. We indeed observed a significant increase in γH2AX (phosphorylated histone H2AX)-positive cells in 5-ALA and dihydroartemisinin double-treated GFP-positive tumor tissue, but not in the control wild-type cells (Fig 4H; Fig EV3E and F). Additionally, while the basal number of apoptotic (caspase 3-positive) and proliferating cells (Ki67-positive) was increased in GFP-positive tumor cells as compared to normal tissue, apoptosis further increased in GFP-positive tumor cells upon combination treatment with dihydroartemisinin and 5-ALA (Fig EV3G–I).

As 5-ALA is routinely used clinically to visualize human high-grade gliomas during fluorescence-guided surgery, we next assessed 5-ALA and dihydroartemisinin combination treatment in an *in vitro* human glioblastoma-like neoplastic organoid model (Bian *et al*, 2018). These organoids were engineered to carry mutations of the tumor suppressor genes p53, NF1, and PTEN, together with GFP

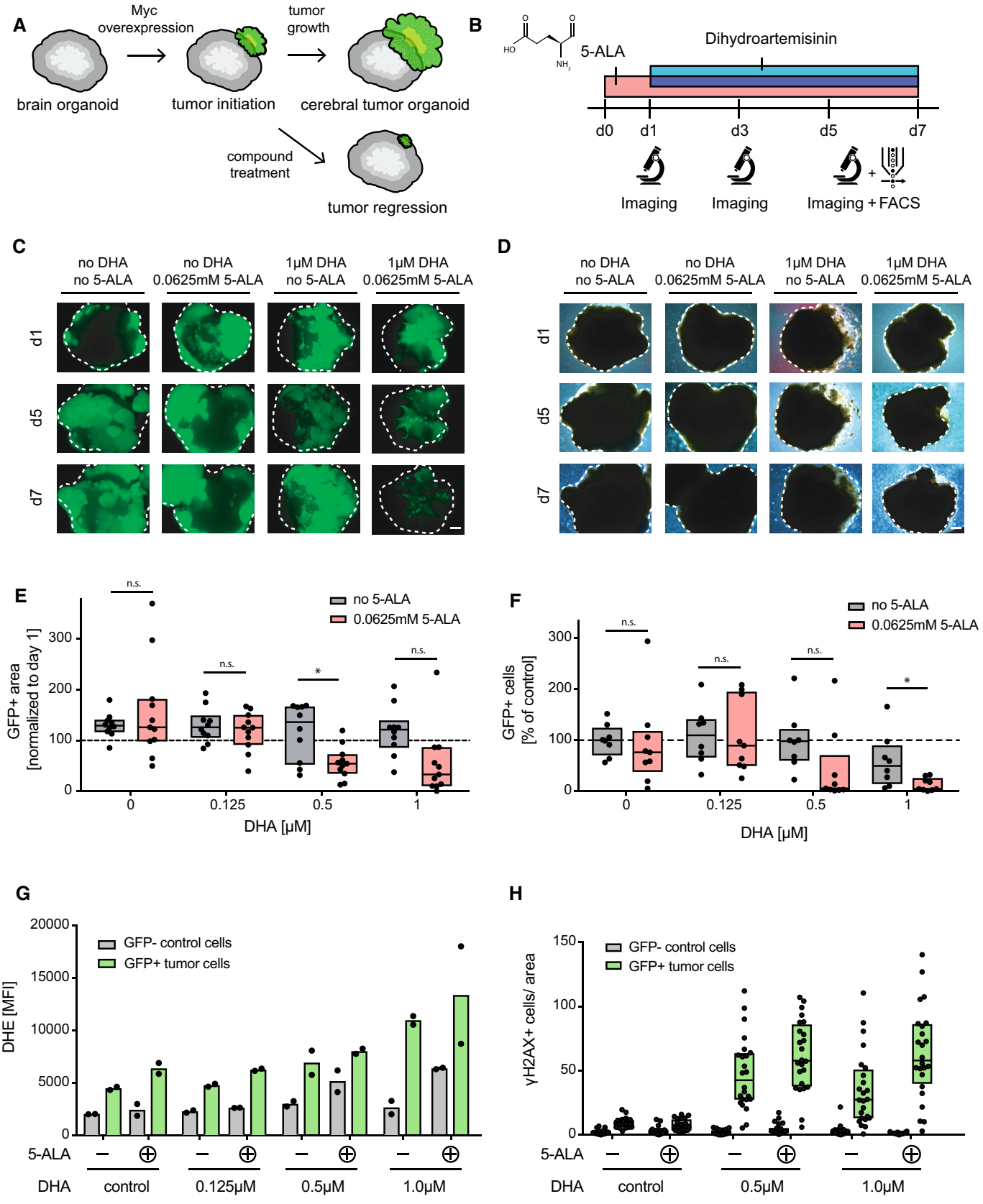

Figure 4.

Figure 4. Cerebral tumor organoids (CNS-PNET-like) display increased sensitivity to dihydroartemisinin and 5-ALA combination therapy.

A Human cerebral tumor organoids for compound profiling.

B Schematic workflow of 5-ALA- and DHA-treated organoids.

C, D (C) Fluorescence and (D) brightfield images of DMSO (control), 5-ALA (0.0625 mM), DHA (1 μM), or 5-ALA and DHA (0.0625 mM and 1 μM) treated tumor organoids (CNS-PNET-like, c-MYC overexpression). Organoids were imaged on day 1, day 5, and day 7. One experiment is shown, representative of four independent experiments. Scale bar 500 μm.

E Image analysis and quantification of GFP-positive tumor areas of the treated organoids. At least eight organoids per condition were analyzed on day 3 and normalized to day 1. Three independent experiments were performed, with two to four organoids per batch, per condition. Data are shown as box plots (25^{th}–75^{th} percentiles, median).

F Flow cytometry analysis of dissociated cerebral tumor organoids. Relative percentages of GFP^+ tumor cells of normalized to control (DMSO) are shown on day 5. At least eight organoids per condition were analyzed. Three independent experiments were performed using all conditions, with two to four organoids each per batch per condition. Box plots (25^{th}–75^{th} percentiles, median) of data are indicated.

G ROS/DHE staining and flow cytometry analysis of dissociated tumor organoids (PE, 582/15 nm). Mean fluorescence intensities (MFI) of DHE-stained GFP^+ tumor cells and GFP—control cells are indicated. $n = 2$, values are mean ± SD.

H Quantification of $\gamma H2AX^+$ cells in cerebral tumor organoids. 6 cryo-sections of three organoids each were stained for γH2AX, scanned and 25 regions of interest (ROI 2,500 μm^2) were analyzed per condition. Raw data were normalized to organoid area (per ROI) and are shown as box plots (25^{th}–75^{th} percentiles, median).

Data information: n.s., nonsignificant, $*P < 0.05$, unpaired Student's *t*-test.

that allowed us to monitor tumor growth over time in the presence of dihydroartemisinin, 5-ALA, or a combination of both. Whereas both 5-ALA and dihydroartemisinin alone had little effect on the survival of untransformed as well as transformed cells, the combination of both compounds specifically ablated GFP-positive tumor cells in the *in vitro* tumor model (Fig 5A; Fig EV4A). Quantification and image analysis of cerebral organoids confirmed progressive loss of GFP-positive tumor cells and tissue, whereas untransformed cells were not affected (Fig 5B and C; Fig EV4B). These data show that 5-ALA and dihydroartemisinin lead to increased cell death of tumor cells in two highly malignant brain tumor models, via elevated ROS levels and increased DNA damage.

Treatment of drug-resistant patient-derived glioblastoma spheroids

In addition to the mini-brain model system, we next explored the effect of the compounds dihydroartemisinin and 5-ALA in human patient-derived high-grade glioma neurospheres from children and adults who died of multidrug-resistant brain cancer, cultured under stem cell conditions. As 5-ALA is routinely used in the clinics to visualize human high-grade gliomas during fluorescence-guided surgery, porphyrin biosynthesis/metabolism in tumor cells differs from that in healthy brain tissue (Guyotat *et al*, 2016). The isolated cell models used for our therapeutic intervention experiments were classified as therapy-resistant clinically by certified oncologists and based on their growth profiles in the presence of common cancer therapeutic drugs *in vitro* (Fig EV4C and D). Upon initiation of tumor sphere formation *in vitro*, treatment with 5-ALA and dihydroartemisinin was started and growth of neurospheres as well as viability were monitored. 5-ALA treatment of patient-derived high-grade glioma cells (VBT92) in the presence of dihydroartemisinin resulted in markedly reduced formation and expansion of spheroids (Fig 6A; Fig EV4E), as well as generally reduced viability (Fig EV4F). In addition, the readhesion capacity of spheroids was assessed and analyzed upon growth of pretreated cells in 3D cell cultures; this readhesion capacity was strongly reduced upon 5-ALA and dihydroartemisinin combination treatment, but not by either compound alone (Fig 6B and C; Fig EV4G). These results could be confirmed in two additional patient-derived spheroid models of atypical teratoid rhabdoid tumors (VBT281, VBT293), which also displayed high sensitivity to dihydroartemisinin and 5-ALA as shown by reduced spheroid formation and cellular viability (Fig EV4H and I), as well as limited readhesion capacity (Fig EV4J). Moreover, when cytotoxicity was assessed in those patient-derived brain cancer cells, we observed increased levels of apoptosis (PI, Annexin V) upon double treatment with 5-ALA and dihydroartemisinin, both in 2D as well as 3D cultures (Fig EV5A and B). Mechanistically, these tumor cells also displayed higher levels of lipid peroxidation (Fig 6D; Fig EV5C and D) and a reduction of tubular mitochondrial structures upon combination treatment (Fig EV5E). However, addition of the ROS scavenger NAC (N-acetyl-l-cysteine) did not apparently increase survival and did thus not salvage patient-derived tumor cells from the combination of 5-ALA and dihydroartemisinin (Fig EV5F–I). This data confirm strong 5-ALA-induced sensitization of human patient-derived brain tumor cells to dihydroartemisinin in at least three independent *in vitro* model systems of different origin.

Combined 5-ALA and artesunate treatment reduce PDX glioblastoma growth in mice

To assess whether our combinatorial treatment exhibits synergistic antitumor activities *in vivo*, we established patient-derived xenografts (PDX) models from two subpopulations (VBT529 and VBT531) of a surgically removed, aggressive glioblastoma. Both lines were tagged with Luc2-iRFP before being injected into nude mice (Fig 7A). In an orthotopic setup where human glioblastoma cells were injected into the brain, mice were treated with 5-ALA (80 mg/kg), artesunate (ARS, 40 mg/kg), or the double combination, starting 11–14 days post-injection. Artesunate is an Artemisinin derivative that shows high brain penetrance is rapidly metabolized to dihydroartemisinin *in vivo* and is commonly used in patients and animal studies (Navaratnam *et al*, 2000). Five intraperitoneal treatments with the double combination per week resulted in a significant reduction of tumor growth as compared to the solvent control as well as to both single treatments (Fig 7B), confirming the strong synergistic antitumor activity from the *in vitro* studies. Importantly, neither treatment regimen showed noticeable effects on mouse body weight, behavior, or overall well-being (Fig EV5J).

We next asked whether drug concentrations can be increased to boost the antineoplastic effect and whether the tumor location

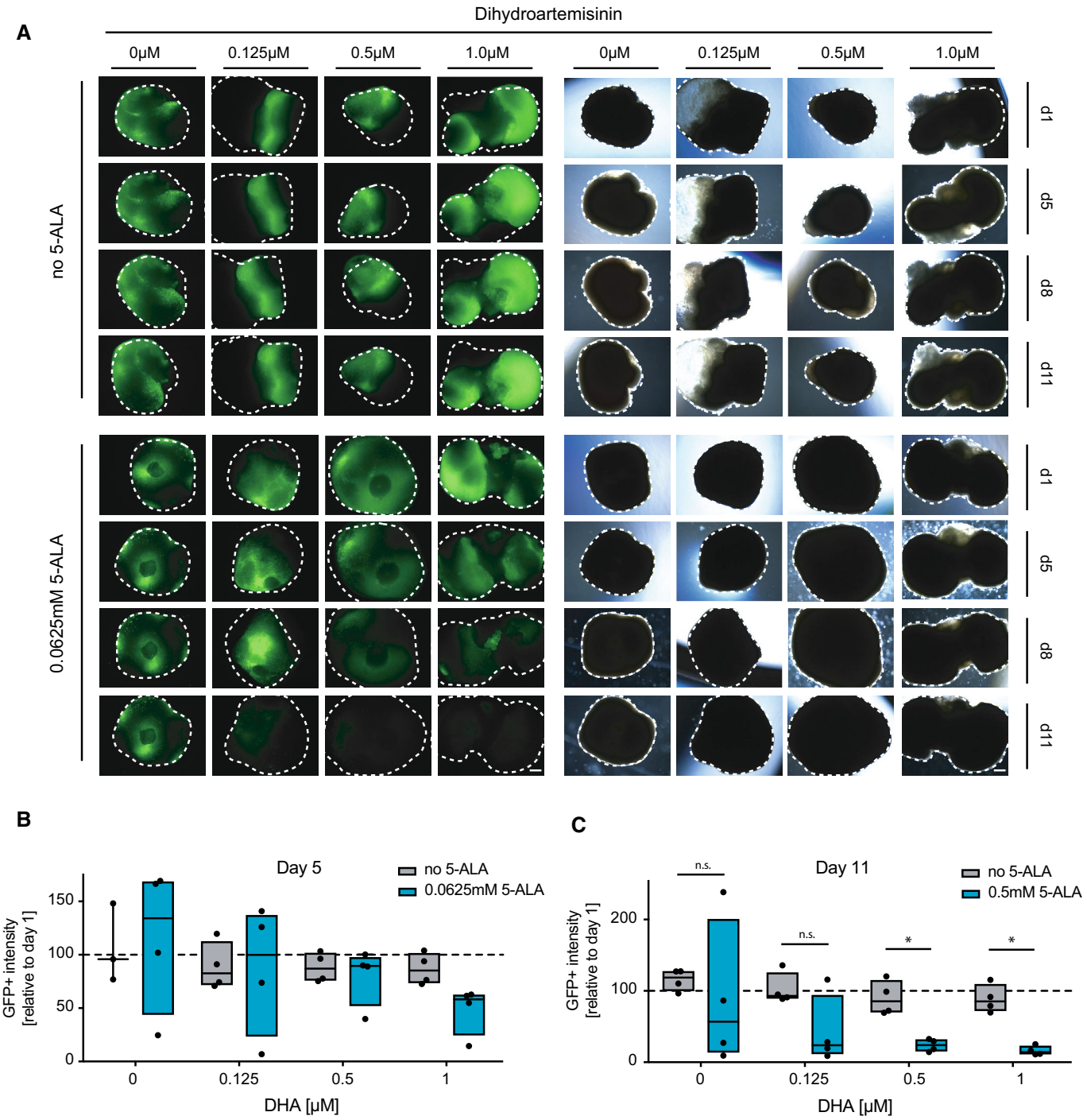

Figure 5. Dihydroartemisinin and 5-ALA combination treatment of human glioblastoma-like neoplastic organoids.

A Fluorescence (left panel) and brightfield (right panel) images of 5-ALA- and DHA-treated human cerebral tumor organoids (glioblastoma-like). Organoids were monitored on day 1, day 5, day 8, and day 11. One experiment is shown, representative of two independent experiments. Scale bar 500 μm.

B, C Image analysis and quantification of GFP-positive tumor areas of the treated organoids. Four organoids per group were analyzed on day (B) d5 and (C) d11, normalized to day 1. Data are shown as box plots (25^{th}–75^{th} percentiles, median) $n = 4$.

Data information: n.s., nonsignificant, $*P < 0.05$, unpaired Student's *t*-test.

affects treatment efficacy. Therefore, VBT529 cells were injected both into the mouse brain and flank. 6–7 days post-injection, mice were treated with the double combination (up to 120 mg/kg 5-ALA and 60 mg/kg ARS) or the control solvent 4–5 times per week for 1 month. While control mice developed malignant tumors in the brain and the flank, the combinatorial treatment significantly

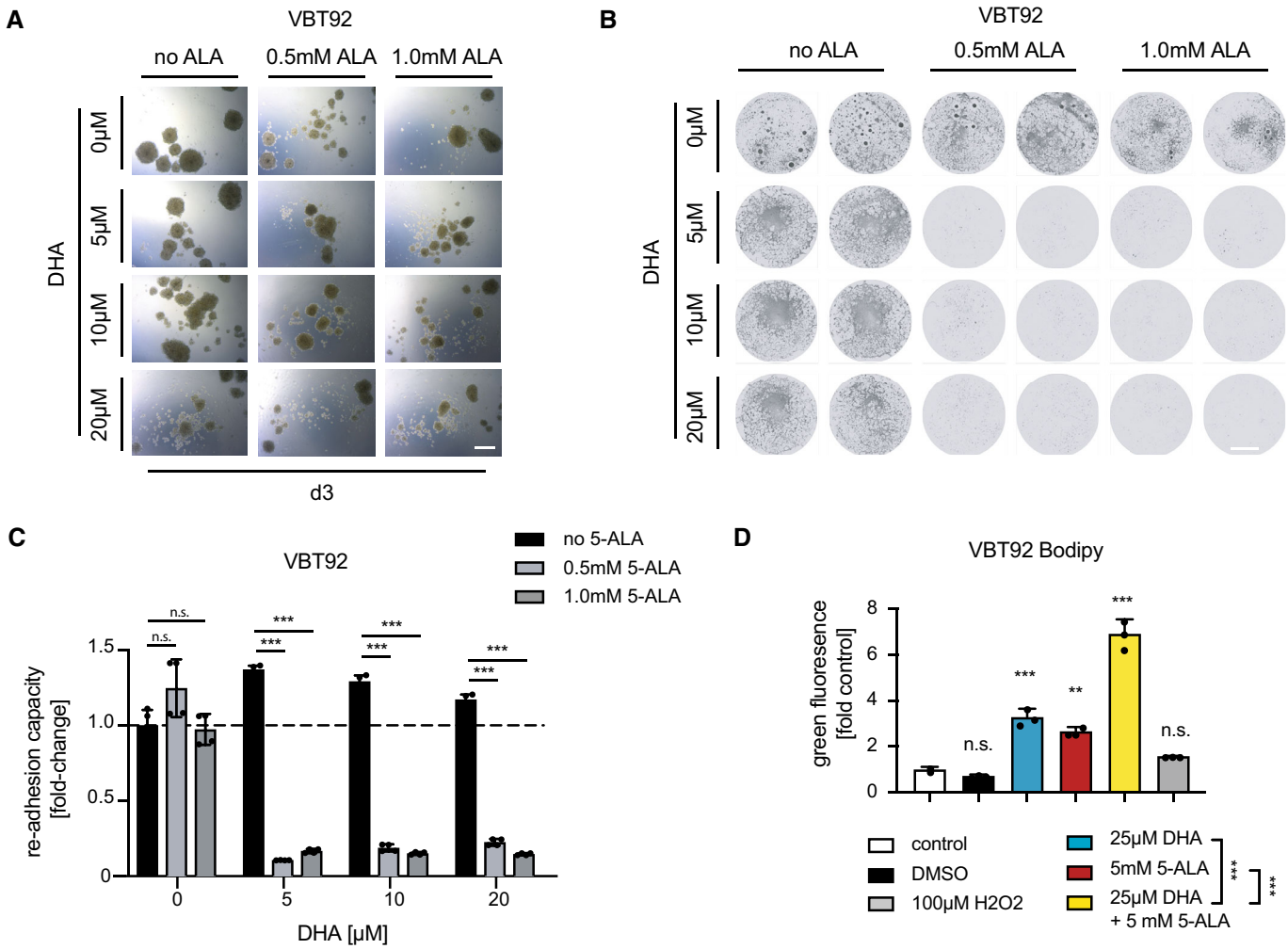

Figure 6. Human patient-derived high-grade glioma spheroids are highly susceptible to dihydroartemisinin and 5-ALA combination therapy.

A Representative brightfield images of 5-ALA- and DHA-treated patient-derived glioblastoma spheroids (VBT92). Images were taken on day 3 of culture left untreated or exposed to the indicated treatments. Scale bar 500 µm. See also Fig EV4E.

B Replating of spheroids after 3 days of 5-ALA and DHA treatment (duplicates). Representative brightfield images are shown for glioblastoma VBT92. Scale bar 500 µm.

C Quantification of the re-adhesion capacity of re-plated VBT92 spheroids as assessed by crystal violet staining and absorbance measurement. Data are shown as mean ± SD. Experiments were performed in quadruplicates.

D Lipid peroxidation in VBT92 cells treated with 5-ALA and DHA. Lipid peroxidation was measured using BODIPY™ 581/591 C11 staining and green (from red) fluorescence shift was determined using flow cytometry. Experiments were performed in triplicate; values are shown as mean ± SD.

Data information: n.s., nonsignificant, $^{**}P < 0.01$, $^{***}P < 0.001$; (C) Student's *t*-test (D) one-way ANOVA followed by Bonferroni's multiple comparisons test.

reduced tumor growth in both locations (Fig 7C–F). Intriguingly, antitumor activity was most striking in the brain, where basically no tumor progression was observed (Fig 7E and F). Mouse body weights remained unaffected in these therapeutic scenarios (Fig EV5K). The strong reduction in tumor growth manifested in a significant increase in overall survival of treated mice, which was monitored until day 76 post-injection (Fig 7G).

To elucidate why the combinatorial treatment specifically targets tumor tissue, we measured two heme pathway metabolites in brain and tumor tissue 60 min post-intraperitoneal injection of 120 mg/kg 5-ALA in control group mice. Interestingly, both assessed metabolites, porphobilinogen and protoporphyrinogen IX, showed higher levels in brain tumor as compared to the surrounding normal brain tissue upon 5-ALA treatment, indicating a higher activity of the heme biosynthesis pathway in these cells (Fig 7H). Importantly, all results obtained with the VBT529 cell line could be replicated with the second tumor line VBT531 (Fig EV5L–R). Collectively, these data demonstrate a strong synergistic activity of 5-ALA and ARS against human relevant glioblastoma models *in vivo*.

Discussion

In this work, we delineate porphyrin biosynthesis as the critical endogenous pathway for Artemisinin-triggered cytotoxicity in eukaryotic cells. Using different high-throughput genetic screening

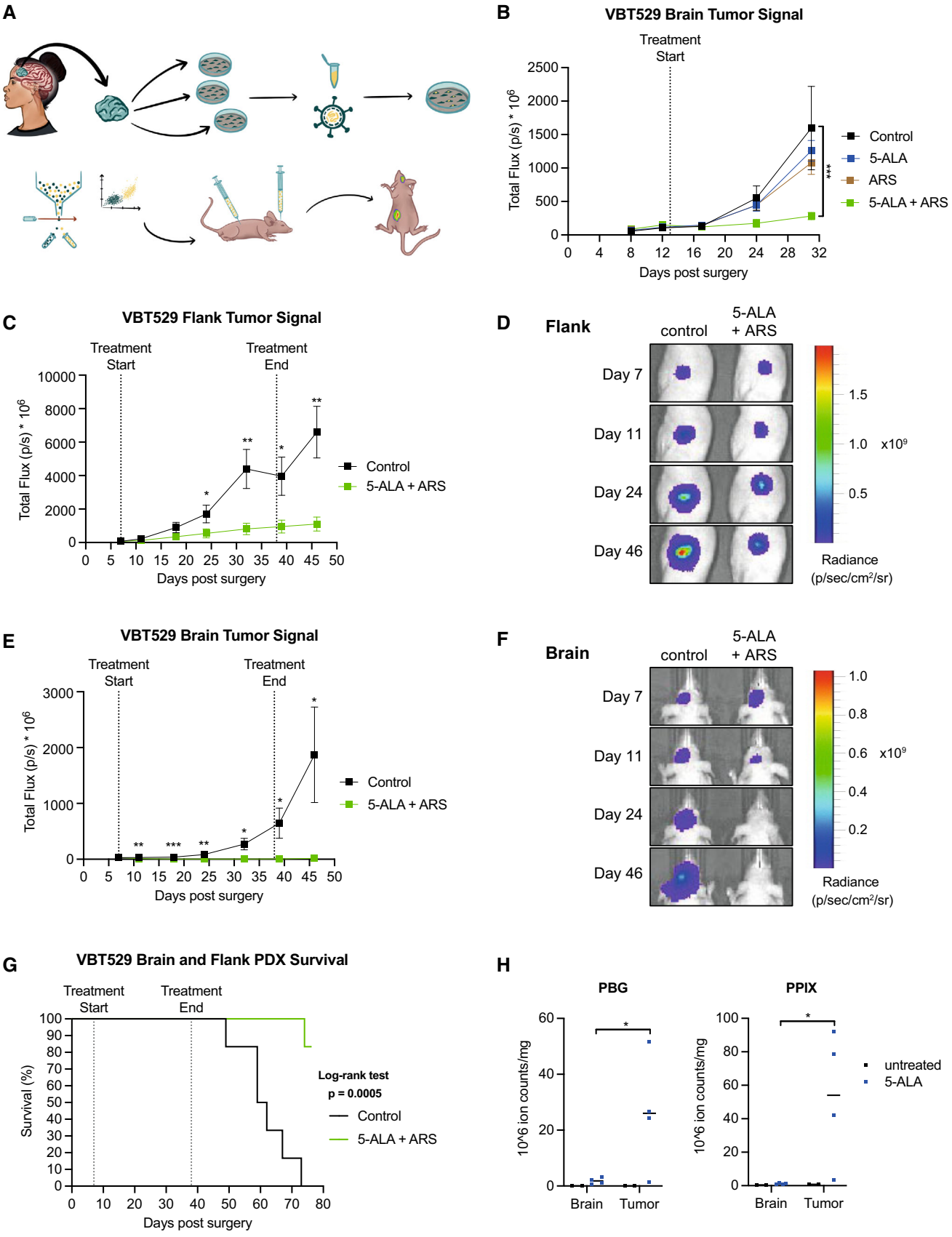

Figure 7.

Figure 7. 5-ALA and artesunate treatment reduces glioblastoma growth in mice.

A Schematic outline of flank and brain PDX models. Patient-derived tumor cells (VBT529) were cultured *in vitro* and transduced with a Luc2-iRFP lentiviral vector. Following flow cytometry sorting, LUC2 expressing cells were injected into the brain or flank and brain of *nude* mice. Upon tumor development, mice were treated with the respective compound(s) and tumor growth was monitored using the IVIS *in vivo* imaging system.

B *In vivo* efficacy comparison of solvents (control), 5-ALA, artesunate (ARS) and combined treatment in an orthotopic glioblastoma model. 11–14 days after stereotactic intracerebral injection of 2×10^5 VBT529 cells, mice received the following treatments: Control (solvents), 5-ALA (80 mg/kg), ARS (40 mg/kg), or 5-ALA plus ARS 5 times per week via intraperitoneal injection ($n \geq 5$).

C, D Quantification and representative images of the VBT529 flank tumor luminescence signal. 6–7 days after injection of 1.5×10^5 VBT529 cells into the flank, mice received the following treatments: Control (solvents) or 5-ALA plus ARS 4–5 times per week for 5 weeks via intraperitoneal injection ($n = 6$). After 4 days of treatment, concentrations of 5-ALA (100 mg/kg) and ARS (50 mg/kg) were increased to 120 and 60 mg/kg, respectively. The 20% dosage increase of both drugs was used as the body weight, behavior, and overall health of the mice were not affected by both, the lower as well as higher dosages.

E, F Quantification and representative images of VBT529 brain tumor luminescence signals. 6–7 days after stereotactic intracerebral injection of 1.5×10^5 VBT529 cells, mice received the treatments as described in (C and D) ($n = 6$).

G Kaplan–Meier survival curves of mice injected with VBT529 glioblastoma cells into the flank and brain (same mice as in C–F; $n = 6$). Mice were treated with solvents (control) or 5-ALA plus ARS (same mice as in C–F).

H Quantification of porphobilinogen (PBG) and protoporphyrin IX (PPIX) levels in untreated versus 5-ALA treated (120 mg/kg) glioblastoma-bearing mice ($n \geq 2$). Levels in tumors as compared to surrounding brain tissue are shown.

Data information: (B, C, E) Data are presented as mean ± SEM; $^*P < 0.05$, $^{**}P < 0.01$, $^{***}P < 0.001$; (B) two-way ANOVA followed by Bonferroni's multiple comparisons test; (C, E, H) Student's one-tailed, unpaired *t*-test, or (G) Log-rank (Mantel–Cox) test.

systems in two unique eukaryotic model organisms, we have independently identified mitochondrial function, and more specifically porphyrin/heme biosynthesis, to be required for the cytotoxic activity of the antimalarial and anticancer compound. Genetic as well as pharmacological modulation of porphyrin production was sufficient to modulate dihydroartemisinin toxicity, as well as to control the levels of dihydroartemisinin-induced ROS, in multiple different cellular contexts and species. Furthermore, we could show in several independent *in vitro* human cerebral tumor organoid, drug-resistant spheroid, and orthotopic PDX glioblastoma model systems that we can specifically target brain tumor cells using a combination treatment of 5-ALA and dihydroartemisinin to induce cell death.

Artemisinin and its derivatives have been widely used for the treatment of malarial and parasitic worm (helminth) infections, but in China they are also used for the therapy of systemic lupus erythematosus and liver cancer due to their cytotoxic activity at higher doses (Bessone *et al*, 2014). The exact mechanism of action of Artemisinin was not known because of the complex chemical interactions involved (Haynes *et al*, 2013). For malaria, the endoperoxide ring can be activated by heme inside the hemoglobin of the red blood cells, resulting in the production of free radicals that in turn damage susceptible proteins, resulting in the death of the parasite (Tilley *et al*, 2016). However, unlike other antimalarials that kill the parasite at a particular stage of its life cycle, Artemisinin is able to kill at all the life cycle stages (Golenser *et al*, 2006), suggesting additional targets. Moreover, it has been reported that Artemisinin can bind to a plethora of additional proteins (Zhang *et al*, 2015), further indicating that it might act on multiple cellular targets critical for its anti-inflammatory and cytotoxic activity. Our data in yeast HIP-HOP as well as murine haploid ESC screens now unequivocally and surprisingly identify a singular pathway that controls Artemisinin cytotoxicity, namely porphyrin/heme biosynthesis. In fact, while we cannot formally exclude other pathways, we identified every single enzyme involved in porphyrin/heme biosynthesis with very high significance scores, including the generation of metabolites that critically feed into this pathway. This allowed us to use the rate-limiting metabolite 5-ALA, already routinely used by neurosurgeons to intraoperatively visualize brain tumors (Zhao *et al*, 2013), to enhance porphyrin biosynthesis and thereby sensitize tumor cells to the cytotoxic effects of dihydroartemisinin. Intriguingly, this sensitization could be observed in essentially all tumor cell lines we tested and could be blocked by the Ppox inhibitor acifluorfen, again providing evidence that dihydroartemisinin cytotoxicity is critically dependent on the final step of porphyrin biosynthesis. Importantly, these data are in line with our finding that dihydroartemisinin/5-ALA treatment markedly induces ROS and thereby damages DNA as determined by γH2AX and JC-1 staining, providing a mechanistic explanation how and why Artemisinin can kill multiple types of tumor cells.

Brain tumors remain one of the deadliest neoplasms with often limited treatment options. For instance, glioblastoma is one of the most aggressive types of brain cancer, representing about 15% of all brain tumors (Young *et al*, 2015). Treatment usually involves surgery, radiation therapy, and chemotherapy with temozolomide (De Vleeschouwer *et al*, 2017). Unfortunately, despite radical multimodal treatments, glioblastomas often recur, resulting in an overall survival of approximately 15 months and 3–7% of people diagnosed with glioblastoma survive longer than 5 years (Bi & Beroukhim, 2014; Ostrom *et al*, 2016). A current clinical trial protocol is using eight different types of drugs to treat recurring glioblastoma (Parasramka *et al*, 2017). Thus, it is paramount to find novel treatment options, one of which is innovative immunotherapy such as tumor vaccines or CAR T cells (Jacob *et al*, 2020). Recent progress in the engineering of cerebral organoids from stem cells has allowed to model and experimentally dissect human brain tumor development, including glioblastomas (Bian *et al*, 2018). Using these two different models (CNS-PNET-like and glioblastoma-like neoplasm) of inducible cerebral brain tumor organoids, we were indeed able to show that a combination of 5-ALA and dihydroartemisinin selectively and efficiently kills tumor cells, while not affecting the surrounding "normal" neuronal tissue of the organoids. To further explore the clinical efficacy and recapitulate parental tumor heterogeneity, we also tested whether 5-ALA and dihydroartemisinin is cytotoxic in patient-derived brain tumor spheroids. Intriguingly, in three different patient-derived organoid models, all of which were

defined as multidrug resistant in the clinic and in *in vitro* cell assays, the addition of 5-ALA markedly sensitized the tumor cells to Artemisinin killing. Most importantly, in patient-derived xenograft models of human glioblastoma, the combination treatment of 5-ALA and the Artemisinin derivative artesunate almost entirely abolished tumor cell growth in mice *in vivo*. Notably, a recent study has also reported enhanced killing of a colon cancer cell line by 5-ALA and Artemisinin (Wang *et al*, 2017), supporting our results in engineered brain cancer organoids, patient-derived brain tumor spheroids and orthotopic PDX glioblastoma models.

In conclusion, our HIP-HOP and haploid ESC screens have identified the critical pathway of how Artemisinin kills eukaryotic cells, a pathway that appears to be conserved from yeast to human. Metabolic perturbation of this pathway, heme/porphyrin biosynthesis, can be used to abolish or sensitize tumor cells to the cytotoxic effects of Artemisinin. Since both 5-ALA and Artemisinin, as well as its derivates, have been safety tested for brain tumor surgery and literally millions of malaria patients, our drug combination could be readily translated to treat patients with yet untreatable and multidrug-resistant brain tumors.

Materials and Methods

HIP-HOP assays

The growth-inhibitory potency of compounds was determined using wild-type *S. cerevisiae* BY4743 as published in detail (Hoepfner *et al*, 2014). HIP-HOP analysis was performed as described previously (Pierce *et al*, 2006; Hoepfner *et al*, 2014). Sensitivity was computed as the median absolute deviation logarithmic (MADL) score for each compound (Dihydroartemisinin, DHA)/concentration (HIP—3 μM, HOP—10 μM) combination. Z-scores were based on a robust parametric estimation of gene variability from > 4,000 different profiles and computed as described in detail previously. In brief, IC (inhibitory concentration) scores were determined using serial dilutions with log phase yeast cultures in YPD (2% glucose, 2% BactoPeptone, 1% yeast extract) in 96-well plates (starting OD_{600} 0.05, 120 μl/well) at 30°C, 770 rpm for 16 h. IC_{10}, IC_{20}, IC_{30}, IC_{40}, and IC_{50} concentrations were determined for all compounds. The HIP assays were performed in 24-well plates (1,600 μl/well YPD) at IC_{30} concentrations in duplicate. YPD/compound filled wells were inoculated with ~ 250 yeast cells/strain (1.5 OD_{600}/ml o/n culture), plates were incubated for 16 h at 30°C, 550 rpm for 5 doublings each, for a total of 20 generations. Similarly, for HOP assays, cultures were incubated with the compounds and 5 doublings were monitored (no further dilutions). For each HIP/HOP experiment, growth curves were recorded and analyzed. gDNA isolation, TAG PCR amplification, GenFlex Tag16K v2 hybridization, and data analysis have been described previously (Hoepfner *et al*, 2014).

Yeast growth rates

Growth assessments and MIC determinations were performed by filling plates with YPD (2% glucose, 2% BactoPeptone, 1% yeast extract) or YPEG (2% glycerol, 1% ethanol, 2% BactoPeptone, 1% yeast extract) and solidified using 2% agar. Compounds were diluted in DMSO and added on top of the plates, and DMSO concentrations were kept constant at 2%.

Mitotracker experiments

LN229 cells were seeded in 8-chamber slides (chambered coverslip with 8 wells, ibidi GmbH) at a density of 3×10^4 cells per ml in 300 μl Dulbecco's Modified Eagle's Medium with 10% FBS per well. The chamber slide was incubated under normal conditions (37°C and 5% CO2). After 24 h, cells were exposed to DHA and/or 5-ALA for a period of 24 h. Then, medium was aspirated, and 300 μl of medium without FBS and phenol red were added, as well as 50 nM of Mitotracker (Mitotracker red, CMXRos, M7512 Invitrogen, Thermo Fisher Scientific) for 30 min. Slides were fixed with 4% PFA for 20 min at room temperature, washed with 1xPBS, and covered with Vectashield (Vectashield with DAPI, Vector Laboratories Inc.). Slides were kept at 4°C and then cells were imaged on a laser scanning microscope (Carl Zeiss), with a 63× oil immersion objective and using the respective image software (Zen2010, Carl Zeiss). Signals were detected using 405 and 555 nm solid state laser lines and 555 nm short pass (DAPI) and 549 nm long pass (A549) emission filters, respectively.

Mitochondrial staining

MitoTracker staining (Cat. No. M7514, ThermoFisher Scientific) was performed according to the manufacturer's protocol and imaged on an Axiovert 200M with standard FITC filter sets, through a 100×/1.3 Ph3 objective (Carl Zeiss, Oberkochen, Germany) using a X-Cite120 (Excelitas, Waltham, Massachusetts, USA) illumination light source.

Mammalian cell lines

Mouse AN3-12 ESC lines were generated in our laboratory and characterized and authenticated as previously described (Elling *et al*, 2011). Haploid murine ESCs were used for insertional mutagenesis and derivation of gene trap knockout cell lines. AN3-12 cells (Elling *et al*, 2011) were cultured in DMEM supplemented with 15% fetal bovine serum (FCS), penicillin–streptomycin, nonessential amino acids (NEAA), sodium pyruvate (1 mM), l-glutamine (2 mM), β-mercaptoethanol (0.1 mM), and LIF (20 μg/ml). SH-SY5Y were obtained directly from the supplier (Sigma Aldrich) and used for growth assays and cellular stainings. SH-SY5Y cells were cultured in DMEM/F12 1:1 supplemented with 10% FCS (fetal calf serum), penicillin–streptomycin, and L-glutamine. 4T1 cells were cultured in IMDM supplemented with 10% fetal calf serum (FCS), penicillin–streptomycin and L-glutamine. Jurkat T cells were used in *in vitro* viability and DHE assays; the cells were obtained from an in-house source and are functionally described elsewhere (Reikerstorfer *et al*, 1995). Mcf7, MDA-MB-231, 4T1, Panc1, and B16F10 cancer cell lines were obtained in house. MEFs (mouse embryonic fibroblasts) were generated and obtained in house. PlatE cells were used for recombinant retrovirus and lentivirus production as previously described (Stadlmann *et al*, 2017; Taubenschmid *et al*, 2017). MEFs, Mcf7, MDA-MB-231, Panc1, and B16F10 and PlatE cells were cultured in DMEM supplemented with 10% FCS, penicillin–streptomycin and L-glutamine. Cells were cultured at 37°C, with

20% O_2 and 5% CO_2. All cell lines tested were negative for mycoplasma. No cell lines listed by ICLAC were used.

Competitive growth assays

Haploid ESCs (Elling *et al*, 2011) harboring gene traps in genomic introns were seeded at low density in normal ESC growth medium and infected for 12 h with two viruses, one encoding mCherry plus Cre recombinase and the other coding for GFP, both expressing puromycin (Invivogen, ant-pr-1). Infected cells were selected (final concentration of puromycin, 1 μg/ml) after 24 h and expanded. Ratios of GFP- to mCherry/Cre-expressing cells in the presence and absence of dihydroartemisinin were determined using high-throughput flow cytometry (BD LSRFortessa HTS Cell Analyzer).

Compound profiling in cell lines

The following compounds were used: Dihydroartemisinin (dihydroqinghaosu, artenimol, DHA) was a kind gift from Dominic Hoepfner (Novartis); Delta-aminolaevulinic acid hydrochloride, 5-ALA (Sigma Aldrich A3785-500MG); acifluorfen, protoporphyrinogen oxidase (Ppox) inhibitor (Sigma Aldrich N11027-250MG); piperlongumine, induces ROS (Sigma Aldrich SML0221-5MG). For dosage responses, cells were seeded in 96-wells (25,000/96-well, in triplicate—where indicated) and subjected to compounds for 48 h (or 72 h if indicated in the Figure). Cell viability was assessed using automated cell counting (high-throughput flow cytometry), Alamar Blue staining (Invitrogen, DAL1100) or CellTiter-Glo Luminescent Assay (Promega, G7570, according to the manufacturer's protocol), respectively. For the detection of ROS, treated cells were collected, washed with 1x HBSS (without Ca^{2+} and Mg^{2+}), incubated with 1 mM DHE (dihydroethidium (hydroethidine), Invitrogen, D11347) in 1× HBSS for 45 min at 37°C, washed twice and counterstained with DAPI or a viability dye (eBioscience™ Fixable Viability Dye eFluor™ 780, 65-0865-18) for 10 min on ice. Cells were then collected, strained, and analyzed using flow cytometry for DHE in the red fluorescent spectrum (PE channel 582/15 nm). For JC-1 staining, treated cells were collected, washed with 1xPBS, incubated with 2 μM JC-1 in 1xPBS (MitoProbe JC-1 Assay Kit-1, Invitrogen, M34152) for 35 min at 37°C, washed twice, and analyzed using flow cytometry in the red (PE channel) and green (FITC channel) fluorescence spectrum.

Cerebral organoids

Cerebral organoids were generated as described (Lancaster *et al*, 2013). Human ESCs (feeder-free H9, WiCell) were transferred into low-attachment 96-well-plates (Corning) in a density of 9,000 cells per well and incubated in human stem cell medium. After 6 days, the medium was changed to neural induction media, containing Dulbecco's modified eagle medium DMEM/F12, N2 supplement (Invitrogen), Glutamax (Invitrogen), minimum essential media-nonessential amino acids (MEM-NEAA), and 1 μg/ml heparin (Sigma), to promote growth of ectodermal tissue. On day 11, embryonic bodies (EBs) were embedded in droplets of Matrigel and transferred to differentiation medium, containing DMEM/F12: Neurobasal 1:1, N2 supplement (Invitrogen), B27 supplement (without vitamin A) (Invitrogen), 50 μM 2-mercaptoethanol, 1:4,000 insulin (Sigma), Glutamax (Invitrogen), penicillin–streptomycin, MEM-NEAA onto 10 cm plates. Five days later, organoids were transferred to an orbital shaker and maintained in differentiation media containing vitamin A (in B27 supplement). Human cells were tested negative for mycoplasma.

Cerebral tumor organoid formation

Tumor initiation was induced by either oncogene amplification, using a Sleeping Beauty (SB) transposase, or mutation of tumor suppressor genes, using the CRISPR-Cas9 system in day 10 old embryoid bodies (EBs). Plasmids carrying the transposase as well as GFP and the desired oncogenes or expressing Cas9 nuclease were introduced by electroporation. In brief, a mixture of 1 μg DNA and 100 μl nucleofector solution was added to 10 EBs and transferred to a nucleofection cuvette. The Lonza Nucleofector 2b and the A-023 program were used for nucleofection. Thereafter, EBs were transferred into 10 cm dishes comprising of differentiation media plus vitamin A and embedded into Matrigel 24 h later. Two different types of tumors were initiated (Bian *et al*, 2018): Central nervous system primitive neuroectodermal tumors (CNS-PNET-like) were induced by the overexpression of c-MYC. Glioblastoma-like tumor group 2 (GBM-2) was modeled by mutagenesis of the tumor suppressor genes p53, NF1, and PTEN. All plasmids were designed by Shan Bian at IMBA (Bian *et al*, 2018).

Compound profiling in cerebral tumor organoids

Cerebral tumor organoids were treated with different doses of dihydroartemisinin and 5-ALA, and the survival and growth of transformed and untransformed neurons were monitored. Fluorescence labeling of tumor cells allowed us to distinguish transformed GFP^+ cells from nontransformed cells in the same organoid throughout the time of experiment using brightfield microscopy combined with fluorescence imaging. At the endpoint of the treatment (d5 or d7), cerebral (tumor) organoids were enzymatically and mechanically dissociated using 1× trypsin, 35–45 min incubation at 37°C, and gentle shaking. Organoid cells were singularized by careful resuspension, addition of differentiation medium and straining (Falcon Round-Bottom Tubes with Cell Strainer Cap, 5 mL, 35 μm nylon mesh cell strainer snap cap). Single cells in suspension were counterstained with DAPI or the viability dye (eBioscience™ Fixable Viability Dye eFluor™ 780, 65-0865-18), and the amounts of GFP-positive cells were analyzed by flow cytometry (BD LSRFortessa HTS Cell Analyzer). 5-ALA- or dihydroartemisinin-treated cerebral organoids were imaged at the indicated time points using the Axio Vert.A1 Inverted Microscope system (Zeiss Objective EC Plan-Neofluar 2.5×/0.085 Pol M27, 0.5 camera adapter). Brightfield and green fluorescence images were taken from the same area. Additionally, for image analyses, the Celldiscoverer 7 (Zeiss), a fully integrated high-end automated live cell imaging system, was used.

Immunohistochemistry staining

Cerebral organoids were fixed in 4% PFA (room temperature, 1 h), incubated with 30% sucrose (4°C, o/n), OCT (Tissue-tek OCT Compound, SANOVA PHARMA GESMBH, 4583) embedded and 20 μm sections were cryostat cut (−12/−14°C). For staining, sections were blocked and permeabilized for 1 h on RT in 0.25%

Triton X-100, 4% donkey serum in PBS, stained with primary antibodies diluted in 0.1% Triton X-100, 4% donkey serum in PBS at RT overnight, incubated with secondary antibodies diluted in 0.1% Triton X-100, 4% donkey serum in PBS for 2 h at RT, and finally counterstained with DAPI (4′,6-diamidino-2-phenylindole, Dilactate, Invitrogen, D3571) at RT for 20 min. Fluorescence Mounting Medium (Dako, S302380) was used for mounting the sample slides. The following antibodies were used: anti-GFP antibody (Abcam, ab13970, 1:500), anti-Ki-67 monoclonal antibody (SolA15, eBioscience, 14-5698-82, 1:100), anti-cleaved caspase-3 antibody (Asp175, Cell Signaling Technology, 966S1, 1:300), anti-Sox2 antibody (R&D Systems, AF2018; or Abcam, ab97959, 1:1000), anti-Map2 antibody (Millipore, MAB3418, 1:500), and anti-gamma-H2A.X antibody (phospho S139, Abcam, ab11174, 1:300). The organoids were imaged on an LSM780 Axio Imager (point laser scanning confocal microscope, GaAsP (gallium arsenide) detectors with QE of 45% and up to 2× SNR) with a standard filter set (CH1: 371–735, CH2: 479–735, CH3 Quasar (GaAsP): 416–690) through a 20×/0.8 plan-Apochromat objective (Carl Zeiss) using laser illumination (laser diode 405—25 mW, argon 458, 488, 514—30 mW, DPSS 561—15 mW, HeNe 633—5 mW).

Patient-derived brain tumor models

The patient-derived brain tumor models VBT12, VBT92, VBT281, VBT293, VBT529, and VBT531 were established at the Medical University of Vienna, Austria, and the models BTL53, BTL90, and BTL1333 at the Johannes Kepler University Hospital, Linz, Austria, as previously published (Gabler *et al*, 2019). The study was approved by the local ethics committee. Patient-derived tumor cells were cultivated in RPMI-1640 (R6504, Sigma-Aldrich) supplemented with 10% fetal bovine serum (FBS, 11403164, Thermo Fisher Scientific) and grown at 37°C and 5% CO_2. Neurospheres were cultured in low attachment plates in neurobasal media (NB^+, Neurobasal Media, Gibco, 21103-049, Thermo Fisher Scientific) supplemented with 1% B27 (50×, 175404-044, Thermo Fisher Scientific), 1% N2 (Neuro Mix 100×, 17502-048, Thermo Fisher Scientific), 20 ng/ml basic FGF (100-18B, PeproTech), 20 ng/ml EGF (E9644, Sigma-Aldrich), and 2 mM L-glutamine (Sigma Aldrich). Monitoring of cells and imaging was performed with a Zeiss Primo Vert light microscope (Carl Zeiss, Jena, Germany). All cell lines were tested negative for mycoplasma.

Cell viability assays

Cells were seeded in triplicates in 96-well plates (CytoOne® Starlab GmbH) at a density of 2.5 (VBT92) or 4 (VBT281) × 10^4 per ml of RPMI-1640 based culture media using 100 µl per well and, after 24 h of adherence, treated with the indicated doses of cisplatin (Sigma Aldrich, 232120-50MG), VP-16 or etoposide (Sigma Aldrich, E1383-25MG), or temozolomide (TMZ, Sigma Aldrich, T2577-100MG) for 72 h at 37°C, 5% CO2. The number of viable cells was determined using "CellTiter-Glo® Luminescent Cell Viability Assay" (Promega G7571) or MTT assay, according to the manufacturer's instructions (MTT/ EZ4U assay, Biomedica BI-5000).

For spheroid assays cells were seeded at a density of 1 × 10^4 cells per well in 500 µl neurobasal media (NB^+ with supplements, see above) in duplicates in ultralow attachment 24-well plates (Corning). Prior to drug exposure, in both settings, cells were left for 24 h under normal culture conditions. Next, the indicated concentrations of DHA and/or 5-ALA were added either in RPMI 1640 with 10% FBS or neurobasal media. Following drug exposure of 72 h, cell viability was assessed using "CellTiter-Glo® Luminescent Cell Viability Assay" (Promega G7571) according to manufacturer's protocols. Luminescence was measured at 1000 nm at the Tecan infinite 200Pro (Zurich, Switzerland). Raw data were analyzed using GraphPad Prism software 8.0.1 (GraphPad Software). Results are given as mean ± standard deviation (SD) and were normalized to untreated control cells.

Re-adhesion capacity of patient-derived brain tumor spheroids

Cells were seeded at a density of 1 × 10^4 cells per well in 500 µl neurobasal media in duplicates in ultralow attachment 24-well plates at 37°C and 5% CO_2, 24 h prior to drug treatment. Following compound exposure for 72 h, cells were harvested (280 *g*, 5 min), resuspended in growth media (RPMI-1640, 10% FBS), and cultured in 24-well plates for 7 days to allow and follow attachment. Afterward, the medium was discarded, plates were dried upside-down overnight, and cells were fixed in ice-cold methanol for 15 min at 4°C before crystal violet staining. Images were taken using a Nikon D3200 camera and processed using ImageJ software (ImageJ Fiji). For quantification, crystal violet was eluted using 2% sodium dodecyl sulfate, and color absorbance was measured at 560 nm at the Tecan infinite 200Pro. Analysis was performed in quadruplicates. Values were analyzed using GraphPad Prism software 8.0.1 and are given as arbitrary units (AU) as mean ± SD normalized to untreated control.

Annexin V-PI staining

VBT281 glioblastoma cells were seeded in 6-well plates (CytoOne) for adherent cell experiments, or ultra-low attachment 6-well plates (Corning) for spheroid assays, at a cell density of 1 × 10^5 cells per ml of the respective cell culture media. R10 media (RPMI with 10% FBS) was used for adherent cells. NB^+ media (Neurobasal media with supplements) was used for spheroid cultures. After preplating for 24 h, cells were treated with DHA (dihydroartemisinin), 5-ALA, or the combination at the indicated concentrations.

The supernatant of adherent cells was combined with the trypsinized, singularized cells, washed with 1× PBS and filtered through a nylon mesh (size 60 µm, Sigma-Aldrich). Floating spheroids were collected, washed with 1× PBS, TrypL/E treated (Gibco TrypLE Express Enzyme (1×), phenol red 12605028, Thermo Fisher Scientific), singularized, washed again with 1× PBS and filtered. All samples were resuspended in 100 µl Annexin V Binding buffer each, and stained in FACS tubes with Propidium iodide (PI, 1 mg/ml, P4864 Sigma-Aldrich) and Annexin V-FITC (50 µg/ml, 556,420, BD Biosciences). After an incubation for 10–15 min at RT (protected from light), 200 µl of cold Annexin V Binding buffer was added and samples were measured on a flow cytometer (LSRFortessa flow cytometer, BD Biosciences). Data analysis was performed with FlowJo v10.06 (BD Biosciences) and GraphPad Prism 8.0.1.

NAC experiments

Cells were seeded in 96-well plates (CytoOne) at a density of 2.5–5 × 10^4 per ml in the respective cell culture media (RPMI with 10% FBS for adherent cells, Dulbecco's Modified Eagle's Medium with

10% FBS for LN229). After 24 h, cells were exposed to DHA and/or 5-ALA with or without 1 h preincubation with freshly prepared NAC (dissolved in cell culture media, R10; Sigma Aldrich A2750-10G). The ATP-based CellTiter-Glo Luminescent Cell Viability Assay (Promega, G7570) was used to measure viability according to manufacturer's instructions and luminescence was measured with the Tecan infinite 200Pro plate reader (Zurich, Switzerland). GraphPad Prism software (version 8.0.1) was used to determine the dose response curves and calculate the activity expressed as IC_{50} values. Results are given as means ± standard deviation (SD) and were normalized to untreated control cells. For clonogenic assays, cells were seeded in 24-well plates (CytoOne) at a density of 1–5 × 10^3 per well in 500 µl of the respective cell culture media (RPMI with 10% FBS for adherent cells, Dulbecco's Modified Eagle's Medium with 10% FBS for LN229). After 24 h, cells were exposed to the indicated drugs (DHA, 5-ALA) with or without 1 h preincubation with freshly prepared NAC (dissolved in cell culture media, R10, Sigma Aldrich A2750-10G). After 7 days cells were fixed with methanol, stained with crystal violet, and photographed with a macro lens on a Nikon D3200 camera (Minato). For quantification, crystal violet was eluted using 2% sodium dodecyl sulfate (SDS) and color absorbance was measured at 560 nm at the Tecan infinite 200Pro (Zurich, Switzerland). Values were analyzed using GraphPad Prism (version 8.0.1) and are given in arbitrary units (AU) as means ± SD normalized to the untreated control.

Lipid peroxidation (BODIPY 581/591 C11 staining)

Cells were seeded at 2.5 × 10^5 cells per ml of the respective cell culture media (RPMI with 10% FBS for adherent cells, Dulbecco's Modified Eagle's Medium with 10% FBS for LN229) in 6-well plates (CytoOne). The next day, cells were exposed to DHA and/ or 5-ALA at the indicated concentrations. Hydrogen peroxide (H_2O_2 solution, 30% [w/w] in H_2O, H1009, Sigma-Aldrich) was used as a positive control. After 24 h, 1 µM of the lipid peroxidation sensor BODIPY 581/591 C11 (Thermo Fisher Scientific, D3861) was added to the cells for 30 min. Afterward, three washing steps with 1x PBS were performed. Cells were then trypsinized, resuspended in cell culture media without FBS, and subjected to flow cytometry using b610/20 (Red) and b530/30 (FITC) channels. Autofluorescence of cells was subtracted from measured values, and fluorescence shifts from red (590 nm) to green (510 nm) were assessed as an indication of oxidation. Data analysis was performed with FlowJo v10.06 and GraphPad Prism 8.0.1.

Animal experiments

All mice were bred, maintained, examined, and euthanized in accordance with institutional animal care guidelines and ethical animal license protocols approved by the legal authorities. Experimental animals were purchased from Charles River and housed at the Institute of Molecular Biotechnology (IMBA, Vienna, Austria), in a 12-h light/dark cycle, with food and water *ad libitum*. Only female *Crl:NU*(*NCr*)-*Foxn1nu* (Nude) mice group housed in individually ventilated cages were used for all experiments described. Animals were randomly assigned to experimental groups and checked daily by veterinary staff. Exclusion criteria for all assays were specified *a priori*; however, no animal was excluded. Experiments were performed in accordance with the ARRIVE guidelines. All animal experiments were approved by the Austrian Federal Ministry of Education, Science and Research (BMWFW-66.015/0021-WF/3b/2014) and conducted according to project license GZ 2020–0.762.422 and their amendments.

The paper explained

Problem
The natural compound Artemisinin is some of the most widely used drugs against Malaria worldwide. Artemisinins are so-called endoperoxides that damage proteins in cells and can thus act as toxins. These cytotoxic properties have not only been recognized to treat malaria but also for their anticancer properties. However, the exact mechanism of action of Artemisinins has only been poorly characterized.

Results
We used genome-wide screens in yeast and haploid ESCs and found that a single pathway, namely mitochondrial heme production (also known as porphyrin biosynthesis), is accountable for Artemisinin's cytotoxicity in eukaryotic cells. We find that modulation of heme production is sufficient to increase or decrease Artemisinin's cytotoxicity in different cell types, including human cancer cells. We further tested the small molecule 5-ALA, an enhancer of heme production, that is used in the clinic specifically to mark brain tumor cells during surgery, as it is metabolized specifically in cancer cells but not in surrounding tissue. We used a variety of different *in vitro* and *in vivo* in mouse and human model systems of brain cancer development and showed that 5-ALA specifically sensitizes brain tumor cells to Artemisinins' cytotoxicity, without affecting normal tissue growth. We thus find that heme biosynthesis is the most critical molecular pathway for Artemisinin cytotoxicity in eukaryotic cells and could potentially be used for antibrain cancer therapy in combination with the heme enhancer 5-ALA.

Impact
We combined an unbiased screening approach and several clinically relevant brain cancer model systems to suggest a novel translational sensitization strategy for human glioblastoma. We envisage to use a clinically approved small molecule together with one of the most widely used antimalarial compounds, Artemisinin, to treat highly malignant brain tumors, such as human glioblastomas, in human patient therapy.

Patient material

Patients with malignant brain tumors and/or their legal representatives treated at the Medical University of Vienna gave preoperative informed consent to participate in the study in all cases. The study was approved by the local institutional review board (IRB) of the Medical University of Vienna (EK Nr. 1244/2016, EK Nr: 1616/2020) according to the guidelines of the Helsinki Declaration developed by the World Medical Association and the Department of Health and Human Services Belmont Report.

Glioblastoma PDX models

VBT529 or VBT531 glioblastoma cells were transduced with a Luc2-iRFP lentiviral vector. Following FACS sorting, 1.5–2 × 10^5 LUC2 expressing cells were injected into the brain or flank and brain of *Crl:NU*(*NCr*)-*Foxn1nu* (Nude) mice. For orthotopic PDX, mice were

anesthetized and restrained in a stereotaxic frame. The body temperature was monitored with a rectal thermometer and kept constant at 36°C by a heating pad. The skull was exposed, cleaned, and a small hole was drilled. Cells were injected at coordinates: AP-1, ML-2, DV-3. To prevent backflow, the needle was left at the injection site for 6 min after the injection was finished. Mice were left to recover for at least 1 week after the surgery and during that time their drinking water was supplied with Baytril (Bayer) and Rimadyl (Pfizer). Tumor growth was monitored using the IVIS imaging system. Artesunate (ARS, A3731-100MG, 88495-63-0 300 mg, Sigma) and 5-ALA (5-aminolevulinic acid hydrochloride, HY-N0305, 5451-09-2 MedchemExpress) were administered intraperitoneally (IP) at the concentrations and timepoints indicated in the figure legends. 5-ALA was dissolved in water, and ARS was dissolved in 5% $NaHCO_3$ (144-55-8, 8551.1, Roth) in 0.9% NaCl (7647-14-5, 3570130, B. Braun). Compounds were not mixed prior to injection, and 5-ALA and ARS were injected right after each other. For the comparisons between artesunate, 5-ALA and artesunate + 5-ALA, mice were 11 weeks old at the start of the experiment (surgery). For the comparison between artesunate and artesunate + 5-ALA, mice were 24 weeks old at the start of the experiment (surgery).

Metabolomics

Mice were treated with 120 mg/kg 5-ALA via intraperitoneal injection 1 h prior to sacrifice. Brain and tumor samples were snap-frozen in liquid nitrogen and homogenized in ice cold methanol:acetonitrile:water (2:2:1, v/v/v). Metabolite extracts were analyzed by reversed phase chromatography directly coupled to mass spectrometry (LC–MS/MS). For each sample, 1 µl was injected onto a Kinetex (Phenomenex) C18 column (100 Å, 150 × 2.1 mm) connected with a respective guard column, employing a 3-min-long linear gradient from 3% A (1% acetonitrile, 0.1% formic acid in water) to 95% B (0.1% formic acid in acetonitrile) at a flow rate of 80 µl/min, followed by isocratic elution for 25 min. Detection and quantification were done by selected reaction monitoring (SRM), employing a TSQ Altis mass spectrometer (Thermo Fisher Scientific) and using the following transitions in the positive ion mode: 210–122 m/z (porphobilinogen), 211–163 m/z, 563–504 m/z (protoporphyrin IX). Data interpretation was performed using Xcalibur (Thermo Fisher Scientific). Authentic standards were used for determining the optimal collision energies and for the confirmation of experimental retention times via standards added to the control sample.

Statistics and reproducibility

All values are given as means ± SD, unless stated otherwise. Box and whisker plots depict the median and ranges from the first to the third quartile. All experiments were reproduced at two to seven independent times, with similar results. GraphPad Prism was used to generate figures and perform statistical analyses (GraphPad Software). An *a priori* sample size estimation was not performed. The experiments were not randomized. The investigators were not blinded to allocation during experiments and outcome assessment. Data were analyzed by using the unpaired two-tailed Student's t-test, as indicated. $P < 0.05$ was accepted as statistically significant.

Data availability

This study includes no data deposited in external repositories.

Expanded View for this article is available online.

Acknowledgements

We would like to thank all members of our laboratories for critical comments and helpful discussions, as well as Thomas Lendl (IMBA/IMP BioOptics) for help with the image analysis. We thank Ralph Rield, Thomas Aust, and Sven Schuierer for execution and processing of the HIP-HOP assay. Orthotopic PDX surgeries were performed in collaboration with the Preclinical Phenotyping Facility at Vienna BioCenter Core Facilities (VBCF), member of the Vienna BioCenter (VBC), Austria. LC–MS/MS analysis was performed by the Metabolomics Facility at Vienna BioCenter Core Facilities (VBCF), funded by the Austrian Federal Ministry of Education, Science & Research and the City of Vienna. Work in JMP's laboratory is supported by the Austrian Federal Ministry of Education, Science and Research, the Austrian Academy of Sciences, the City of Vienna and grants from the European Research Council (ERC Advanced grant 341036), the Austrian Science Fund (FWF Wittgenstein award Z 271-B19), the T. von Zastrow foundation, and a Canada 150 Research Chairs Program (F18-01336). Work in JAK's laboratory is supported by the Austrian Federal Ministry of Education, Science and Research, the Austrian Academy of Sciences, the City of Vienna, and the SFB F78 Stem Cell (F 7803-B). This project has received funding from the European Research Council (ERC) under the European Union's Horizon 2020 research and innovation (695642), as well as from FFG (early stage; project number 879800). The work was further supported by ERA-NET TRANSCAN-2 JTC 2017 consortium "BRCAddict" (Austrian Science Fund #I 4164, to J.G.), the Verein unser_kind," and the "Fellinger Krebsforschung." GW received travel support from NX Development Corp (NXDC), which distributes 5-ALA for fluorescence-guided surgery of high-grade gliomas. WB was supported by the Austrian Science Fund FWF, project number: P30105.

Author contributions

Jasmin Taubenschmid-Stowers: Conceptualization; formal analysis; investigation; visualization; methodology; writing—original draft; writing—review and editing. **Michael Orthofer:** Formal analysis; investigation; visualization; methodology; writing—review and editing. **Anna Laemmerer:** Formal analysis; investigation; visualization; methodology; writing—review and editing. **Christian Krauditsch:** Investigation; methodology; writing—review and editing. **Marianna Rózsová:** Investigation. **Christian Studer:** Investigation. **Daniela Lötsch:** Formal analysis; investigation; visualization; methodology; writing—review and editing. **Johannes Gojo:** Investigation; methodology; writing—review and editing. **Lisa Gabler:** Investigation. **Matheus Dyczynski:** Investigation. **Thomas Efferth:** Investigation. **Astrid Hagelkruys:** Project administration. **Georg Widhalm:** Resources; funding acquisition; investigation. **Andreas Peyrl:** Resources; investigation. **Sabine Spiegl-Kreinecker:** Resources. **Dominic Hoepfner:** Formal analysis; investigation; visualization; methodology; writing—review and editing. **Shan Bian:** Resources; methodology. **Moritz Horn:** Resources; investigation; project administration; writing—review and editing. **Walter Berger:** Resources; supervision; funding acquisition; investigation; methodology; writing—review and editing. **Juergen A Knoblich:** Resources; funding acquisition; methodology. **Ulrich Elling:** Conceptualization; formal analysis; methodology. **Josef M Penninger:** Conceptualization; resources; supervision; funding acquisition; writing—review and editing.

Disclosure and competing interests statement

JMP is founder shareholder and supervisory board member of JLP Health. UE and MH are shareholders of JLP Health. MO, MR, and MD are employees of JLP Health. JLP Health develops a combinatorial cancer therapy based on 5-ALA and artesunate.

References

Antoine T, Fisher N, Amewu R, O'Neill PM, Ward SA, Biagini GA (2014) Rapid kill of malaria parasites by artemisinin and semi-synthetic endoperoxides involves ROS-dependent depolarization of the membrane potential. *J Antimicrob Chemother* 69: 1005 – 1016

Arlt H, Tauer R, Feldmann H, Neupert W, Langer T (1996) The YTA10-12 complex, an AAA protease with chaperone-like activity in the inner membrane of mitochondria. *Cell* 85: 875 – 885

Aweeka FT, German PI (2008) Clinical pharmacology of Artemisinin-based combination therapies. *Clin Pharmacokinet* 47: 91 – 102

Batlle AM (1993) Porphyrins, porphyrias, cancer and photodynamic therapy–a model for carcinogenesis. *J Photochem Photobiol B Biol* 20: 5 – 22

Bessone F, Poles N, Roma MG (2014) Challenge of liver disease in systemic lupus erythematosus: clues for diagnosis and hints for pathogenesis. *World J Hepatol* 6: 394 – 409

Bi WL, Beroukhim R (2014) Beating the odds: extreme long-term survival with glioblastoma. *Neuro Oncol* 16: 1159 – 1160

Bian S, Repic M, Guo Z, Kavirayani A, Burkard T, Bagley JA, Krauditsch C, Knoblich JA (2018) Genetically engineered cerebral organoids model brain tumor formation. *Nat Methods* 15: 631 – 639

Bosman A, Mendis KN (2007) A major transition in malaria treatment: the adoption and deployment of artemisinin-based combination therapies. *Am J Trop Med Hyg* 77: 193 – 197

Cadet J, Wagner JR (2013) DNA base damage by reactive oxygen species, oxidizing agents, and UV radiation. *Cold Spring Harb Perspect Biol* 5: a012559

Chacinska A, Pfannschmidt S, Wiedemann N, Kozjak V, Sanjuán Szklarz LK, Schulze-Specking A, Truscott KN, Guiard B, Meisinger C, Pfanner N (2004) Essential role of Mia40 in import and assembly of mitochondrial intermembrane space proteins. *EMBO J* 23: 3735 – 3746

Craven RJ, Mallory JC, Hand RA (2007) Regulation of iron homeostasis mediated by the heme-binding protein Dap1 (damage resistance protein 1) via the P450 protein Erg11/Cyp51. *J Biol Chem* 282: 36543 – 36551

De Vleeschouwer S, Fernandes C, Costa A, Osório L, Lago RC, Linhares P, Carvalho B, Caeiro C (2017) Current standards of care in glioblastoma therapy. *Glioblastoma* 31: 197 – 241

Dunn CD, Lee MS, Spencer FA, Jensen RE (2006) A genomewide screen for petite-negative yeast strains yields a new subunit of the i-AAA protease complex. *Mol Biol Cell* 17: 213 – 226

Efferth T (2017) From ancient herb to modern drug: artemisia annua and artemisinin for cancer therapy. *Semin Cancer Biol* 46: 65 – 83

Elling U, Taubenschmid J, Wirnsberger G, O'Malley R, Demers SP, Vanhaelen Q, Shukalyuk AI, Schmauss G, Schramek D, Schnuetgen F *et al* (2011) Forward and reverse genetics through derivation of haploid mouse embryonic stem cells. *Cell Stem Cell* 9: 563 – 574

Gabler L, Lötsch D, Kirchhofer D, van Schoonhoven S, Schmidt HM, Mayr L, Pirker C, Neumayer K, Dinhof C, Kastler L *et al* (2019) TERT expression is susceptible to BRAF and ETS-factor inhibition in BRAFV600E/TERT promoter double-mutated glioma. *Acta Neuropathol Commun* 7: 128 – 116

Giaever G, Shoemaker DD, Jones TW, Liang H, Winzeler EA, Astromoff A, Davis RW (1999) Genomic profiling of drug sensitivities via induced haploinsufficiency. *Nat Genet* 21: 278 – 283

Golenser J, Waknine JH, Krugliak M, Hunt NH, Grau GE (2006) Current perspectives on the mechanism of action of artemisinins. *Int J Parasitol* 36: 1427 – 1441

Guyotat J, Pallud J, Armoiry X, Pavlov V, Metellus P (2016) 5-Aminolevulinic acid-Protoporphyrin IX fluorescence-guided surgery of high-grade gliomas: a systematic review. *Adv Tech Stand Neurosurg* https://doi.org/10.1007/978-3-319-21359-0_3

Hadjipanayis CG, Widhalm G, Stummer W (2015) What is the surgical benefit of utilizing 5-Aminolevulinic acid for fluorescence-guided surgery of malignant gliomas? *Neurosurgery* 77: 663 – 673

Haynes RK, Cheu K-W, N'Da D, Coghi P, Monti D (2013) Considerations on the mechanism of action of artemisinin antimalarials: part 1–the 'carbon radical' and 'heme' hypotheses. *Infect Disord Drug Targets* 13: 217 – 277

Hoepfner D, Helliwell SB, Sadlish H, Schuierer S, Filipuzzi I, Brachat S, Bhullar B, Plikat U, Abraham Y, Altorfer M *et al* (2014) High-resolution chemical dissection of a model eukaryote reveals targets, pathways and gene functions. *Microbiol Res* 169: 107 – 120

Ismail HM, Barton V, Phanchana M, Charoensutthivarakul S, Wong MHL, Hemingway J, Biagini GA, O'Neill PM, Ward SA (2016) Artemisinin activity-based probes identify multiple molecular targets within the asexual stage of the malaria parasites plasmodium falciparum3D7. *Proc Natl Acad Sci USA* 113: 2080 – 2085

Jacob F, Salinas RD, Zhang DY, Nguyen PTT, Schnoll JG, Wong SZH, Thokala R, Sheikh S, Saxena D, Prokop S *et al* (2020) A patient-derived glioblastoma organoid model and biobank recapitulates inter- and intra-tumoral heterogeneity. *Cell* 180: 188 – 204.e122

Klayman DL (1985) Qinghaosu (artemisinin): an antimalarial drug from China. *Science* 228: 1049 – 1055

Krishna S, Bustamante L, Haynes RK, Staines HM (2008) Artemisinins: their growing importance in medicine. *Trends Pharmacol Sci* 29: 520 – 527

Lancaster MA, Renner M, Martin C-A, Wenzel D, Bicknell LS, Hurles ME, Homfray T, Penninger JM, Jackson AP, Knoblich JA (2013) Cerebral organoids model human brain development and microcephaly. *Nature* 501: 373 – 379

Matringe M, Camadro JM, Labbe P, Scalla R (1989) Protoporphyrinogen oxidase as a molecular target for diphenyl ether herbicides. *Biochem J* 260: 231 – 235

Mbengue A, Bhattacharjee S, Pandharkar T, Liu H, Estiu G, Stahelin RV, Rizk SS, Njimoh DL, Ryan Y, Chotivanich K *et al* (2015) A molecular mechanism of artemisinin resistance in plasmodium falciparum malaria. *Nature* 520: 683 – 687

Meshnick SR, Taylor TE, Kamchonwongpaisan S (1996) Artemisinin and the antimalarial endoperoxides: from herbal remedy to targeted chemotherapy. *Microbiol Rev* 60: 301 – 315

Morales MJ, Dang YL, Lou YC, Sulo P, Martin NC (1992) A 105-kDa protein is required for yeast mitochondrial RNase P activity. *Proc Natl Acad Sci USA* 89: 9875 – 9879

Navaratnam V, Mansor SM, Sit NW, Grace J, Li Q, Olliaro P (2000) Pharmacokinetics of artemisinin-type compounds. *Clin Pharmacokinet* 39: 255 – 270

Navone NM, Polo CF, Frisardi AL, Andrade NE, Battle AM (1990) Heme biosynthesis in human breast cancer—mimetic "*in vitro*" studies and some heme enzymic activity levels. *Int J Biochem* 22: 1407 – 1411

Nunnari J, Walter P (1996) Regulation of organelle biogenesis. *Cell* 84: 389 – 394

Ostrom QT, Gittleman H, Xu J, Kromer C, Wolinsky Y, Kruchko C, Barnholtz-Sloan JS (2016) CBTRUS statistical report: primary brain and other central nervous system tumors diagnosed in the United States in 2009–2013. *Neuro Oncol* 18: v1 – v75

Parasramka S, Talari G, Rosenfeld M, Guo J, Villano JL (2017) Procarbazine, lomustine and vincristine for recurrent high-grade glioma. *Cochrane Database Syst Rev* 7: CD011773

Pierce SE, Fung EL, Jaramillo DF, Chu AM, Davis RW, Nislow C, Giaever G (2006) A unique and universal molecular barcode array. *Nat Methods* 3: 601 – 603

Reikerstorfer A, Holz H, Stunnenberg HG, Busslinger M (1995) Low affinity binding of interleukin-1 beta and intracellular signaling via NF-kappa B identify Fit-1 as a distant member of the interleukin-1 receptor family. *J Biol Chem* 270: 17645 – 17648

Roemer T, Davies J, Giaever G, Nislow C (2011a) Bugs, drugs and chemical genomics. *Nat Chem Biol* 8: 46 – 56

Roemer T, Xu D, Singh SB, Parish CA, Harris G, Wang H, Davies JE, Bills GF (2011b) Confronting the challenges of natural product-based antifungal discovery. *Chem Biol* 18: 148 – 164

Schnütgen F, Hansen J, De-Zolt S, Horn C, Lutz M, Floss T, Wurst W, Noppinger PR, von Melchner H (2008) Enhanced gene trapping in mouse embryonic stem cells. *Nucleic Acids Res* 36: e133

Stadlmann J, Taubenschmid J, Wenzel D, Gattinger A, Durnberger G, Dusberger F, Elling U, Mach L, Mechtler K, Penninger JM (2017) Comparative glycoproteomics of stem cells identifies new players in ricin toxicity. *Nature* 549: 538 – 542

Straimer J, Gnadig NF, Witkowski B, Amaratunga C, Duru V, Ramadani AP, Dacheux M, Khim N, Zhang L, Lam S *et al* (2015) K13-propeller mutations confer artemisinin resistance in *Plasmodium falciparum* clinical isolates. *Science* 347: 428 – 431

Stummer W, Stocker S, Wagner S, Stepp H, Fritsch C, Goetz C, Goetz AE, Kiefmann R, Reulen HJ (1998) Intraoperative detection of malignant gliomas by 5-aminolevulinic acid-induced porphyrin fluorescence. *Neurosurgery* 42: 518 – 525; discussion 525–526

Taubenschmid J, Stadlmann J, Jost M, Klokk TI, Rillahan CD, Leibbrandt A, Mechtler K, Paulson JC, Jude J, Zuber J *et al* (2017) A vital sugar code for ricin toxicity. *Cell Res* 27: 1351 – 1364

Thorsness PE, White KH, Fox TD (1993) Inactivation of YME1, a member of the ftsH-SEC18-PAS1-CDC48 family of putative ATPase-encoding genes, causes increased escape of DNA from mitochondria in *Saccharomyces cerevisiae*. *Mol Cell Biol* 13: 5418 – 5426

Tilley L, Straimer J, Gnädig NF, Ralph SA, Fidock DA (2016) Artemisinin action and resistance in plasmodium falciparum. *Trends Parasitol* 32: 682 – 696

de Vries PJ, Dien TK (1996) Clinical pharmacology and therapeutic potential of artemisinin and its derivatives in the treatment of malaria. *Drugs* 52: 818 – 836

Wang J, Zhang J, Shi Y, Xu C, Zhang C, Wong YK, Lee YM, Krishna S, He Y, Lim TK *et al* (2017) Mechanistic investigation of the specific anticancer property of Artemisinin and its combination with Aminolevulinic acid for enhanced Anticolorectal cancer activity. *ACS Cent Sci* 3: 743 – 750

Witkowski DA, Halling BP (1989) Inhibition of plant protoporphyrinogen oxidase by the herbicide acifluorfen-methyl. *Plant Physiol* 90: 1239 – 1242

Young RM, Jamshidi A, Davis G, Sherman JH (2015) Current trends in the surgical management and treatment of adult glioblastoma. *Ann Transl Med* 3: 121

Zhang C-J, Chia WN, Loh CCY, Li Z, Lee YM, He Y, Yuan L-X, Lim TK, Liu M, Liew CX *et al* (2015) Haem-activated promiscuous targeting of artemisinin in plasmodium falciparum. *Nat Commun* 6: 1 – 11

Zhao S, Wu J, Wang C, Liu H, Dong X, Shi C, Shi C, Liu Y, Teng L, Han D *et al* (2013) Intraoperative fluorescence-guided resection of high-grade malignant gliomas using 5-aminolevulinic acid-induced porphyrins: a systematic review and meta-analysis of prospective studies. *PLoS One* 8: e63682

FEBS openbio

FEBS PRESS science publishing by scientists

RESEARCH ARTICLE

Nuclear endonuclease G controls cell proliferation in ovarian cancer

Ye Na Choi[1], Tae Woong Seo[1], Yui Taek Lee[1], Dar Heum Jeong[2] and Soon Ji Yoo[1]

1 Department of Biology, Kyung Hee University, Seoul, South Korea
2 Department of Life and Nanopharmaceutical Sciences, Kyung Hee University, Seoul, South Korea

Keywords
antioxidants; cell death; cell proliferation; endonuclease G (EndoG); ovarian cancer (OC); reactive oxygen species (ROS)

Correspondence
S. J. Yoo, Department of Biology, Kyung Hee University, 1, Hoegi-dong, Dondaemoon-gu, Seoul 02447, South Korea
Fax: +82 2 961 0244
Tel: +82 2 961 0978
E-mail: yoosoonji@khu.ac.kr

Ye Na Choi, Tae Woong Seo and Yui Taek Lee contributed equally to this article

(Received 26 August 2022, revised 22 December 2022, accepted 2 February 2023)

doi:10.1002/2211-5463.13572

Edited by Ivana Novak

Ovarian cancer is characterized by a high degree of genetic heterogeneity. Platinum-based chemotherapy and some gene-targeted therapies have shown limited treatment efficacy due to toxicity and recurrence, and thus, it is essential to identify additional therapeutic targets based on an understanding of the pathological mechanism. Here, we report that endonuclease G, which exhibits altered expression in ovarian cancer, does not function as a cell death effector that digests chromosomal DNA in ovarian cancer. Endonuclease G is modulated by intracellular reactive oxygen species dynamics and plays a role in cell proliferation in ovarian cancer, suggesting that targeting endonuclease G alone or in combination with other antitumor agents may have the potential for development into a treatment for endonuclease G-overexpressing cancers, including ovarian cancer.

Ovarian cancer (OC) is a common gynecologic malignancy. It is often diagnosed at an advanced stage due to a lack of symptoms in the early stage, and thus the 5-year survival rate is poor [1]. Platinum-based chemotherapy, which induces DNA instability, is the standard treatment for OC, and cisplatin is the most frequently used drug for OC treatment. However, the efficacy of cisplatin is limited due to the development of drug resistance [1,2]. Therefore, it is important to provide additional treatment options for OC patients, including those used in combination with platinum agents or single gene-targeted therapies. Genes associated with OC have been discovered, and targeted therapies have been developed for some genes [3–5].

Abbreviations
2-DG, 2-deoxy-D-glucose; BIR, baculoviral IAP repeat; CHIP, C-terminus of Hsc70-interacting protein; CHX, cycloheximide; cIAP1, cellular inhibitor of apoptosis protein; CPC, chromosome passenger complex; DAPI, diamidino-2-phenylindole; EndoG, endonuclease G; FBS, fetal bovine serum; GAPDH, glyceraldehyde 3-phosphate dehydrogenase; GEPIA, gene expression profiling interactive analysis; GFP, green fluorescent protein; H_2O_2, hydrogen peroxide; NAC, N-acetyl cysteine; PBS, phosphate-buffered saline; PI, propidium iodine; qRT-PCR, quantitative reverse-transcription polymerase chain reaction; ROS, reactive oxygen species.

FEBS Open Bio **13** (2023) 655–669

Bevacizumab targets the VEGF pathway, and PARP inhibitors such as olaparib can treat certain OC subtypes [4,5]. However, in addition to toxicity, disease relapse is quite common after primary chemotherapy [4–6]. OC patients have a particularly heterogenous genetic background [1]. Therefore, the identification of additional altered genes in OC and understanding their tumorigenic mechanism are essential to expanding treatment options.

Reactive oxygen species (ROS) are naturally generated in cells, mostly as by-products of metabolic processes. Various forms of ROS are eventually reduced to hydrogen peroxide (H_2O_2). Accumulation of ROS can cause oxidative stress, which is toxic to organisms, thus the antioxidant system must maintain low ROS levels under normal physiological conditions. However, the redox system, which controls intracellular ROS levels, is frequently dysregulated in cancers [7]. According to a study of OC patients, the ROS concentration was approximately 96% higher in malignant tissues compared to that in normal tissues [8], implying that high ROS levels might cause the proliferation and survival of OC cells. Indeed, antioxidants are used for OC therapy [9,10], but the underlying mechanism is not fully understood.

Endonuclease G (EndoG) is a cell death effector that causes DNA fragmentation during apoptosis [11,12]. EndoG is localized in mitochondria under normal conditions. EndoG is an evolutionary conserved DNA/RNA digesting nuclease [13] and target preference between DNA and RNA is changed depending on physiological ionic strength [14]. When apoptosis is triggered, EndoG is released from mitochondria and moves to the nucleus, destroying chromosomal DNA. Various types of cells are killed when nuclear EndoG translocates from the mitochondria during oxidative stress [15,16]. Interestingly, EndoG expression is induced by oxidative stress, including H_2O_2 treatment, as shown in our previous study [17]. Furthermore, elevated EndoG levels can sensitize cancer cells to chemotherapeutic drugs [18,19]. Regarding cancer cell death, studies have collectively suggested that increasing ROS levels might be a possible strategy to destroy cancer cells via nuclear EndoG activity because oxidative stress would induce EndoG expression and translocation to the nucleus [20,21]. However, in OC therapy, various types of antioxidants have been used to decrease intracellular ROS alone or in combination with other antitumor reagents [9,10]. This strategy conflicts with the classical apoptotic function of oxidative stress-induced EndoG, suggesting that EndoG might be differentially regulated by oxidative stress in OC.

Surprisingly, we found that EndoG is upregulated and localized in the nucleus in OC cell lines and patient tissues under normal conditions without additional apoptotic insult. We hypothesized that EndoG might not play an apoptotic role in OC. Therefore, we investigated whether EndoG might have a vital function in OC and whether it can be used as a therapeutic option alone and in combination with platinum-type agents for OC.

Results

EndoG does not function as a cell death effector upon oxidative stress in OC cells

Previously, we showed that EndoG is responsible for oxidative stress-induced cell death in HeLa cells and primary rat cortical neurons [17]. EndoG acts as a death effector and cleaves chromosomal DNA upon H_2O_2 treatment [11,12]. While exploring a novel function of EndoG in various cancer types, we noticed that EndoG might not be involved in cell death in OC cells. A water-soluble tetrazolium (WST) assay showed decreased cell viability of EndoG-depleted SKOV3 cells (an OC cell line) treated with siendoG and exposed to oxidative stress and increased viability in EndoG-depleted OSE80PC (control normal ovary cell line) and EndoG-depleted HeLa cells (Fig. 1A,B), consistent with our previous results [17]. The established stable cell line in this study, SKOV3 cells with EndoG-knockdown via shendoG (EndoG-KD cells), again showed decreased cell viability upon oxidative stress compared to control cells (shCTL cells) (Fig. 1C,D). If EndoG were a cell death effector upon oxidative stress in OC, EndoG-depleted cells would have shown increased cell viability. These results indicate that in OC cell lines, EndoG is not a cell death effector in response to oxidative stress and may have a nonapoptotic function.

Upregulated EndoG is localized in the nucleus in OC cells

We examined the EndoG levels in OC cells. EndoG levels were upregulated in all tested OC cell lines compared to normal ovary cells and were highest in SKOV3 cells (Fig. 2A, Fig. S1A). The *endoG* transcript was also upregulated in SKOV3 cells (Fig. 2B). The EndoG promoter is regulated via methylation of CpG by DNMT1, a DNA methyltransferase [19]. DNMT1 expression was decreased in SKOV3 cells compared to that in control cells (Fig. S1B), which might explain the upregulation of *endoG* mRNA in SKOV3 cells.

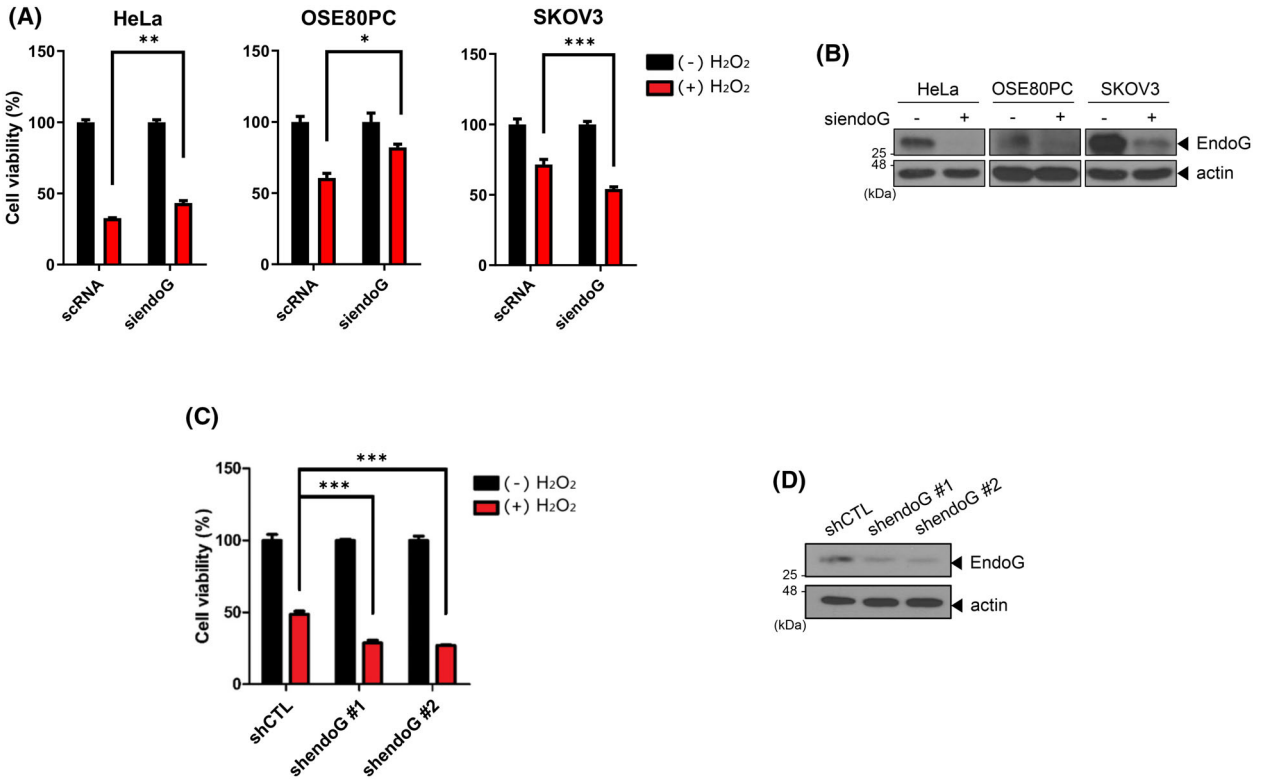

Fig. 1. EndoG does not function as a cell death effector under oxidative stress in OC cells. (A) HeLa, OSE80PC (normal ovary cell line), and SKOV3 (OC cell line) cells were transfected with scRNA or siendoG for 48 h and treated with 500 μM (OSE80PC, SKOV3) or 1 mM (HeLa) H_2O_2 for 4 h. The cell viability was analyzed with a WST assay. (B) The RNAi efficiency in (A) was evaluated by WB with anti-EndoG and antiactin antibodies. (C) EndoG-KD cells (shendoG) and control cells (shCTL) were treated with 500 μM H_2O_2 for 4 h. The cell viability was analyzed with a WST assay. (D) The EndoG levels in (C) were analyzed by WB. The means ± SEM are given for three independent experiments, ***$P < 0.001$, **$P < 0.01$, *$P < 0.05$, unpaired *t*-test (A, C).

Moreover, the half-life of EndoG was much longer in SKOV3 cells than that in control cells (Fig. 2C). Therefore, the upregulation of EndoG in SKOV3 cells is due to increases in both transcription and protein stability. We assessed *endoG* mRNA expression levels in OC patients by analyzing the Gene Expression Profiling Interactive Analysis (GEPIA) database and found that *endoG* was considerably increased compared to that in normal ovary tissues (Fig. 2D).

Next, we examined whether upregulated EndoG is localized in the mitochondria. Confocal images of cells immunostained with an anti-EndoG antibody showed more intense EndoG staining in SKOV3 cells than that in control normal cells (Fig. 2E). Surprisingly, we found that EndoG was localized in the nucleus and cytosol in SKOV3 cells, while in control cells, EndoG was observed in the cytosol, where it would normally be localized without an apoptotic stimulus (Fig. 2E). The statistical analysis revealed that the relative amount of nuclear EndoG was approximately 30% higher in SKOV3 cells than that in control cells (Fig. 2F). The subcellular fractionation results confirmed that EndoG was mainly localized in the nucleus in SKOV3 cells, unlike that in control cells (normal ovary cell line; Fig. 2G). Finally, to confirm our results in OC patient tissues, immunohistochemistry was conducted with an anti-EndoG antibody using ovary tissue microarray slides containing both normal and malignant tissues. EndoG staining was more intense in OC patient tissues than that in normal ovary tissues, and EndoG was observed throughout the whole cell, not only in the cytosol (Fig. 2H). Taken together, these results indicate that EndoG is upregulated in OC cells and patient tissues, and a considerable amount of EndoG is localized in the nucleus under normal conditions without apoptotic stress. EndoG is a cell death effector that is exclusively localized in the mitochondria and translocates to the nucleus after apoptotic stimulation, thus cleaving chromosomal DNA. Therefore, these results imply that nuclear-localized EndoG might have a different function from that in the mitochondria. This finding may explain why EndoG

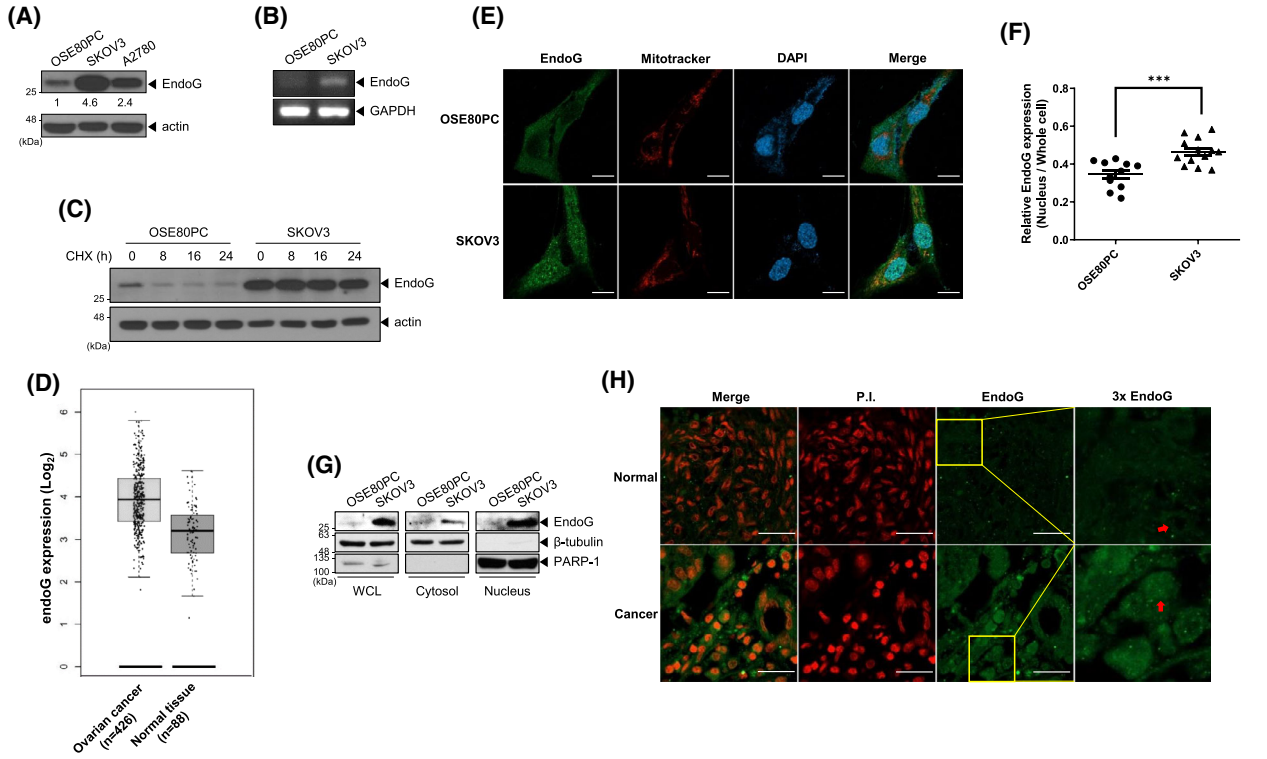

Fig. 2. Upregulated EndoG is localized in the nucleus and cytosol in OC cells. (A) The steady-state levels of EndoG were analyzed by WB with an anti-EndoG antibody in OSE80PC cells and the SKOV3 and A2780 OC cell lines. The numbers indicate the expression of EndoG relative to that of Actin. (B) mRNA expression of *endoG* via RT-PCR in normal ovary cells (OSE80PC) or OC cells (SKOV3). GAPDH was used as an internal control for RT-PCR. (C) OSE80PC and SKOV3 cells were treated with 200 μg·mL^{-1} CHX and harvested at the indicated times. WCLs were analyzed by WB. (D) The *endoG* mRNA expression was analyzed using the GEPIA database (http://gepia2.cancer-pku.cn). The box plots of 426 OC samples (left) and 88 normal samples (right) revealed upregulation of *endoG* mRNA expression in OC patient tissues compared to normal tissues. The height of each thick bar represents the median expression level. The whiskers represent the maximum and minimum values within each sample set. (E, F) Representative confocal images showing EndoG staining with an anti-EndoG antibody (green), Mitotracker (red), and DAPI (blue) in OSE80PC and SKOV3 cells, scale bar: 20 μm, (E) and the statistical analysis of relative EndoG expression (nuclear localization of EndoG relative to that in the whole cell) (F). The images were quantified using IMAGEJ. The means ± SEM are given for three independent experiments, ***$P < 0.001$, unpaired *t*-test (F). (G) Subcellular fractionation was performed for OSE80PC and SKOV3 cells. The EndoG level was measured along with marker proteins in the WCL and cytosolic and nuclear fractions; β-tubulin, a cytosolic marker, and PARP-1, a nuclear marker. (H) Representative immunohistochemical staining images showing high EndoG expression in carcinoma tissues (bottom) compared to non-carcinoma tissues (top). Anti-EndoG antibody (green). propidium iodide (PI) scale bar: 25 μm. OC tissue microarrays were obtained from US Biomax Inc (Materials and methods).

depletion in SKOV3 cells resulted in decreased cell viability upon oxidative stress compared to that in control cells (Fig. 1).

High ROS and cellular inhibitor of apoptosis protein (cIAP1) levels induce upregulation and nuclear localization of EndoG in OC cells

Previously, we reported that EndoG expression is increased under oxidative stress [17]. Therefore, we examined whether ROS levels were elevated in SKOV3 cells, which might cause EndoG upregulation. We assessed ROS levels in normal ovary cells, SKOV3 cells, and other types of cancer cells via DCFH-DA measurement. ROS levels were much higher in SKOV3 cells than in normal ovary cells and other cancer cells (Fig. 3A), which is consistent with several reports demonstrating high ROS levels in OC [7,8]. Comparison of the EndoG expression in these cell lines showed correlations between EndoG and ROS levels in each cell line (Fig. 3A,B). We hypothesized that if high ROS levels caused EndoG upregulation, decreasing ROS levels in SKOV3 cells might downregulate EndoG expression. Indeed, we found that treatment with antioxidants, including N-acetyl cysteine (NAC) or the glucose analog 2-deoxy-D-glucose (2-DG), decreased ROS levels in SKOV3 cells (Fig. 3C,D). In parallel, EndoG levels were reduced (Fig. 3E) by these

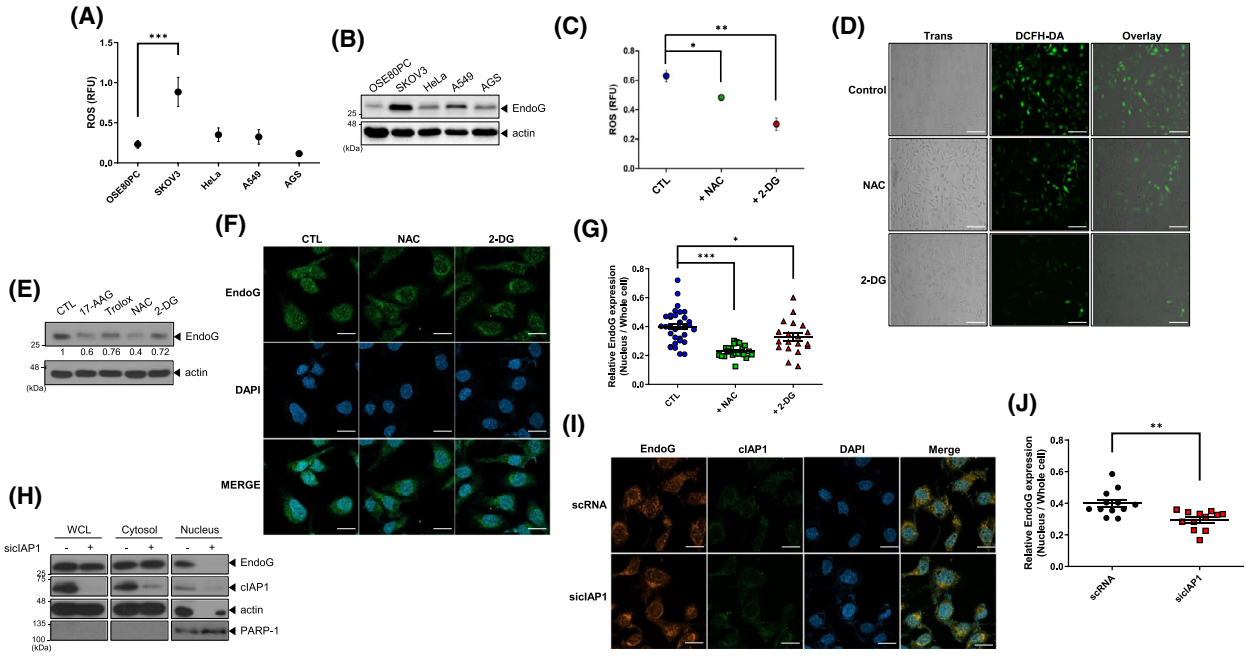

Fig. 3. High ROS and cIAP1 levels upregulate and increase nuclear localization of EndoG in OC cells. (A, B) The OSE80PC, SKOV3, HeLa (cervical cancer), A549 (lung cancer), and AGS (gastric cancer) cell lines were incubated with 5 μM DCFH-DA for 5 min. Fluorescence was measured using a microplate reader (Materials and methods) (A). WB analysis in a parallel experiment showed EndoG upregulation only in SKOV3 cells (B). (C, D) SKOV3 cells were treated with 10 mM NAC or 10 mM 2-DG. After 24 h, intracellular ROS levels were measured with a microplate reader (C) and a fluorescence microscope, scale bar: 100 μm (D). (E) EndoG levels in SKOV3 cells were decreased after treatment with various antioxidants. The numbers indicate EndoG expression relative to that of Actin. (F, G) SKOV3 cells were treated with 5 mM NAC or 5 mM 2-DG for 24 h and then immunostained with an anti-EndoG antibody (green) and DAPI (blue). EndoG expression (F) was quantified using IMAGEJ, scale bar: 20 μm. Total EndoG expression was downregulated and the nuclear EndoG ratio was further reduced (G). (H–J) SKOV3 cells were transfected with scRNA or siclAP1 for 48 h. The cytosolic or nuclear fraction was isolated, and each cell lysate was analyzed by WB with anti-EndoG, anti-cIAP1, antiactin, and anti-PARP-1 antibodies (H). The cells were immunostained with anti-EndoG (red) and anti-cIAP1 (green) antibodies and DAPI (blue), scale bar: 20 μm (I). The ratio of nuclear localization of EndoG to that in the whole cell was decreased according to analysis with IMAGEJ software (J). Values represent means ± SEM from triplicate independent experiments (***$P < 0.001$, **$P < 0.01$, *$P < 0.05$, unpaired *t*-test).

antioxidants. Moreover, we found that the relative amount of nuclear EndoG in SKOV3 cells was reduced upon NAC or 2-DG treatment (Fig. 3F,G, Fig. S2), indicating that EndoG localization and protein levels are also affected by intracellular ROS levels.

We previously reported that cIAP1, an E3 ligase, binds and ubiquitinates EndoG without affecting intracellular levels of EndoG and EndoG-mediated cell death [22,23]. Thus, we hypothesized that cIAP1 might be involved in the nuclear localization of EndoG through its Ring activity. Western blot (WB) results after subcellular fractionation showed that most EndoG in cIAP1-depleted SKOV3 cells was located in the cytosol and not in the nucleus (Fig. 3H). Immunocytochemical images after treatment with an anti-EndoG antibody and the statistical analysis revealed that the relative amount of nuclear EndoG in cIAP1-depleted SKOV3 cells was decreased to approximately 70% of that in control cells (Fig. 3I,J). Additionally, ectopic cIAP1 expression induced by Ub R63K caused EndoG to be mainly localized in the nucleus (Fig. S3). These data indicate that cIAP1 plays a role in the nuclear localization of EndoG. Taken together, our results demonstrate that elevated ROS and cIAP1 levels are required for upregulated expression and nuclear localization of EndoG in SKOV3 cells and suggest that post-translational modification of EndoG, such as oxidation and/or ubiquitination, might be necessary for nuclear localization.

The oxidation mutant EndoG P199E behaves differently from wild-type (WT) EndoG

In addition to its enhanced expression, we examined whether EndoG stability was also altered in SKOV3 cells due to its high ROS levels. When ROS levels in SKOV3 cells were decreased by NAC or 2-DG treatment, the half-life of EndoG was markedly reduced

(Fig. 4A). Previously, we reported that a co-chaperone E3 ligase, C-terminus of Hsc70-interacting protein (CHIP), binds and ubiquitinates EndoG, targeting it for proteasomal degradation. However, under oxidative stress, CHIP and EndoG could not interact, and no EndoG ubiquitination was observed [17], implying that CHIP-induced EndoG regulation is affected by intracellular ROS levels. Indeed, CHIP overexpression in SKOV3 cells, which have high ROS levels, did not affect the half-life of EndoG (Fig. 4B), while CHIP overexpression resulted in a sharp decrease in the EndoG half-life in normal ovary cells and HeLa cells (Fig. 4B). These results suggested that the conformation of EndoG might be altered by the increased ROS levels in OC. CPS-6, an EndoG homolog in *Caenorhabditis elegans*, normally acts as a dimer; when acting as a monomer under oxidative stress, CPS6 has no nuclease activity [24]. Oxidative insult specifically oxidized P207 of CPS-6, altering its conformation to a monomer. The primary sequence of EndoG is highly conserved from yeast to humans [11,24]. We mutated the 199th proline of human EndoG, equivalent to Pro207 of the *C. elegans* EndoG homolog, CPS-6, to glutamic acid (EndoG P199E, Fig. 4C) and determined whether it acts as a monomer. His-EndoG P199E protein did not interact with WT green fluorescent protein (GFP)-EndoG (Fig. 4D). In co-immunoprecipitation (co-IP) experiments, WT EndoG protein formed dimers with EndoG with various tags, but the EndoG P199E mutant protein did not form dimers (Fig. 4E). Additionally, EndoG P199E was localized in the nucleus and cytosol, while WT EndoG was expressed exclusively in the cytosol of HeLa cells, which have low intracellular ROS levels (Fig. 4F). Furthermore, cIAP1 showed greater interaction with EndoG P199E than with WT EndoG (Fig. 4G), and EndoG P199E exhibited greater ubiquitination by cIAP1 than that of WT EndoG (Fig. 4H, Fig. S4). These results indicate

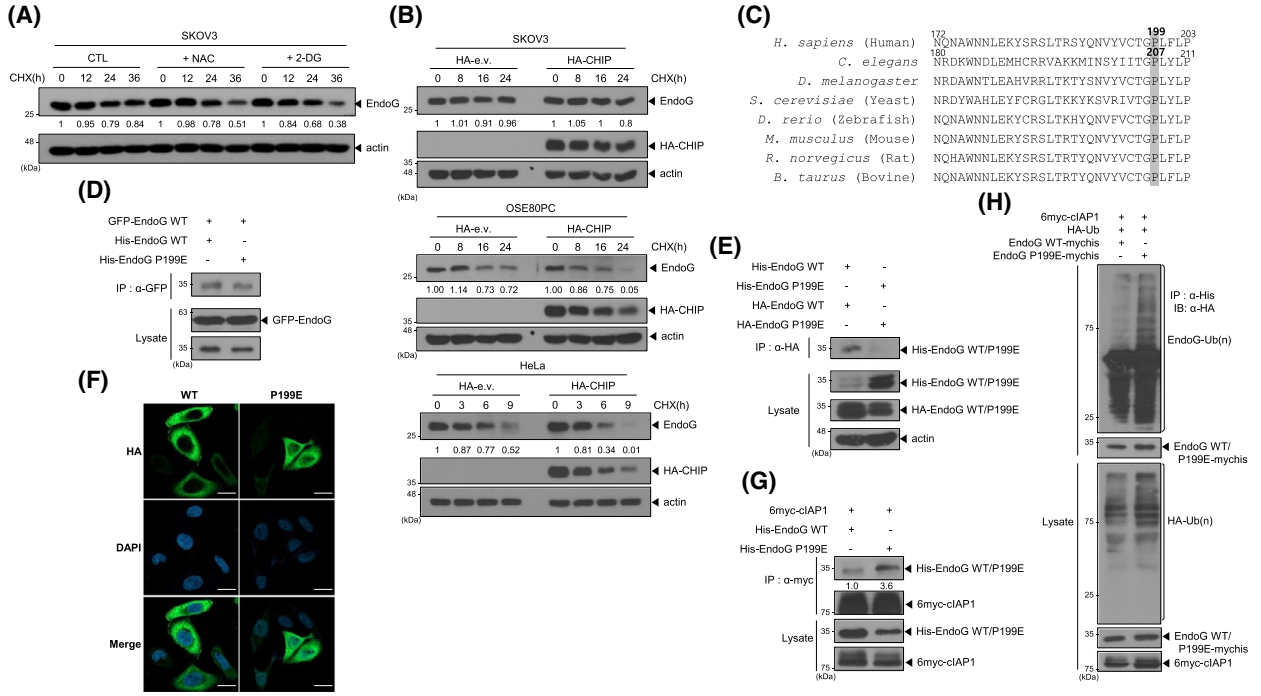

Fig. 4. The oxidation mutant EndoG P199E behaves differently from WT EndoG. (A) Antioxidants decreased the EndoG half-life in SKOV3 cells. The cells were co-treated with 200 μg·mL^{-1} CHX and 10 mM NAC or 10 mM 2-DG, and EndoG levels were compared by WB with an anti-EndoG antibody. The numbers indicate the ratio of EndoG to Actin. (B) The EndoG half-life was much longer in SKOV3 cells overexpressing HA-CHIP than in OSE80PC or HeLa cells overexpressing HA-CHIP. (C) The alignment of the EndoG sequences in various species shows their homology. (D) HEK293 cells were co-transfected with WT GFP-EndoG and WT His-EndoG or His-EndoG P199E. At 24 h after transfection, WCLs were prepared for co-IP with an anti-GFP antibody and then analyzed by WB using an anti-His antibody. (E) EndoG P199E did not form a dimer in the co-IP experiment. (F) HeLa cells were transfected with WT HA-EndoG or HA-EndoG P199E. The cells were immunostained with an anti-HA antibody (green) and DAPI (blue), scale bar: 20 μm. (G) Interaction between EndoG P199E and cIAP1 was greater than that between cIAP1 and WT EndoG. (H) HeLa cells were co-transfected with 6myc-cIAP1, HA-Ub, and His-EndoG (WT or P199E). No MG132 was added to the cell culture. A ubiquitination assay was performed by co-IP with an anti-His antibody, and WB assays were performed with anti-HA, anti-His, and anti-myc antibodies.

that human EndoG P199E behaves as a monomer and is primarily localized in the nucleus, suggesting that the high ROS levels in OC might induce an oxidized, monomeric EndoG with no nuclease activity that is readily ubiquitinated due to strong interaction with cIAP1 and is eventually localized in the nucleus under normal conditions.

EndoG depletion reduces cell viability

Because EndoG digests chromosomal DNA in the nucleus during apoptosis, it is surprising that OC cells survive and have a considerable amount of nuclear EndoG (Figs 2–4). Thus, we determined whether EndoG plays a role in cell viability in OC cells. A WST assay showed that cells depleted of EndoG via siRNA showed approximately 80% viability compared to controls (Fig. 5A,B), and cells depleted of EndoG via shRNA showed 60–80% viability compared with controls (Figs 5C and 1D). Moreover, EndoG-KD cells showed a marked decrease in colony numbers (Fig. 5D,E, Fig. S5). These results indicate that EndoG has a vital function in OC cells and is not involved in apoptosis. Furthermore, we overexpressed WT EndoG and EndoG P199E in EndoG-KD cell lines and performed WST assays to determine whether increased EndoG expression enhanced cell proliferation. Cells overexpressing EndoG P199E exhibited nearly 30% enhanced cell viability compared with control cells, while the viability of cells overexpressing WT EndoG was similar to that of control cells (Fig. 5F,G), suggesting that, under high ROS conditions, EndoG monomers might produce greater cell proliferation than EndoG dimers.

Depletion of EndoG caused cell cycle delay in the G2/M phase in OC cells

Next, we aimed to understand how EndoG participates in cell proliferation. To investigate whether EndoG is involved in cell cycle progression, we synchronized control cells (shCTL) and EndoG-KD cells (shendoG) at the G1 phase and released them after 72 h. The cell cycle profiles were monitored at the indicated time points via fluorescence-activated cell sorting analysis. EndoG-KD cells required almost twice the amount of time for cell doubling as that of control cells (Fig. 6A). Additionally, EndoG-KD cells had a smaller G1 and a greater G2/M population than control cells (Fig. 6B,C). We examined whether this

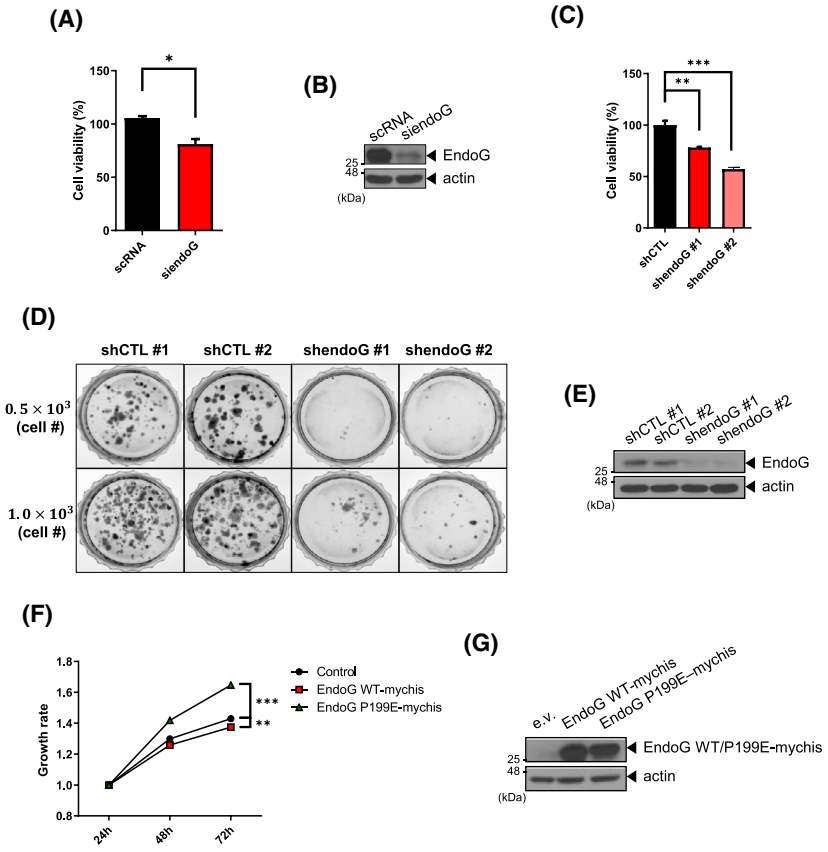

Fig. 5. EndoG depletion reduces cell viability. (A, B) SKOV3 cells were transfected with scRNA or siendoG. At 48 h after transfection, the cell viability was analyzed by WST assay (A). WCLs were analyzed by WB with anti-EndoG and antiactin antibodies (B). (C) EndoG-KD cells also showed reduced viability in the WST assay (C). (D, E) EndoG-KD cells were grown in the medium containing puromycin for 2 weeks. Colonies were stained with crystal violet, photographed (D), and subjected to a WB assay (E). (F, G) EndoG-KD cells were transfected with EndoG WT-mychis, HA-EndoG P199E-mychis, or a control empty vector. A WST assay was performed at the indicated time points after transfection (F). EndoG expression was revealed by WB (G). Values represent means ± SEM from triplicate independent experiments (***$P < 0.001$, **$P < 0.01$, *$P < 0.05$ unpaired *t*-test).

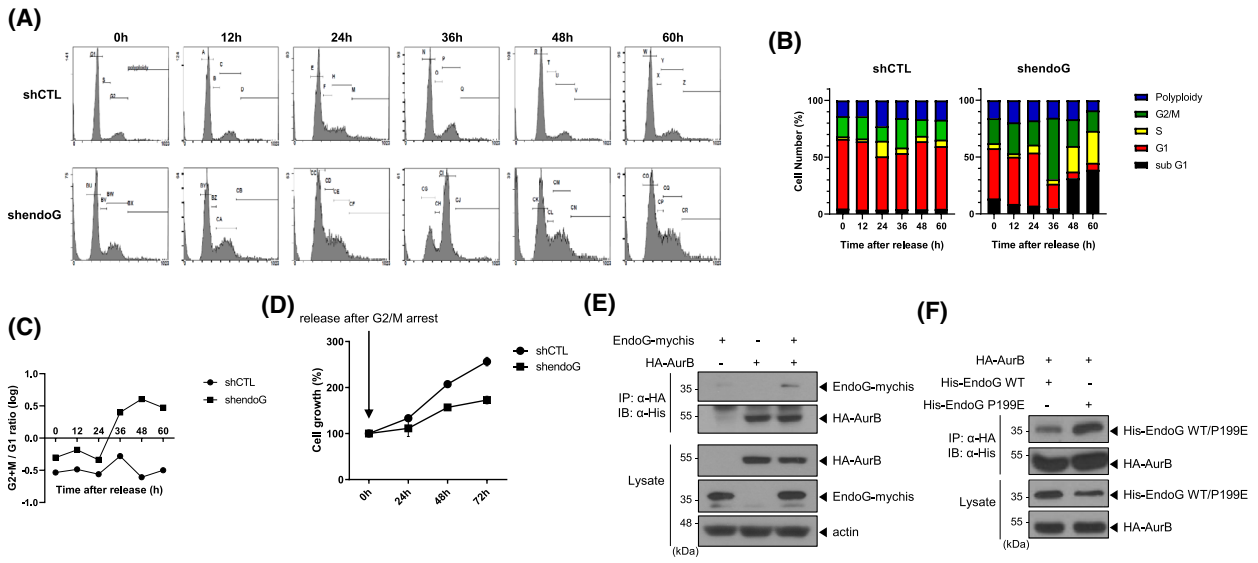

Fig. 6. Depletion of EndoG causes a cell cycle delay in the G2/M phase in OC cells. (A–C) EndoG-KD cells (shendoG #2) and control cells (shCTL) were arrested at the G1 phase by serum starvation for 72 h, and then the cells were released. The cell cycle was analyzed by flow cytometry (Materials and Methods). (D) Control cells (shCTL) or EndoG-KD cells were arrested at the G2/M phase by treatment with 200 ng·mL^{-1} nocodazole for 16 h, and then the cells were released. The cell viability was measured by WST assay at the indicated time points over 72 h. (E) EndoG interacted with AurB. HEK293 cells were co-transfected with EndoG-mychis and HA-AurB. After 24 h, co-IP was performed with an anti-HA antibody, and binding of EndoG to AurB was revealed by WB with an anti-His antibody. (F) Comparison of WT EndoG and EndoG P199E binding to AurB. HA-AurB showed stronger binding to His-EndoG P199E than to WT EndoG.

extended G2/M phase had a substantial effect on the progression of mitosis. Indeed, we found that EndoG-KD cells had a greater polyploid population (Fig. S5A), and approximately fourfold more EndoG-KD cells than control cells at the subG1 phase (Fig. S5B). In addition, we synchronized shCTL and EndoG-KD cells at the G2/M phase using nocodazole and counted cell numbers for 72 h. The control cells doubled within nearly 48 h. However, EndoG-KD cells showed only an approximately 50% growth increase at 72 h (Fig. 6D). We also observed similar results after G1 arrest (Fig. S5C). These results suggest that lack of EndoG expression delays cell cycle progression, characterized by an extended G2/M phase.

Aurora B (AurB) is a catalytic component of the chromosome passenger complex (CPC) and plays a key role in chromosome segregation and cytokinesis during mitosis [25]. According to proteomic analysis, AurB interacts with EndoG [26]. Therefore, we hypothesized that EndoG might participate in cell cycle regulation by interacting with AurB. Indeed, EndoG interacted with AurB (Fig. 6E, Fig. S5D), and interestingly, EndoG P199E exhibited enhanced interaction with AurB (Fig. 6F), implying that under high ROS conditions, EndoG monomers might preferentially bind to AurB, thereby regulating the mitotic process. Our results support this idea because EndoG P199E enhanced the cell proliferation rate (Fig. 5F), and EndoG-KD cells showed an abnormal cell cycle with an extended G2/M phase and polyploidy, similar to the phenotype observed in AurB-depleted cells (Fig. 6A–C, Fig. S5A).

Decreasing the ROS level reduces OC cell proliferation and enhances cisplatin efficacy by reducing EndoG availability

Our findings showed that increased ROS levels upregulated EndoG and altered its conformation, enhancing OC cell proliferation. Thus, we examined whether decreasing intracellular ROS levels would decrease cell viability due to a change in EndoG. If so, modulation of ROS levels in OC might be a promising strategy to suppress OC cell growth. Furthermore, NAC or 2-DG treatment reduced intracellular ROS levels (Fig. 7A) and endogenous EndoG levels (Fig. 7B), consistent with the results shown in Fig. 3. In parallel, cell viability was decreased by NAC or 2-DG treatment (Fig. 7C). If our hypothesis was true, EndoG-KD cells would not exhibit reduced growth under low ROS levels. NAC or 2-DG treatment inhibited growth in control cells (shCTL). However,

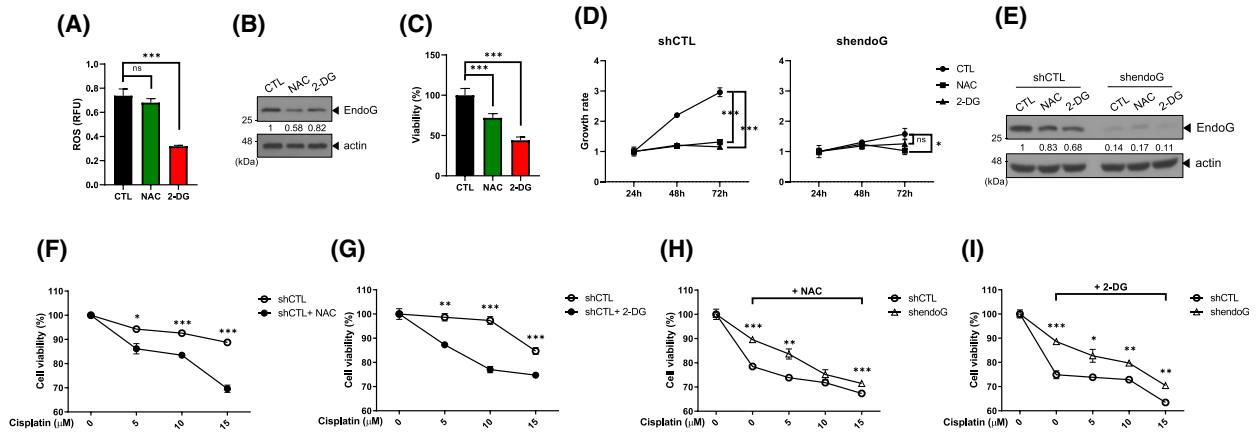

Fig. 7. Decreased ROS levels reduce OC cell proliferation and enhance the effect of cisplatin depending on EndoG availability. (A–C) SKOV3 cells were treated with 5 mM NAC or 5 mM 2-DG for 24 h. Then, the cells were incubated with 5 μM DCFH-DA for 5 min. ROS levels were measured using a microplate reader (A). Changes in EndoG levels were confirmed by WB with an anti-EndoG antibody (B). A WST assay indicated that the cell viability was decreased by NAC or 2-DG treatment (C). (D, E) Control cells (shCTL) and EndoG-KD cells (shendoG) were treated with 5 mM NAC or 5 mM 2-DG, and the cell number was counted at 24–72 h (D). WB analysis showed that NAC and 2-DG were only effective in controlling cells by reducing EndoG levels (E). (F, G) Control (shCTL) cells were treated with increasing concentrations of cisplatin in the absence or presence of NAC (F) or 2-DG (G), and cell viability was measured by WST assay. (H, I) The response to co-treatment with cisplatin and NAC (H) or 2-DG (I) was compared between the control cells (shCTL) and EndoG-KD cells (shendoG) using a WST assay. Values represent means ± SEM from triplicate independent experiments (***$P < 0.001$, **$P < 0.01$, *$P < 0.05$, unpaired *t*-test).

untreated EndoG-KD cells exhibited little cell growth, and antioxidant treatment did not further suppress growth (Fig. 7D). The EndoG level reduction was confirmed by WB analysis in a parallel experiment (Fig. 7E). These results suggest that OC cell growth depends on the availability of EndoG, which is quantitatively and qualitatively modulated by the intracellular ROS concentration.

We hypothesized that decreasing the ROS level could improve cisplatin efficacy, especially in EndoG-upregulated cancers such as OC. Indeed, the cell viability of control cells (shCTL) was markedly decreased by combined treatment with NAC and increasing concentrations of cisplatin compared to treatment with cisplatin alone (Fig. 7F). Combined treatment with 2-DG and cisplatin also showed a similar result (Fig. 7G). However, a clear discrepancy in EndoG-mediated cell viability suppression was observed between EndoG-KD cells (shendoG) and control cells (shCTL) treated with antioxidants and cisplatin (Fig. 7H,I). Control cells with endogenous EndoG were much more sensitive to NAC (Fig. 7H) and 2-DG (Fig. 7I), resulting in improved efficacy of low-dose cisplatin. However, EndoG-KD cells were less sensitive to antioxidants, as shown in Fig. 7D, and no obvious combined effect was observed. Taken together, our results demonstrate that antioxidants can at least partially enhance cisplatin efficacy by targeting EndoG in anti-OC therapy.

Discussion

EndoG is not only a DNA-cleaving nuclease and a cell death effector but is also a multifunctional protein modulated by intracellular ROS dynamics

During the two decades since EndoG was shown to be a cell death effector in *C. elegans* and mice, most studies have focused on inducing EndoG activity to kill cancer cells [20,21,27] or blocking its activity to induce cytoprotection [28,29]. In this classical view, EndoG is primarily localized in mitochondria during translation and translocates to the nucleus upon apoptotic insult. However, a growing number of studies have shown nonapoptotic roles of EndoG in either mitochondria or the nucleus. EndoG is involved in the maintenance of mitochondria [30,31], conservative recombination [32], and DNA rearrangement upon replication stress in the nucleus [33]. These reports extend the classical view of EndoG, especially regarding its nonapoptotic function in the nucleus. EndoG was originally purified and characterized in mammalian nuclei [34]. Therefore, it is not clear why EndoG does not cleave chromosomal DNA but rather plays a different role in the nucleus. High ROS levels have been shown to affect the conformation of purified CPS-6 (a homolog of human EndoG) in *C. elegans*. Under oxidative stress, CPS-6 undergoes structural alteration by oxidation, and EndoG monomers with diminished nuclease

activity, rather than EndoG dimers, are present, inhibiting cell death [24]. Thousands of proteins can be reversibly oxidized under high ROS conditions, especially by H_2O_2 [35]. Therefore, we hypothesized that intracellular oxidative stress represented by high ROS levels might modulate the conformation of human EndoG. Most cancer cells have high ROS levels due to their high energy requirements [7]. Indeed, high intracellular ROS levels are maintained in OC cell lines and patient tissues [8] (Fig. 3), and nuclear EndoG plays a vital role in OC proliferation (Figs 2–7). We assumed that in OC cells, which have high ROS levels, EndoG behaves as a monomer and is primarily oxidized and ubiquitinated by cIAP1, showing no nuclease activity. We have previously shown that increased EndoG levels during oxidative stress induce caspase-independent cell death in HeLa cells and primary rat cortical neurons [17]. Thus, it is unclear why EndoG shows the opposite response under high ROS conditions. OC cells may adapt to high ROS conditions, and therefore post-translational modifications of EndoG, such as oxidation and ubiquitination, would primarily affect EndoG expression, nuclear localization, and, subsequently, cell proliferation. Upregulation of EndoG has been shown in gastric and colorectal cancer patient tissues via immunohistochemistry [36]. The proposed mechanism in this study is likely to at least partly contribute to tumorigenesis in gastric and colorectal cancer through the upregulation of EndoG.

It is not clear how EndoG is regulated in normal cells if cancer cells are an extreme example. Cells dynamically maintain intracellular ROS within a certain range. Therefore, EndoG might be modified through ROS dynamics, and thus structurally altered types of EndoG could co-exist, with some localized in the nucleus and others localized in the mitochondria or cytosol. These EndoG subtypes could play distinct, either nonapoptotic or apoptotic, roles according to changes in ROS dynamics.

Nuclear EndoG is involved in OC cell cycle regulation

The role of upregulated nuclear EndoG in OC is unclear. We show that EndoG plays a vital role in cell proliferation because EndoG depletion reduced cell growth and overexpression of EndoG P199E-stimulated cell growth in EndoG-KD cells (Figs 5 and 6). Similarly, reduced EndoG expression has been shown to decrease cell viability in human embryonic kidney 293T (HEK293T) cells [37]. Additionally, a homolog of EndoG in yeast, Nuc1, exerts dual functionality, playing either a lethal or vital role, depending on mitochondrial respiration [38]. EndoG-depleted cells had a delayed cell cycle, especially at the G2/M phase, and an increased polyploid population (Fig. 6, and Fig. S5A,B). These results imply that EndoG is involved in cell cycle progression, especially in the late step of mitosis, because polyploidy indicates failure of cytokinesis. Chromosome segregation and cytokinesis are late steps during the completion of mitosis. These events are mainly controlled by the CPC, which is composed of AurB, INCENP, Survivin, and Borealin [25]. AurB plays a key role in chromosome segregation by correcting kinetochore attachment errors [25]. AurB was originally identified in yeast when screening for increase-in-ploidy mutants [39], and dysregulation of its activity caused aneuploidy in mammals [40]. We observed that AurB interacts with EndoG and has greater interaction with the EndoG P199E mutant (Fig. 6), suggesting that EndoG is involved in the regulation of mitosis and supports the function of AurB. Moreover, cIAP1, a member of the Inhibitor of Apoptotic Proteins family, shares baculoviral IAP repeat (BIR) domains [22] and binds and ubiquitinates EndoG P199E and WT EndoG, and cIAP1 depletion decreases nuclear EndoG localization (Figs 3H–J and 4H,G). Considering that EndoG binds to the BIR domains of cIAP1 [23], EndoG might interact with Survivin, a component of the CPC and a member of the IAP family with a single BIR domain. Therefore, we postulate that nuclear EndoG might augment the formation of CPC through its binding to AurB and potentially to Survivin.

Targeting EndoG alone or in combination with platinum-type agents could be effective for OC therapy

We suggest that the key to cancer treatment is to discover altered genes and understand their mechanism of action in tumorigenesis. We found that in OC, EndoG is upregulated, and EndoG localized in the nucleus has a nonapoptotic function (Figs 1–4). In OC, elevated ROS upregulates transcription and protein maintenance of EndoG (Figs 3 and 4). Therefore, we propose that the EndoG molecule is a reasonable candidate for the development of specific anti-OC therapy. An inhibitor that directly bound to EndoG was demonstrated by chemical library screening [28]. Thiobarbiturate analogs inhibited the nuclease activity of EndoG in the dimer conformation, showing a cytoprotective effect against various apoptotic stimuli.

However, it is unlikely that this type of inhibitor would effectively inhibit the altered EndoG under

elevated ROS conditions. Another EndoG-targeting method to consider is antioxidant treatment. SOD1-overexpressing transgenic rats exhibited reduced oxidative stress, and significantly less EndoG translocated to the nucleus [41]. We demonstrated that decreasing intracellular ROS levels downregulated EndoG, especially in the nucleus of OC cells (Fig. 3). Various types of antioxidants have been used in pre-clinical and clinical research, including NADPH oxidase inhibitors, SOD mimetics, and NAC [reviewed in ref. 9]. Among them, NAC has been used in combination with standard chemotherapy. NAC treatment potentiated doxorubicin-induced ATM and p53 phosphorylation, thereby enhancing their inhibition of cell proliferation in OC [42]. We demonstrated that NAC treatment decreased intracellular ROS, downregulating EndoG and decreasing cell viability (Figs 3 and 7). Furthermore, NAC sensitized OC cells to cisplatin in an EndoG-dependent manner (Fig. 7). The glucose analog 2-DG competes with glucose, interfering with aerobic glycolysis in cancer, and thus is widely used because of its antitumor potential. Additionally, 2-DG has been shown to increase intracellular ROS, thereby facilitating the apoptosis of certain types of cancer cells [43]. However, interestingly, we observed that 2-DG treatment significantly decreased ROS levels in OC cells, which were sensitized to cisplatin due to the reduction of EndoG (Fig. 7).

In our study, we demonstrated that elevated ROS in OC cell lines induces EndoG expression and nuclear localization, playing a vital role in OC tumorigenesis. We propose that targeting EndoG, either by itself or in combination with platinum-type agents, might be a promising strategy to enhance cancer cell death in the treatment of OC patients. This strategy can also be considered for the treatment of cancers with high EndoG expression such as gastric or colorectal cancers.

Materials and methods

Cell culture, transfection, and RNA interference

The ovarian cancer cell lines used in this study were acquired from Korean Cell Line 13 Bank. SKOV3, A2780, and OVCAR3 cell lines were cultured in RPMI (Welgene, Seoul, Korea) supplemented with 5% or 10% fetal bovine serum (FBS) at 37 °C in a humidified 5% CO_2 atmosphere. The HeLa cervical cancer cell line and HEK293 cells were cultured in DMEM (Welgene) supplemented with 10% FBS at 37 °C in a humidified 5% CO_2 atmosphere. The stable OC cell lines derived from SKOV3 cells generated in this study were maintained in the presence of puromycin. Transfection was performed using PEI (Sigma-Aldrich Inc, St. Louis, MO, USA) or Lipofectamine 2000 (Invitrogen, Carlsbad, CA, USA) according to the manufacturer's instructions. *cIAP1* or *endoG* siRNA was transfected into SKOV3 cells using Lipofectamine 2000 (Invitrogen) according to the manufacturer's instructions. After 48 h, whole cell lysates (WCLs) were analyzed by WB. The siRNA sequences were as follows (sense strand, 5′ to 3′): *cIAP1*, UCGCAAUGAUGAUGUCAAA; *endoG*, GGAAAUCCUACGUAAAGUA.

Antibodies and co-IP

Anti-EndoG (Proteintech, Rosemont, IL, USA), antiactin (Bethyl, Montgomery, TX, USA), anti-HA (Covance, Emeryville, CA, USA), anti-PARP-1 (Santa Cruz Biotechnology, Inc. Dallas, TX, USA), anti-His, anti-GFP, anti-β-tubulin, anti-myc 9E10 (Millipore, Billerica, MA, USA), and anti-cIAP1 (R&D Systems, Minneapolis, MN, USA) were used for WB or co- IP assays.

Co-IP was performed as follows unless otherwise noted. Cells were lysed in lysis buffer (50 mM Tris pH 8.0, 150 mM NaCl, 1 mM EDTA, 10% glycerol, 1% Triton X-100, protease inhibitor cocktail). WCLs were mixed with the indicated antibody for 2 h at 4 °C. Protein-A sepharose beads (Sigma-Aldrich) were incubated with the immunocomplex for 2 h at 4 °C and then washed three times with IP wash buffer (20 mM Tris pH 8.0, 150 mM NaCl, 1 mM EDTA, 1% Triton X-100). Samples were subjected to sodium dodecyl-sulfate polyacrylamide gel electrophoresis and analyzed by WB.

Database analysis

The mRNA expression levels of *endoG* in 426 tumors and 88 normal ovarian tissue samples were analyzed using the GEPIA database (http://gepia2.cancer-pku.cn). The GEPIA database is an interactive web server used to estimate mRNA expression data based on 9736 tumors and 8587 normal samples in The Cancer Genome Atlas and Genotype-Tissue Expression dataset projects. All boxplot analyses are presented with $\log_2$ (TPM + 1) values for the log scale.

Immunofluorescence

Cells grown on 12-mm diameter coverslips were fixed in 4% formaldehyde in phosphate-buffered saline (PBS) for 20 min and permeabilized using 0.5% Triton X-100 in PBS for 2 min. Cells were blocked in 5% normal goat serum in PBS for 1 h and then incubated overnight with the indicated primary antibody. After washing with PBS, cells were incubated with anti-rabbit Alexa Fluor 546- or anti-mouse Alexa Fluor 488-conjugated secondary antibody

(Invitrogen). After washing with PBS, the cells were counterstained with diamidino-2-phenylindole (DAPI) for 15 min and mounted on glass slides (Vector Laboratories, Inc., Burlingame, CA, USA). MitoTracker Red CMXRos (200 nM; Invitrogen) was used to stain mitochondria. Images were visualized using an LSM 800 Meta confocal microscope (Carl Zeiss, Inc., Oberkochen, Germany) and further analyzed by IMAGEJ software for quantification.

Ovarian tissue microarrays were obtained from a commercial supplier (US Biomax, Rockville, MD, USA; TMA catalog number T113a). The array contained biospecimens from 12 OC patients and one sample of normal ovary tissue, with duplicate cores for each OC patient and normal tissue. Immunohistochemistry was performed with an anti-EndoG antibody according to the manufacturer's instructions.

EndoG-KD stable cell lines and colony formation assay

Production of lentiviral particles was conducted according to the manufacturer's instructions (Sigma-Aldrich); the packaging lentiviral vector pLKO.1 contained control shRNA (shCTL) and endoG-specific shRNA (shEndoG, #1: sigma TRCN0000039644 and #2: sigma TRCN0000039645, respectively). To establish stable cell lines, SKOV3 cells were seeded in 60-mm culture dishes. Upon reaching 70% confluence, lentiviral particles at a multiplicity of infection of 15 in culture medium were added to the cells in the presence of 8 $\mu g \cdot mL^{-1}$ hexadimethrine bromide (Sigma-Aldrich), which increases the efficiency of viral infection. At 24 h after infection, puromycin (2 $\mu g \cdot mL^{-1}$) was added for selection for 72 h. EndoG-KD cell lines were seeded in six-well plates after maintenance at 37 °C, 5% CO_2 for 2 weeks. The colonies formed by each cell were fixed with 4% formaldehyde for 30 min and stained with 0.2% crystal violet for 40 min. The assay was performed in triplicate. All the experimental protocols, usage of human cell lines, and chemicals have been approved by the Institutional Biosafety Committee (IBC) at Kyung Hee University.

Protein half-life measurement

OSE80PC, SKOV3, and HeLa cells were treated with 200 $\mu g \cdot mL^{-1}$ cycloheximide (CHX) and then harvested at the indicated time points. Cells were lysed with RIPA buffer (50 mM Tris pH 7.4, 150 mM NaCl, 0.1% sodium dodecylsulfate, 1% Triton X-100, 0.5% Na-deoxycholate, 1 mM EDTA), and each sample was subjected to WB analysis.

Quantitative reverse-transcription polymerase chain reaction (qRT-PCR) analysis

Total RNA was isolated using an easy-spin RNA extraction kit (iNtRON, Seongnam-Si, Korea) according to the manufacturer's instructions. cDNA synthesis was performed using an M-MLV cDNA synthesis kit (Enzynomics, Daejeon, Korea). qRT-PCR was performed using a 2x SensiFAST SYBR No-ROX Mix (BIOLINE, Memphis, TN, USA) according to the manufacturer's instructions. The primer sets were as follows: *endoG* (sense: 5′-CGACAC GTTCTACCTGAGCA-3′, antisense: 5′-AGGATTTCCCA TCAGCCTCT-3′), *Dnmt1* (sense: 5′-TACCTGGACGACC CTGACCTC-3′, antisense: 5′-CGTTGGCATCAAAGATG GACA-3′), and glyceraldehyde 3-phosphate dehydrogenase (*GAPDH*, sense: 5′-GAGTCAACGGATTTGGTCGT-3′, antisense: 5′-TTGATTTTGGAGGGATCTCG-3′).

Cell fractionation

The cells were lysed in Buffer A (10 mM HEPES, 10 mM KCl, 0.1 mM EDTA, 0.1 mM EGTA, 1 mM DTT, 0.5 mM PMSF, protease inhibitor cocktail) and incubated for 15 min on ice. Buffer B (10% NP-40) was added, and the cells were centrifuged at 20 160 *g* for 10 min at 4 °C. The supernatant (cytosolic fraction) was then transferred to a clean tube. The pellet was washed twice with ice-cold Buffer A and resuspended in Buffer C (20 mM HEPES pH 7.9, 0.4 M NaCl, 1 mM EGTA, 1 mM DTT, 1 mM PMSF, protease inhibitor cocktail). The pellet was vortexed on the highest setting for 30 min at 4 °C. The supernatant (nuclear fraction) was transferred to a clean tube, and each sample was subjected to WB analysis.

Cell viability assay

The cells were seeded in 96-well plates, and cell viability was assessed using the EZ-cytox kit (Dogen Bio, Seoul, Korea) according to the manufacturer's instructions. The absorbance was measured at 450 nm using Multi-Mode microplate readers (BioTek, Winooski, VT, USA). The assay was performed in triplicate.

ROS measurement

The cells were seeded in 96-well black plates. DCFH-DA (2′, 7′-dichlorofluorescein diacetate, 5 μM) was pre-incubated in DPBS (DCFH-DA working solution) at 37 °C for 30 min. The cells were washed twice with DPBS and then incubated in 100 μL DCFH-DA working solution at 37 °C for 5 min. Fluorescence was measured by a fluorescence microplate reader (Molecular Devices, San Jose, CA, USA). The assay was performed in triplicate.

Flow cytometry

The cell lines were trypsinized and then centrifuged at 108 *g*. The cells were washed twice with DPBS, fixed with 75% ethanol for 1 h at 4 °C, and then washed twice with DPBS.

Harvested cells were resuspended in propidium iodide (PI) staining solution (3.8 mM sodium citrate, 50 $\mu g \cdot mL^{-1}$ PI in PBS). Fluorescence was analyzed using an FC500 flow cytometer (Beckman Coulter Inc., Miami, FL, USA).

Acknowledgments

We are grateful to Dr Choi at Kyung Hee University for the kind gift of the primary normal ovary cell line. This research was supported by the Basic Science Research Program through the National Research Foundation of Korea (NRF) funded by the Ministry of Education (2016R1D1A1B03936237, 2019R1F1A1058084, 2021R1F1A1063423).

Conflict of interest

The authors declare no conflict of interest.

Author contributions

YNC and TWS designed and performed most of the experiments. YTL performed the experiments and the data analysis and helped to write the manuscript. DHJ assisted in some experiments and data analysis. SJY designed the experiments, supervised the project, and wrote the manuscript. All authors read and approved the manuscript.

Data accessibility

The data that support the findings of this study are available from the corresponding author [yoosoonji@khu.ac.kr] upon reasonable request.

References

1 Matulonis UA, Sood AK, Fallowfield L, Howitt BE, Sehouli J and Karlan BY (2016) Ovarian cancer. *Nat Rev Dis Primers* **2**, 16061.
2 Muggia F (2009) Platinum compounds 30 years after the introduction of cisplatin: implications for the treatment of ovarian cancer. *Gynecol Oncol* **112**, 275–281.
3 Banerjee S and Kaye SB (2013) New strategies in the treatment of ovarian cancer: current clinical perspectives and future potential. *Clin Cancer Res* **19**, 961–968.
4 Mao CL, Seow KM and Chen KH (2022) The utilization of bevacizumab in patients with advanced ovarian cancer: a systematic review of the mechanisms and effects. *Int J Mol Sci* **23**, 6911.
5 Foo T, George A and Banerjee S (2021) PARP inhibitors in ovarian cancer: an overview of the practice-changing trials. *Genes Chromosomes Cancer* **60**, 385–397.
6 Flynn MJ and Ledermann JA (2022) Ovarian cancer recurrence: is the definition of platinum resistance modified by PARPi and other intervening treatments? The evolving landscape in the management of platinum-resistant ovarian cancer. *Cancer Drug Resist* **5**, 424–435.
7 Cheung EC and Vousden KH (2022) The role of ROS in tumour development and progression. *Nat Rev Cancer* **22**, 280–297.
8 Cohen S, Mehrabi S, Yao X, Millingen S and Aikhionbare FO (2016) Reactive oxygen species and serous epithelial ovarian adenocarcinoma. *Cancer Res J (N Y N Y)* **4**, 106–114.
9 Luo M, Zhou L, Huang Z, Li B, Nice EC, Xu J *et al.* (2022) Antioxidant therapy in cancer: rationale and Progress. *Antioxidants (Basel)* **11**, 1128.
10 Stieg DC, Wang Y, Liu LZ and Jiang BH (2022) ROS and miRNA dysregulation in ovarian cancer development, angiogenesis and therapeutic resistance. *Int J Mol Sci* **23**, 6702.
11 Parrish J, Li L, Klotz K, Ledwich D, Wang X and Xue D (2001) Mitochondrial endonuclease G is important for apoptosis in *C. elegans*. *Nature* **412**, 90–94.
12 Li LY, Luo X and Wang X (2001) Endonuclease G is an apoptotic DNase when released from mitochondria. *Nature* **412**, 95–99.
13 Schäfer P, Scholz SR, Gimadutdinow O, Cymerman IA, Bujnicki JM, Ruiz-Carrillo A, Pingoud A and Meiss G (2004) Structural and functional characterization of mitochondrial EndoG, a sugar non-specific nuclease which plays an important role during apoptosis. *J Mol Biol* **338**, 217–228.
14 Kalinowska M, Garncarz W, Pietrowska M, Garrard WT and Widlak P (2005) Regulation of the human apoptotic DNase/RNase endonuclease G: involvement of Hsp70 and ATP. *Apoptosis* **10**, 821–830.
15 Ishihara Y and Shimamoto N (2006) Involvement of endonuclease G in nucleosomal DNA fragmentation under sustained endogenous oxidative stress. *J Biol Chem* **281**, 6726–6733.
16 Higgins GC, Beart PK and Nagley P (2009) Oxidative stress triggers neuronal caspase-independent death: endonuclease G involvement in programmed cell death-type III. *Cell Mol Life Sci* **66**, 2773–2787.
17 Lee JS, Seo TW, Yi JH, Shin KS and Yoo SJ (2013) CHIP has a protective role against oxidative stress-induced cell death through specific regulation of endonuclease G. *Cell Death Dis* **4**, e666.
18 Basnakian AG, Apostolov EO, Yin X, Abiri SO, Stewart AG, Singh AB and Shah SV (2006) Endonuclease G promotes cell death of non-invasive human breast cancer cells. *Exp Cell Res* **312**, 4139–4149.
19 Wang X, Tryndyak V, Apostolov EO, Yin X, Shah SV, Pogribny IP and Basnakian AG (2008) Sensitivity of human prostate cancer cells to chemotherapeutic drugs

depends on EndoG expression regulated by promoter methylation. *Cancer Lett* **270**, 132–143.
20 Winnard PT Jr, Botlagunta M, Kluth JB, Mukadam S, Krishnamachary B, Vesuna F and Raman V (2008) Hypoxia-induced human endonuclease G expression suppresses tumor growth in a xenograft model. *Cancer Gene Ther* **15**, 645–654.
21 Chiang JH, Tsai FJ, Hsu YM, Yin MC, Chiu HY and Yang JS (2020) Sensitivity of allyl isothiocyanate to induce apoptosis via ER stress and the mitochondrial pathway upon ROS production in colorectal adenocarcinoma cells. *Oncol Rep* **44**, 1415–1424.
22 Vaux DL and Silke J (2005) IAPs, RINGs and ubiquitylation. *Nat Rev Mol Cell Biol* **6**, 287–297.
23 Seo TW, Lee JS and Yoo SJ (2014) Cellular inhibitor of apoptosis protein 1 ubiquitinates endonuclease G but does not affect endonuclease G-mediated cell death. *Biochem Biophys Res Commun* **451**, 644–649.
24 Lin JLJ, Nakagawa A, Skeen-Gaar R, Yang WZ, Zhao P, Zhang Z *et al.* (2016) Oxidative stress impairs cell death by repressing the nuclease activity of mitochondrial endonuclease G. *Cell Rep* **16**, 279–287.
25 Carmena M, Wheelock M, Funabiki H and Earnshaw WC (2012) The chromosomal passenger complex (CPC): from easy rider to the godfather of mitosis. *Nat Rev Mol Cell Biol* **13**, 789–803.
26 Huttlin EL, Ting L, Bruckner RJ, Gebreab F, Gygi MP, Szpyt J *et al.* (2015) The BioPlex network: a systematic exploration of the human interactome. *Cell* **162**, 425–440.
27 Glinka EM (2015) Killing of cancer cells through the use of eukaryotic expression vectors harbouring genes encoding nucleases and ribonuclease inhibitor. *Tumour Biol* **36**, 3147–3157.
28 Jang DS, Penthala NR, Apostolov EO, Wang X, Crooks PA and Basnakian AG (2015) Novel cytoprotective inhibitors for apoptotic endonuclease G. *DNA Cell Biol* **34**, 92–100.
29 Büttner S, Habernig L, Broeskamp F, Ruli D, Vögtle FN, Vlachos M, Macchi F, Küttner V, Carmona-Gutierrez D, Eisenberg T *et al.* (2013) Endonuclease G mediates alpha-synuclein cytotoxicity during Parkinson's disease. *EMBO J* **32**, 3041–3054.
30 McDermott-Roe C, Ye J, Ahmed R, Sun XM, Serafín A, Ware J, Bottolo L, Muckett P, Cañas X, Zhang J *et al.* (2011) Endonuclease G is a novel determinant of cardiac hypertrophy and mitochondrial function. *Nature* **478**, 114–118.
31 Wiehe RS, Gole B, Chatre L, Walther P, Calzia E, Ricchetti M and Wiesmüller L (2018) Endonuclease G promotes mitochondrial genome cleavage and replication. *Oncotarget* **9**, 18309–18326.
32 Robertson AB, Robertson J, Fusser M and Klungland A (2014) Endonuclease G preferentially cleaves 5-hydroxymethylcytosine-modified DNA creating a substrate for recombination. *Nucleic Acids Res* **42**, 13280–13293.
33 Gole B, Baumann C, Mian E, Ireno CI and Wiesmüller L (2015) Endonuclease G initiates DNA rearrangements at the MLL breakpoint cluster upon replication stress. *Oncogene* **34**, 3391–3401.
34 Gerschenson M, Houmiel KL and Low RL (1995) Endonuclease G from mammalian nuclei is identical to the major endonuclease of mitochondria. *Nucleic Acids Res* **23**, 88–97.
35 Topf U, Suppanz I, Samluk L, Wrobel L, Böser A, Sakowska P *et al.* (2018) Quantitative proteomics identifies redox switches for global translation modulation by mitochondrially produced reactive oxygen species. *Nat Commun* **9**, 324.
36 Yoo NJ, Jeong EG, Kim MS, Ahn CH, Kim SS and Lee SH (2008) Increased expression of endonuclease G in gastric and colorectal carcinomas. *Tumori* **94**, 351–355.
37 Huang KH, Ku CC and Lehman IR (2006) Endonuclease G: a role for the enzyme in recombination and cellular proliferation. *Proc Natl Acad Sci USA* **103**, 8995–9000.
38 Büttner S, Eisenberg T, Carmona-Gutierrez D, Ruli D, Knauer H, Ruckenstuhl C, Sigrist C, Wissing S, Kollroser M, Fröhlich KU *et al.* (2007) Endonuclease G regulates budding yeast life and death. *Mol Cell* **25**, 233–246.
39 Chan CS and Botstein D (1993) Isolation and characterization of chromosome-gain and increase-in-ploidy mutants in yeast. *Genetics* **135**, 677–691.
40 Steigemann P, Wurzenberger C, Schmitz MH, Held M, Guizetti J, Maar S and Gerlich DW (2009) Aurora B-mediated abscission checkpoint protects against tetraploidization. *Cell* **136**, 473–484.
41 Yu F, Sugawara T, Nishi T, Liu J and Chan PH (2006) Overexpression of SOD1 in transgenic rats attenuates nuclear translocation of endonuclease G and apoptosis after spinal cord injury. *J Neurotrauma* **23**, 595–603.
42 Brum G, Carbone T, Still E, Correia V, Szulak K, Calianese D, Best C, Cammarata G, Higgins K, Ji F *et al.* (2013) *N*-acetylcysteine potentiates doxorubicin-induced ATM and p53 activation in ovarian cancer cells. *Int J Oncol* **42**, 211–218.
43 Shutt DC, O'Dorisio MS, Aykin-Burns N and Spitz DR (2010) 2-deoxy-D-glucose induces oxidative stress and cell killing in human neuroblastoma cells. *Cancer Biol Ther* **9**, 853–861.

Supporting information

Additional supporting information may be found online in the Supporting Information section at the end of the article.

Fig. S1. The levels of EndoG in various ovarian cancer cell lines. (A) The steady-state levels of EndoG were analyzed by WB with an anti-EndoG antibody in OSE80PC cells and the ovarian cancer cell lines JH514, OVCAR3, and SKOV3. The numbers indicate expression of EndoG relative to actin. (B) mRNA expression of *dnmt1* via RT-PCR in normal ovary cells (OSE80PC) or ovarian cancer cells (SKOV3). GAPDH was used as an internal control for RT-PCR.

Fig. S2. The relative nuclear EndoG level in SKOV3 cells treated with10 mM NAC or 10 mM 2-DG (A) or with cotreatment of 5 mM NAC and 5 mM 2-DG (B) for 24 hours. Immunostaining was performed with an anti-EndoG antibody and DAPI, and the images and statistical analysis were performed using Image J (means ± SEM are given for three independent experiments, ***$p<0.001$, **$p<0.01$, unpaired t-test).

Fig. S3. Overexpression of cIAP1 with Ub R63K led to EndoG being mainly localized in the nucleus. SKOV3 cells were transfected with 6myc-cIAP1 and HA-Ub R63K for 24 hours and immunostained with the indicated antibodies, scale bar: 20 μm.

Fig. S4. EndoG P199E exhibited greater ubiquitination by cIAP1. (A) Ubiquitination assay (Materials and Methods). (B) Statistical analysis after quantification of (A) using Image J (means ± SEM are given for three independent experiments, ***$p<0.001$, unpaired t-test).

Fig. S5. EndoG-KD cells (shendoG) showed more cells with tetraploidy. (A) and subG1-staged cells (B) than control cells (shCTL) on analysis of the cell cycle profile using flow cytometry after serum starvation for72 hours. (C) The cells were arrested at the G1 phase by serum starvation, and then the cells were released. The cell viability was measured by WST assay over 72 hours, means ± SEM are given for three independent experiments. (D) HEK293 cells were co-transfected with EndoG-mychis and HA-AurB. After 24 hours, co-IP assays were performed with an anti-myc antibody, and HA-AurB binding to EndoG-mychis was revealed using an anti-HA antibody on WB.

ZEISS CASE STUDY

High Content Imaging for Genotoxicity

By Dr. Philipp Seidel
11 NOVEMBER 2021

ABSTRACT

From Image to Results | High Content Imaging for Genotoxicity

In this series *"From Image to Results"*, we explore various case studies explaining how to reach results from your demanding samples and acquired images in an efficient way. For each case study, we highlight different samples, imaging systems, and research questions.

In this episode, we set up an application example to perform DNA damage analysis by employing ZEISS Axio Observer and the Arivis Vision4D image analysis software.

Key Learnings:

- How to perform the general analysis with single drug treatment
- How to automate imaging and analysis procedures, to the point that the whole process can be scaled easily to perform high-content screening (HCS) or be adapted to other complex experimental settings

ZEISS CASE STUDY

Organoid Analysis

By Dr. Philipp Seidel
11 NOVEMBER 2021

ABSTRACT

From Image to Results | Organoid Analysis

In this series *"From Image to Results"*, we explore various case studies explaining how to reach results from your demanding samples and acquired images in an efficient way. For each case study, we highlight different samples, imaging systems, and research questions.

In this episode, we showcase a simple imaging experiment performed on intestinal organoids treated with and without a Wnt-inhibiting drug, with the experimental goal to study the role of Wnt signaling in **organoid formation**.

Key Learnings:

- How to study the role of Wnt signaling in organoid formation
- How to use machine learning to segment outer organoid cell layers
- How to perform nucleus and cell body segmentation